Toward Plasmon Enhanced Organic Photovoltaics:

A Study of Nanoparticle Size and Shape

A thesis submitted to the College of Graduate Studies and Research

in partial fulfillment of the requirements for the

Degree of Master of Science

in the Department of Chemistry

University of Saskatchewan

Saskatoon

By

Cheryl A. Burnyeat

Permission to Use

In presenting this thesis/dissertation in partial fulfillment of the requirements for a Postgraduate degree from the University of Saskatchewan, I agree that the Libraries of this University may make it freely available for inspection. I further agree that permission for copying of this thesis/dissertation in any manner, in whole or in part, for scholarly purposes may be granted by the professor or professors who supervised my thesis/dissertation work or, in their absence, by the Head of the Department or the Dean of the College in which my thesis work was done. It is understood that any copying or publication or use of this thesis/dissertation or parts thereof for financial gain shall not be allowed without my written permission. It is also understood that due recognition shall be given to me and to the University of Saskatchewan in any scholarly use which may be made of any material in my thesis/dissertation.

Requests for permission to copy or to make other use of materials in this thesis/dissertation in whole or part should be addressed to:

Head of the Department of Chemistry
University of Saskatchewan
Saskatoon, Saskatchewan (S7N 5C9)
Canada

Abstract

This thesis reports the functionalization of metal nanoparticles to allow for solubility in organic solvents used in solar cell fabrication. Functionalization of the nanoparticles using poly(ethylene glycol) methyl ether thiol (PEG-SH) allows for the phase transfer of the nanoparticles from aqueous solution to organic solvents. Once functionalized it was found that nanoprisms will undergo a shape change. This change in morphology was investigated using UV-Vis measurements, transmission electron microscopy (TEM), and X-ray Absorption Near Edge Structure (XANES) measurements and a mechanism for the shape degradation is presented. The PEG functionalization procedure can be applied to other types of metal nanoparticles and once soluble, these particles were incorporated into the active layer of the BHJ cells. It has been found that the PEG functionalized particles do not improve the cell efficiency, but they do affect the cell performance. The addition of the particles does not influence the open circuit voltage, but it does affect the current density of the devices. This suggests that the particles may be acting as electron traps, not allowing current to flow efficiently through the device. This shows that while the PEG-ylation of the particles is effective at solubilising them into useful organic solvents, the thickness of the PEG layer on the nanoparticles may not provide protection from electrons and allow for effective charge transfer throughout the solar cell.

Co-Authorship Statement

The work done in Chapter 2 is the result of collaboration with group members Lijia Liu, Reegan Lepsenyi, and Izuoma Nwabuko.

A version of chapter 2 has been accepted for publication in Chemistry of Materials. The principal author of the submitted article is Lijia Liu. I have written the version of text that is included in this thesis.

I provided assistance and supervision on nanoprism sample preparation, PEG-ylation procedure, and UV-Vis measurements for undergraduate students Reegan Lepsenyi and Izuoma Nwabuko. The UV-Vis kinetics data for the PEG-ylation of silver nanoprisms stability experiments was collected by Reegan Lepsenyi and Izuoma Nwabuko. The 1000 MW PEG concentration experiments were performed by Izuoma Nwabuko. Reegan Lepsenyi performed the 2 000, 5000, and 10000 MW PEG concentration variation experiments. I performed TEM image collection and XANES sample preparation. The XANES experimental design was done by Lijia Liu, and data collection was performed collectively by Lijia Liu, Reegan Lepsenyi and me. I interpreted the XANES data included in this thesis.

A small portion of the work in chapter 3 was performed by undergraduate student Xioameng Wang. I supervised and assisted with his project on determining the usability and layer thickness optimization of MoO_3 as a hole transport layer in BHJ cells.

Acknowledgements

There are a number of people that I need to thank for their help throughout my master`s program. First to thank is my family; Bob, Kathy, and Andrew Burnyeat. You have all been supportive, whether you were here in the city, or half way around the globe. I thank you for your patience, encouragement, and your ability to keep me grounded. I absolutely would not have succeeded in any of my studies if it wasn`t for your love and support.

I would like to thank Dr. Tim Kelly for taking me on as his first graduate student. He was patient, encouraging, and knowledgeable, even when neither of us knew what was going on. Thank you for all the guidance and support you gave me.

To all the members of the Kelly group, both past and present, as well as other member of the Department of Chemistry, thank you for being there as an amazing source for collaboration during the serious work and entertainment during the not so serious times.

I would also like to thank Yongfeng Hu and everyone at the SXRMB beamline for all of the help at the Canadian Light Source, as well as Guosheng Lui in the Department of Biology for his assistance with the transmission electron microscope.

Finally I would like to thank my Adam, for loving me unconditionally, even when I was crazy, and keeping me firmly planted in reality. I am so incredible grateful for your encouragement when I was stressed or unsure, and I love you so much for that.

Table of Contents

List of Figures

List of Tables

List of Abbreviations

APTES	3-aminopropyltriethoxysilane
BHJ	Bulk heterojunction
CIGS	Copper indium gallium selenide
DSSC	Dye sensitized solar cell
EQE	External quantum efficiency
fcc	Face centered cubic
FF	Fill factor
HOMO	Highest occupied molecular orbital
hcp	Hexagonal close packed
I_m	Current at maximum power point
IPCE	Incident photon to current efficiency
I_{SC}	Short circuit current
ITO	Indium tin oxide
IQE	Internal quantum efficiency
IZO	Indium doped zinc oxide
J_{SC}	Short circuit current density
LUMO	Lowest unoccupied molecular orbital
LSPR	Localized surface plasmon resonance
MHA	Mercaptohexadecanoic acid
oDCB	Ortho-dichlorobenzene
OPV	Organic photovoltaic
P3HT	Poly-3-hexylthiophene

PBDTTT-C-T	poly[4,8-bis-substituted-benzo [1,2-b:4,5-b0]dithiophene-2,6-diyl-alt-4-substituted-thieno[3, 4-b]thiophene-2,6-diyl]
PCDTBT	Poly[*N*-9′-heptadecanyl-2,7-carbazole-*alt*-5,5-(4′,7′-di-2-thienyl-2′,1′,3′-benzothiadiazole)], Poly[[9-(1-octylnonyl)-9H-carbazole-2,7-diyl]-2,5-thiophenediyl-2,1,3-benzothiadiazole-4,7-diyl-2,5-thiophenediyl]
PCBM	Phenyl-$C_{60/70}$-butyric acid methyl ester
PEDOT:PSS	Poly (3,4-ethylenedioxythiophene):poly (4-styrenesulfonate)
PEG	Poly(ethylene glycol)
PEG-SH	Thiol-terminated poly(ethylene glycol)
PTB7	Poly [[4,8-bis[[2-thylhexyl] oxy] benzo[1,2-b 4,5b'] dithiophene-2,6-diyl][3-fluor-2[[2-ehtylhexyl]carbonyl] thieno[3,4,6] thiophene diyl]]
TEM	Transmission electron microscopy
V_m	Voltage at maximum power point
V_{OC}	Open circuit voltage
XANES	X-ray Absorption Near Edge Structure

Chapter 1 - Introduction

Organic Photovoltaic Solar Cells

Introduction

With the world's energy consumption slowly increasing, and the amounts of available fossil fuels slowly decreasing, society is looking for new types of renewable energy sources. In 2011, the energy consumption in the United States was 97.5 quadrillion Btu. Only 9.0 quadrillion Btu (9.3%) of that came from renewable energy sources, including biomass, geothermal, wind, hydro, and solar.[1] These alternative energy sources are attractive because they are renewable; they use naturally occurring energy sources that will automatically replenish after they are used to create useable energy.

Solar power may be the most underutilized of the types of renewable resources in the world. The United States reported that in 2011 only 0.2% of the power that the country consumed was solar power.[1] Each year approximately 5.46×10^6 EJ of energy from the sun reaches the earth. Over the years 2005-2010, the annual world energy consumption was approximately 500 EJ. This is approximately 0.01% of the light energy available[2]. Solar energy has the potential to become a major source of renewable energy across the globe. Currently the cost of solar power is high and the amount of energy that can be delivered is low in comparison, but this is something researchers are looking to improve.

There are many different types of solar cells, all with the same general function. Solar energy is captured by the device and converted into electrical energy. Exactly how this is done depends on the type of cell. The three major categories of cells that are being developed are

crystalline silicon, thin film, and emerging photovoltaics. Each type of cell has its own challenges and efficiency records are shown in figure 1-1.

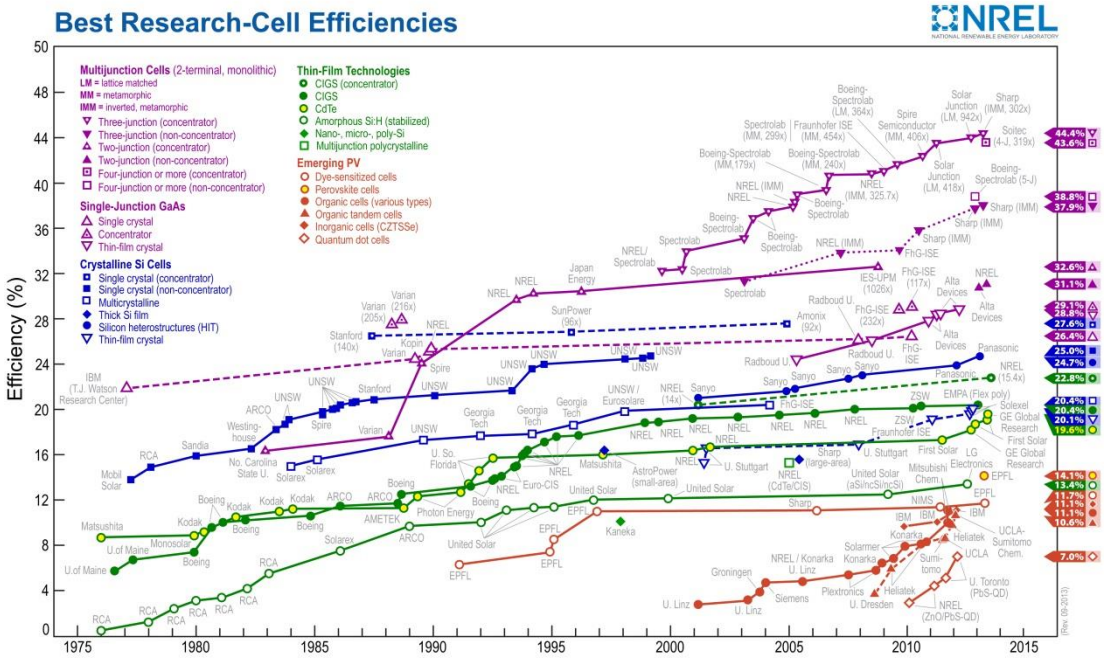

Figure 1-1 - Record solar cell efficiencies for different cell types[3]

This chart shows how the different technologies have improved and evolved over the last 4 decades. The current records for cell efficiencies within each type are shown on the right hand side of the chart. The current overall highest record for efficiency is for a multijunction type cell, with an efficiency value of 44.0%. A multijunction solar cell has a number of layers within the cell that are each tuned to absorb different wavelengths of light. The current generation of multijunction cells have three layers; the current record holding cell consists of GaInP, GaAs, and Ge layers.[4] This cell also uses a concentrating system to focus the incoming solar energy and concentrate it onto the cell, increasing the amount of light that reaches the cell. These

multijunction cells are extremely complex which causes them to be difficult and expensive to fabricate.

Another type of commercially available cell is a crystalline silicon cell. This type of cell is made up of either a single continuous crystal of silicon, or of smaller silicon crystals. The monocrystalline variety is more efficient than polycrystalline cells, but it is significantly more expensive due to processing conditions required. These cells are often brittle which makes their installation difficult, even though they are very commonly used commercially.

Thin film technologies are on the cutting edge of production research. The goal in this type of cell is to create a cell that is as thin as possible. This will allow the cells to be mounted on more flexible substrates, producing creative ways of incorporating these cells into daily life. There are three main types of these thin film cells: amorphous silicon (a-Si), cadmium telluride (CdTe), and copper indium gallium selenide (CIGS).[5] Rather than crystalline like the commercially available silicon cell, the a-Si cells are made of amorphous silicon. These cells are less efficient due to their thickness, have poor carrier mobilities, and are subject to degradation. The CIGS type cell is similar in structure to a silicon cell, but the manufacturing techniques are less costly. The latest technology prepares these cells in a way that is similar to printing newspapers, and is called roll-to-roll processing. The substrate is an aluminum foil electrode that the CIGS ink is printed onto, then wrapped with a foil lamination, and finally the transparent top electrode is printed on to the top of the cell.[6] The CdTe cells are also similar in structure, but unfortunately the cadmium within the cell is toxic, due to its ability to accumulate within the food chain, similar to mercury.

An emerging type of solar cell is a dye sensitized solar cell (DSSC). This is a thin cell that is made up of a sensitizer or dye that is attached to a wide band semiconductor.[7] Often a

liquid electrolyte is required to carry the electrons throughout the cell, but this can cause limitations in cell use. In the newest generation of DSSCs the electrolyte is not necessary, allowing for the cells to be used in all types of environments.[8] These types of cells currently have some of the best efficiencies of all the new and emerging types of cell technologies. Since 1991 these cells have improved in efficiency from ~5% to the current record of 15% held by the Grätzel group.[9] The rise of DSSC efficiencies began with the "Grätzel Cell" in 1991. This type of DSCC cell is based on the dye being adsorbed on to the surface of TiO_2 nanoparticles.[7] The basic structure of the DSSC is shown in figure 1-2.

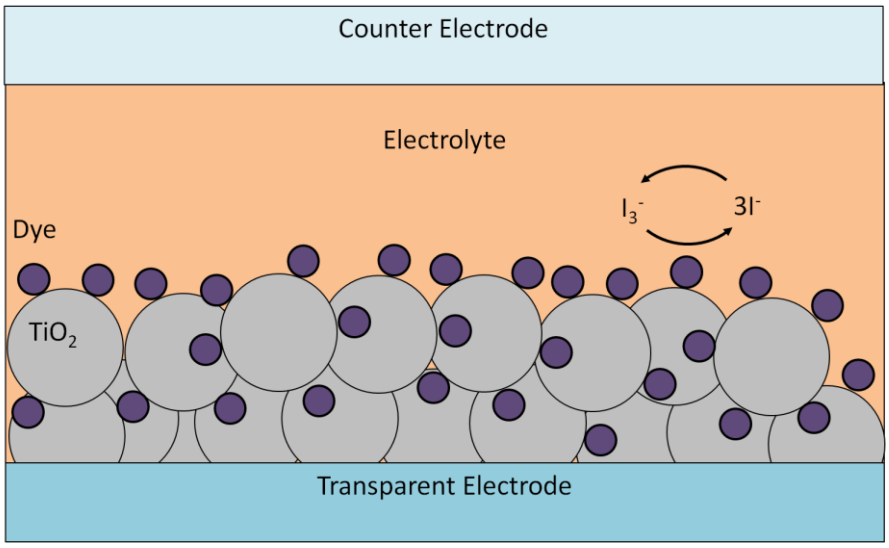

Figure 1-2 - DSSC structure

The sensitizing dye within the DSSC absorbs a photon, causing an electron to be excited into the lowest unoccupied molecular orbital (LUMO) of the dye. This electron is injected in to the conduction band of the TiO_2 and then travels to the electrode. The now oxidized dye is reduced by the electrolyte, which is then regenerated at the counter electrode to complete the circuit[10].

The absorption spectra of the dyes used in these types of cells are often broad, causing them to absorb and convert photons over a wide range of wavelengths, resulting in higher currents within the cell. Examples of some of the dyes used are shown in figure 1-3.

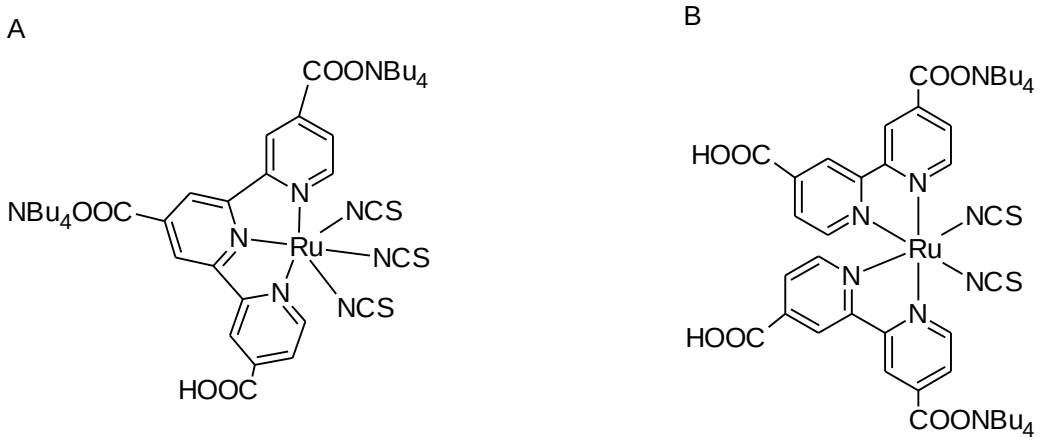

Figure 1-3 – Structures of (A) black dye N749 and (B) dye N719

Figure 1-3 shows examples of 2 dyes that are used in DSSCs. There are hundreds of possible dyes, with new ones constantly being synthesized to try and extend or improve the absorption into different parts of the electromagnetic spectrum.

Bulk Heterojunction Cells

This thesis focuses on a type of emerging solar cell, a bulk heterojunction (BHJ) cell. The general structure and different layers of a BHJ is shown in figure 1-4. Each layer within this type of cell has a specific function that will contribute to the efficiency of the cell, and each layer can be a variety of materials leading to a number of different versions of this type of cell. Each layer will be introduced and the function and materials will be discussed.

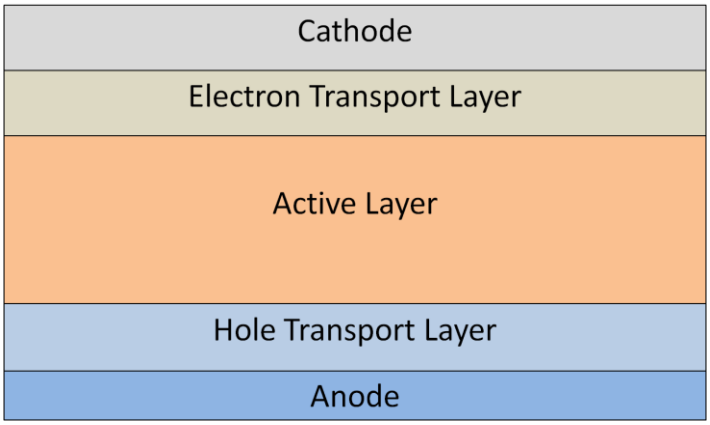

Figure 1-4 - General BHJ structure

In all types of BHJ cells the most important layer is the active layer. This layer is made up of a blend of two types of materials, a donor material and an acceptor material. This is where the solar energy is converted into electrical energy. Figure 1-5 shows how the light is absorbed into the cell and then converted into electrical energy.

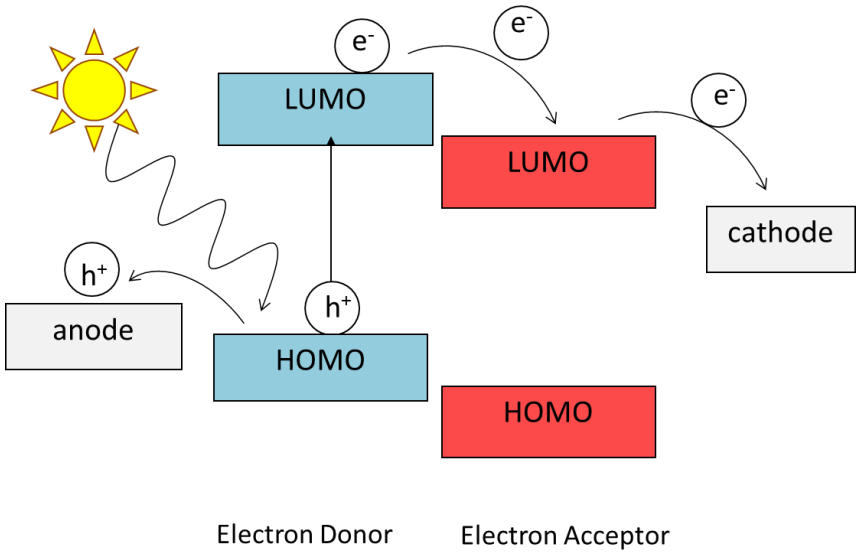

Figure 1-5 - Energy level diagram of a BHJ active layer

A photon enters the cell through the transparent anode and excites an electron from the highest occupied molecular orbital (HOMO) of the donor material into the LUMO leaving a positively charged vacancy or hole in the LUMO. This electron-hole pair is bound together while moving within the electron donor material, and is called an exciton. Once it reaches a junction between the donor material and the acceptor material, it is more favourable for the electron to move into the LUMO of the acceptor. This causes the exciton to split and the electron and the hole are free to move towards the anode and the cathode. In order for this split to occur the LUMO of the acceptor must be lower in energy than the LUMO of the donor, making it more energetically favourable for the electron to move into the new material. Once split, the hole will migrate towards the anode and the electron towards the cathode, completing the electrical circuit.

The migration of the electron and the hole towards the cathode and anode is due to band bending. The energy level diagram shown in figure 1-6(a) is of the energy levels of the materials before they are combined into a cell. Once combined, at short circuit the Fermi levels of the electrodes will attempt to equilibrate, resulting in a bent band structure as illustrated in figure 1-6(b).

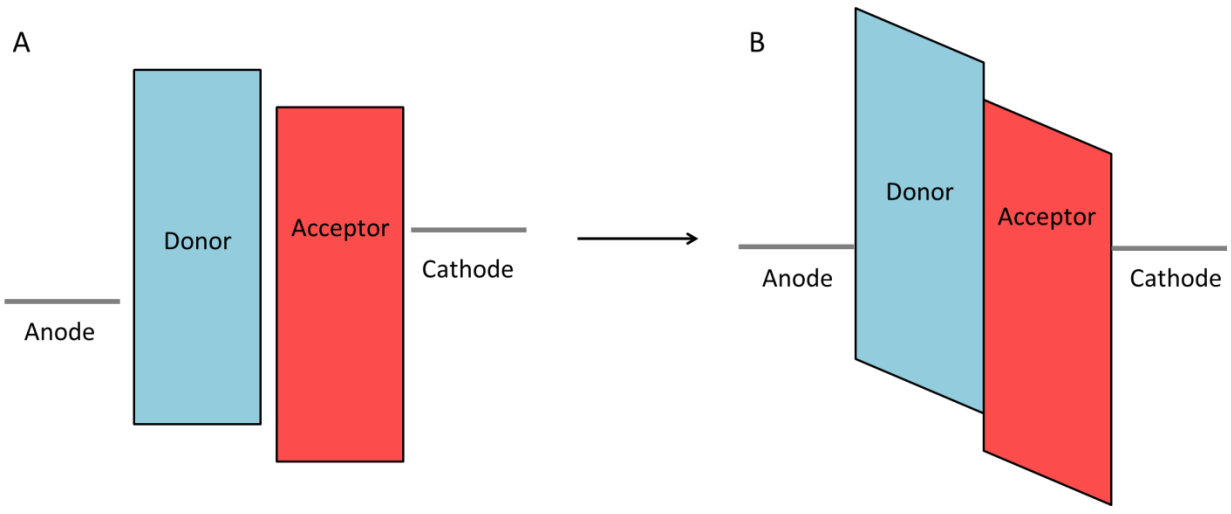

Figure 1-6 - Energy band structures of the (A) individual and (B) combined active layer materials

This creates a sloped band structure that allows for the electrons to move more favourably towards the cathode and the holes to move more favourably towards the anode. As excitons build up at the interface of the donor and acceptor materials, electrons will drift downward towards the cathode. A concentration gradient will also help to drive the electrons or holes towards the electrodes.

The acceptor is usually a fullerene, the most popular being either phenyl-C_{60}-butyric acid methyl ester or phenyl-C_{70}-butyric acid methyl ester ($PC_{60}BM$ or $PC_{70}BM$). The structure of $PC_{60}BM$ is shown in figure 1-7. Fullerenes are most often used due to their favourable LUMO energy and excellent electron transport characteristics.[11]

The donor material is often a polymer, with a large range of materials available and being used. Because $PC_{60}BM$ and $PC_{70}BM$ are well established as being effective acceptor materials, the donor materials are designed to match the band structures of these materials. One of the more popular donor materials is poly-3-hexylthiophene (P3HT), shown in figure 1-7, but other materials also work well.

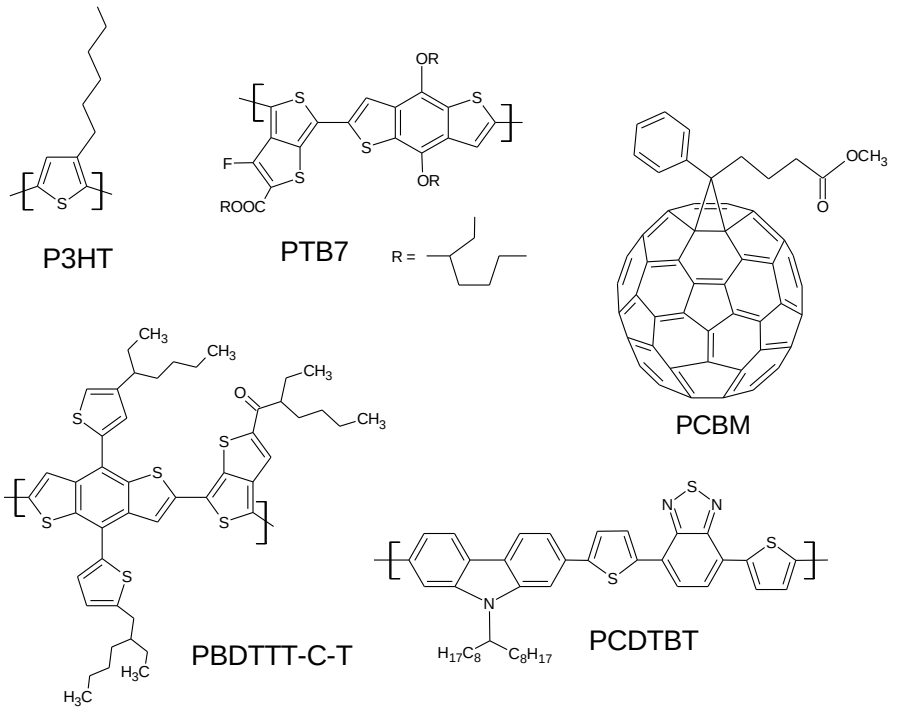

Figure 1-7 - Chemical structures of donor and acceptor materials

An important part of polymer selection are the energy levels of the polymer and how well they will overlap with the energy levels of the acceptor. The LUMO of the polymer must be higher in energy than the LUMO of the acceptor material, in order for efficient charge transfer to occur. The separation must be at least 0.3 eV in order to overcome the exciton binding energy and have charge separation occur.[12] It must be more favourable for the electron to move from the higher energy level of the polymer to the lower energy level of the acceptor. But there is a balance that needs to be maintained, and this is where the band gap becomes significant. The HOMO of the acceptor material must also be lower in energy than the HOMO of the polymer so that the hole will not transfer into the acceptor. Holes move up along the energy scale, as seen in

figure 1-5. The HOMO and LUMO levels and band gaps of some common donor-acceptor blends are shown in figure 1-8.[13,14]

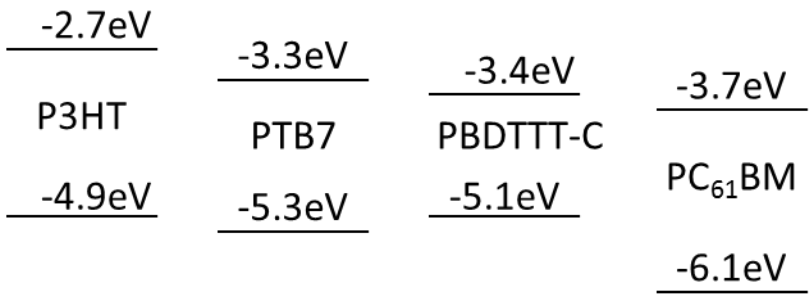

Figure 1-8 - Energy levels of multiple donor materials and PCBM acceptor material

.

Figure 1-8 shows the energy levels for the HOMOs and LUMOs with respect to vacuum for donors; P3HT, poly [[4,8-bis[[2-ethylhexyl] oxy] benzo[1,2-b 4,5b'] dithiophene-2,6-diyl][3-fluro-2-[[2-ethylhexyl]carbonyl]thieno[3,4,6] thiophene diyl]] (PTB7), Poly[*N*-9′-heptadecanyl-2,7-carbazole-*alt*-5,5-(4′,7′-di-2-thienyl-2′,1′,3′-benzothiadiazole)], Poly[[9-(1-octylnonyl)-9H-carbazole-2,7-diyl]-2,5-thiophenediyl-2,1,3-benzothiadiazole-4,7-diyl-2,5-thiophenediyl] (PCDTBT) and a poly[4,8-bis-substituted-benzo [1,2-b:4,5-b0]dithiophene-2,6-diyl-alt-4-substituted-thieno[3, 4-b]thiophene-2,6-diyl] derived polymer (PBDTTT-C), and acceptor PCBM. Table 1-1 shows efficiency values for common donor-acceptor combinations.

Table 1-1 – Efficiency values for various donor-acceptor combinations

Donor Material	**Acceptor Material**	**Power Conversion Efficiency (%)**
P3HT	$PC_{60}BM$	2.90[15]
P3HT	$PC_{70}BM$	3.49[16]
PTB7	$PC_{70}BM$	7.25[17]
PBDTTT-C-T	$PC_{70}BM$	7.59[18]
PCDTBT	$PC_{70}BM$	6.30[19]

Proper energy level alignment is not the only factor when fabricating a successful donor-acceptor blend. Film morphology is a very important factor in the active layer. The donor layer needs to be uniformly distributed throughout the cell in order to capture all of the light that enters the device. But in order for the acceptor layer to work efficiently it also needs to be distributed evenly throughout the device. This is where the idea of blending the two materials together stems from. Figure 1-9 illustrates how the blending of the donor and acceptor materials allows for even distribution of both materials.

Figure 1-9 - Film morphology of blended donor (orange) and acceptor (blue) materials

Solution processing of the active layer allows for the junctions between the donor and acceptor materials to be distributed randomly thought the cell.[20] The active layer in a cell is not the only component that helps with cell function. Hole and electron transport layers are necessary to encourage the flow of electrons in the correct direction. These buffer layers are essential for the achievement of high power conversion efficiency in organic photovoltaic (OPV) cells.[21] Between the active layer and the anode is the hole transport layer. This layer facilitates the movement of holes towards the anode. The energy levels of this layer are as important as the

energy levels in the donor acceptor blend. The work function of the popular anode indium tin oxide (ITO) is not well aligned with most donor materials[21], therefore an intermediate is required for effective hole transport from donor to anode. The HOMO level of the hole transport layer needs to lie above the HOMO of the donor material to encourage the movement of the positively charged holes into the buffer layer, and slightly below the work function of the anode to encourage movement into the anode. The LUMO also must be higher in energy in order to discourage the movement of the electrons into the hole transport layer and then on to the anode.

Along with efficiently transporting positive holes and blocking electrons, the buffer material needs to be stable and not increase the series resistance of the cell. It also must be transparent in order for light to reach the active layer.[21] Popular hole transport layers include poly(3,4-ethylenedioxythiophene):poly(4-styrenesulfonate) (PEDOT:PSS), V_2O_5, or MoO_3. While PEDOT:PSS is the most widely used in OPVs due to its ease of use, thermally evaporated metal oxides such as V_2O_5 and MoO_3 have been found to be comparable to PEDOT:PSS.[22] PEDOT:PSS, as shown in figure 1-10, is available as a suspension in water allowing for it to be spin coated on top of the anode. But there are disadvantages to the material. The suspension is extremely acidic (pH ~1-2), which may cause the ITO to lose indium. PEDOT:PSS is highly hydroscopic, and any uptake of water will damage the cell function. Also the film morphology is sometimes hard to reproduce. Solution processed materials are not the only option when looking for an effective hole transport layer.

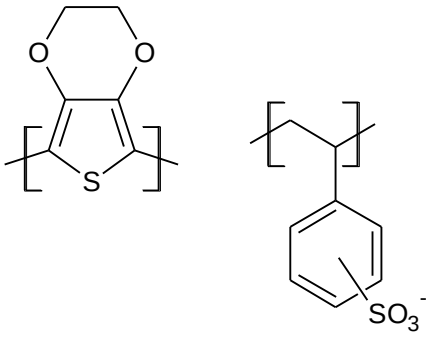

Figure 1-10 – Structure of PEDOT:PSS hole transport layer material

Other buffer layers within the cell are used to transport electrons to and block holes from the cathode. The main requirements of such a materials are to transport the negative carriers, block positive carriers, be stable, and not to increase the series resistance of the cell.[21] Lithium fluoride (LiF) is the most commonly used electron transport layer. It has been demonstrated that including a layer of LiF below the cathode leads to a significant improvement of both the fill factor and the open circuit voltage of a cell, as well as a decrease in the series resistance. This will lead to an increase in the overall efficiency.[23]

The final important components of an OPV are the anode and cathode materials. The work function of the anode is what allows for the positively charged hole to migrate towards the anode and complete the circuit within the cell. The work function of the material needs to match up with the energy level of the hole transport layer, or be very slightly higher to encourage the migration of the hole. As mentioned before, the most popular anode material is ITO on a glass substrate. The ever increasing price of indium prevents the large scale use of ITO as anode material. Other factors may limit this type of material as well. ITO has been known to release oxygen and indium into the organic layer, compromising device performance. It also has limited transparency in the blue region which may not allow for the full spectrum of light to reach the active layer.[24] On the other hand, there are few alternatives that work as well as ITO does in

OPV cells with the advantage being their use with flexible substrates. Emerging anode materials include polymer based materials, such as PEDOT based materials[25], or indium doped zinc oxide (IZO) thin films.[26]

The cathode material of a BHJ cell is much more variable than the anode. Often aluminum is used, but other metals, such as silver, gold or palladium[27] are also effective. As with the anode, the work function of the material is important. The material needs to allow for the electrons to migrate easily from the electron transport buffer layer to the cathode material.

Limitations

Limitations in BHJ devices most often originate in the active layer. There are five distinct reasons as to why there are limits in the efficiency of BHJ cells and why even the efficiency limit outlined by Shockley-Queisser[28] has yet to be reached; energy level misalignment at the donor acceptor interface, insufficient light trapping, low exciton diffusion lengths , non-radiative recombination, and low charge carrier mobilities are the cause of limited efficiencies.[29]

Insufficient light trapping is often due to the thickness of the active layer. The active layer is the part of the cell that absorbs the light. According to Beers Law, the absorbance of a material is directly related to the path length, or thickness of the material. If the active layer is too thin, the amount of light that can be absorbed is compromised. Therefore, the longer the path length, the more light can be absorbed, which should lead to an increase in efficiency of the cell.

However, increasing the thickness of the cell can create issues. Recombination can occur when the junctions between the donor and acceptor materials are far apart. The exciton must be able to diffuse to these junctions to achieve separation of the hole and the electron. If the exciton does not reach a junction within approximately 10 nm from where it was formed[30], it will recombine. This is known as geminate recombination. If the exciton does diffuse to a donor

acceptor junction before recombining, it will charge separate and the resulting hole and electron will begin to diffuse toward the anode and cathode respectively. This diffusion is also subject to recombination. If the active layer is too thick, the electron or hole may encounter another hole or electron near a donor acceptor junction and recombine within the active layer before it reaches the anode or cathode; this is known as non-geminate or bimolecular recombination. Both types of recombination are illustrated in figure 1-11

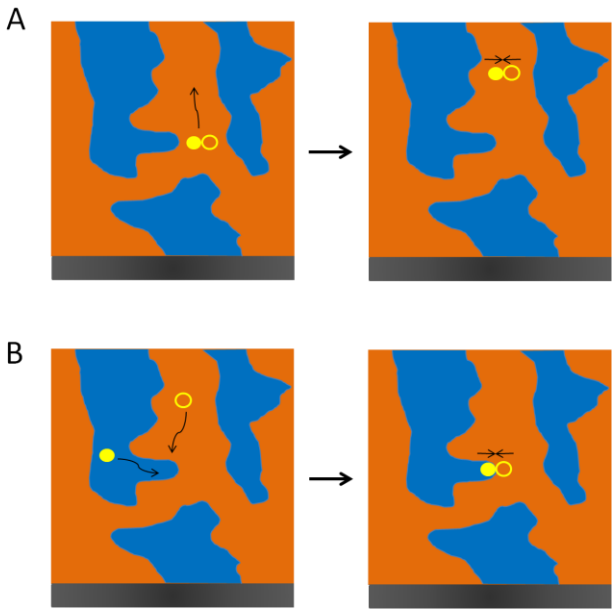

Figure 1-11 - Mechanisms of (A) geminate recombination and (B) bimolecular recombination

Charge carrier mobility is the movement of the separated positive and negative charges through the cell towards the anode and cathode. If a material has poor carrier mobility, the chances for recombination are increased. The higher the carrier mobility of a material, the more efficiently it moves the separated charges throughout the active layer. The carrier transit time within a material must be much smaller in comparison to the carrier lifetime.[31]

Most of these limitations can be controlled by careful selection of donor and acceptor materials and processing procedures. Selection of appropriate materials will help control any limitations that may arise from energy level alignment, or carrier mobilities. Careful layer fabrication will allow for reduction of limitations surrounding light trapping, exciton diffusion lengths and recombination.

If proper energy level alignment of the donor acceptor interface, adequate light trapping and low exciton diffusion lengths, recombination reduction, and high charge carrier mobility within a cell can be controlled, a well-functioning cell can be expected.

Characterization

The characterization of all types of solar cells is done in the same way, to ensure reproducibility, consistency and comparability. The efficiency and the power output of a cell are measured under specific standard conditions. The light intensity is 1000 W/m^2, the ambient temperature of the cell is 25°C, and the light spectrum used is AM1.5G. This is defined as light that has been passed through the atmosphere when the sun is at 42° elevation from the horizon[2]. Extraterrestrial light is energy that comes directly from the sun with no impedance. The light used to characterize solar cells needs to be the same as the light that would pass through the Earth's atmosphere, which contains molecules that absorb light at certain wavelengths. Figure 1-12 shows the difference between the light that reaches the edge of the earth's atmosphere (AM 0G) and the light that reaches the surface of the earth after passing through the atmosphere (AM 1.5G).

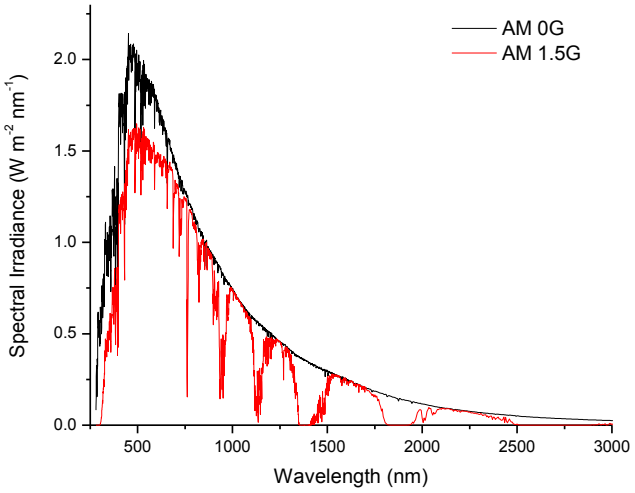

Figure 1-12 - Power density of solar radiation

Light is irradiated onto the cell, a voltage is applied and the current produced is measured. This current and voltage data is then plotted to produce a current-voltage (J-V) plot. There is a large amount of data about the cell that can be determined from this type of plot. Figure 1-13 shows an example of a J-V plot and the kinds of data that can be extracted.

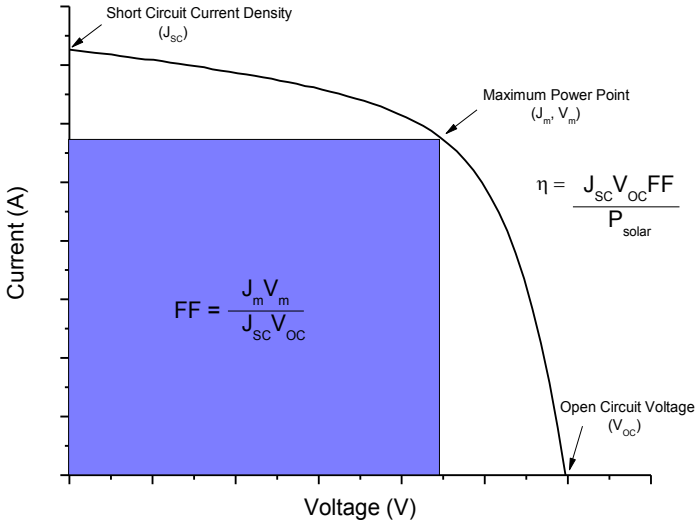

Figure 1-13 – JV curve characteristics

As shown in Figure 1-13, the efficiency of the cell can be calculated from the J-V curve of the cell. The maximum power point of the cell occurs when the power of the cell reaches its peak. The voltage at this point is the voltage at the maximum power point (V_m) and the current at the point is the current at the maximum power point (I_m). The short circuit current density (J_{SC}) of a cell is defined as the current of a solar cell when the voltage is zero divided by the area of the cell. J_{SC} values have been found to a result of active layer diffusion properties and film morphology. The more uniform the morphology, the more likely the cell to have an improved J_{SC} value[20]. The open circuit voltage (V_{OC}) is defined as the voltage within the solar cell when the current is zero. The V_{OC} of a cell has been found to be directly related to the difference in energy between the HOMO level of the donor material and the LUMO of the acceptor material in the active layer[32]. The V_m, J_m, J_{SC} and V_{OC} values are used to determine the fill factor of the cell. The fill factor (FF) is a measure of the squareness of the J-V curve and it is a representation of how difficult or easy it is to extract photogenerated carriers out of the cell.[33] Ideally the FF of a cell is 100%, where the J-V plot is a perfect rectangle. The FF, J_{SC}, and V_{OC}, are combined with incident power (P_I), the amount of light reaching the cell, to calculate the efficiency (η) of the cell. Efficiency is the parameter that is most often compared between cells, because it is a real measure of a cell's performance.

Another type of cell characterization is the incident photon to current efficiency (IPCE). This is a measure of how effectively light of a particular wavelength is converted into current. A series of current measurements is taken over a range of wavelengths and compared to a reference. The resulting data is the external quantum efficiency (EQE) and is in the form of a percentage. Equation 1-1 describes how the EQE at a certain wavelength is calculated.

$$EQE = \frac{electrons\ collected}{incident\ photons} \times 100\% \qquad (1\text{-}1)$$

Another version of this measurement is the internal quantum efficiency (IQE) this measurement is described in Equation 1-2.

$$IQE = \frac{electrons\ collected}{absorbed\ photons} \times 100\% \qquad (1\text{-}2)$$

IQE measurements take into consideration any losses that may occur from reflection in the EQE measurements. An example of an EQE measurement is shown in Figure 1-14.

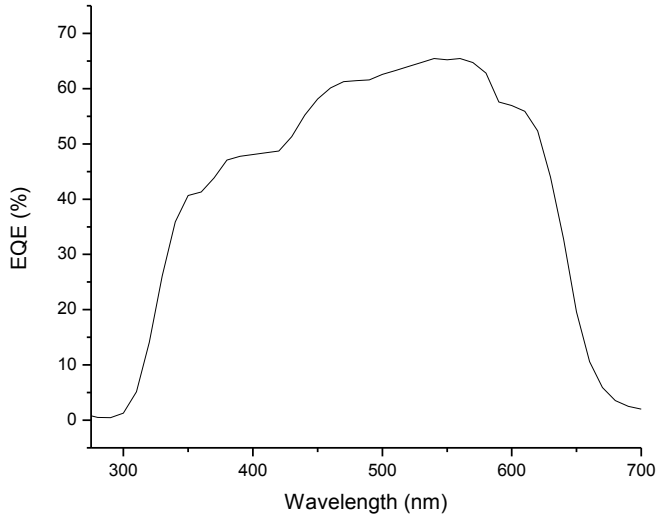

Figure 1-14 – EQE spectrum of a control P3HT:PCBM solar cell

EQE and IQE measurements are useful for determining exactly which wavelengths of light the cell is capable of converting into energy. This allows researchers to see exactly where in the electromagnetic spectrum any changes to the cell design affects the cell efficiency. It allows for a more careful cell design, to try and extend or improve the efficiency of the cell at specific wavelengths.

Plasmonics

Nanometer scale metallic structures have been used for centuries as a means to modify optical properties materials. One of the first examples of the use of nanosized particles is the

Lycurgus Cup shown in figure 1-15. The cup dates back to the ancient Roman times and is the source of an interesting phenomenon. As shown in figure 1-15, when the cup is in ambient light it appears green, but when light is passed through the glass it appears red. This is due to the presence of gold and silver nanoparticles embedded within the glass. Nanoparticles were also found as colorants in stained glass windows, illustrating how the use, but not necessarily a complete understanding, of nanoparticles goes back for centuries. Inspired by these materials, a breakthrough in the understanding the mathematical foundation surrounding nanoparticles occurred around 1900, with the formation of Mie theory in 1908.[34]

Figure 1-15 - Lycurgus Cup in ambient (left) and direct (right) light[35]

Plasmonic materials are objects that exhibit surface plasmon resonance when excited by light. When a plane wave is incident upon a nanoparticle it will be partially transmitted without deviation, partially scattered, and partially absorbed.[36] The resonance in plasmonic materials occurs when incoming light interacts with particles that are smaller than the incident light

wavelength. This phenomenon is known as localized surface plasmon resonance (LSPR), and is illustrated in figure 1-16.

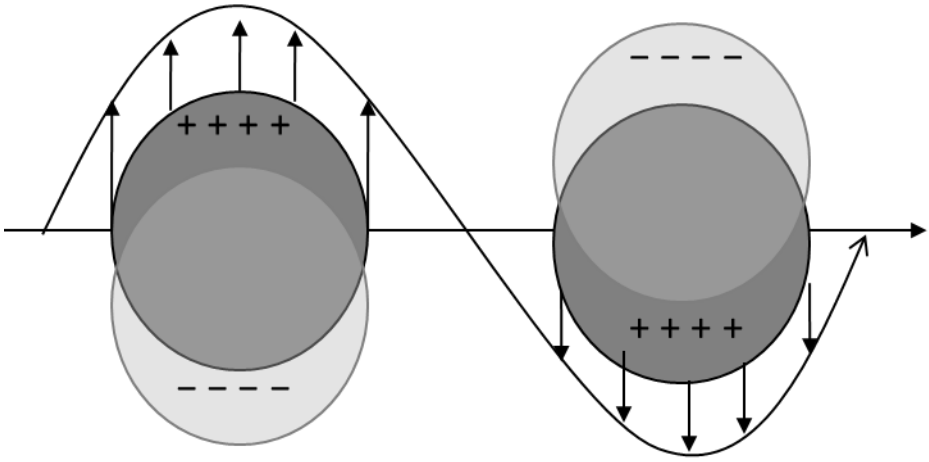

Figure 1-16 - Localized Surface Plasmon Resonance

A dipole moment is when the incident light causes a charge separation within the particle. One side of the particle will be positively charged, while the opposite side will be negatively charged, and these charges will reverse sign[37] as shown in figure 1-16. When the frequency of the incoming light matches with the frequency of the oscillation a peak in absorbance occurs. This appears as a peak in the UV-Vis spectrum and can help to characterize the size of the particle.

Shape Dependence

Peaks in the spectrum also help to characterize the shape. A uniformly sized sphere only has one spectrum peak. This is due to the shape being isotropic; there is only one axis upon which oscillation will occur. A rod shape will have two peaks, one for the oscillation along the length of the rod and one along the width. Figure 1-17 illustrates axes present in both a sphere and a rod shape.

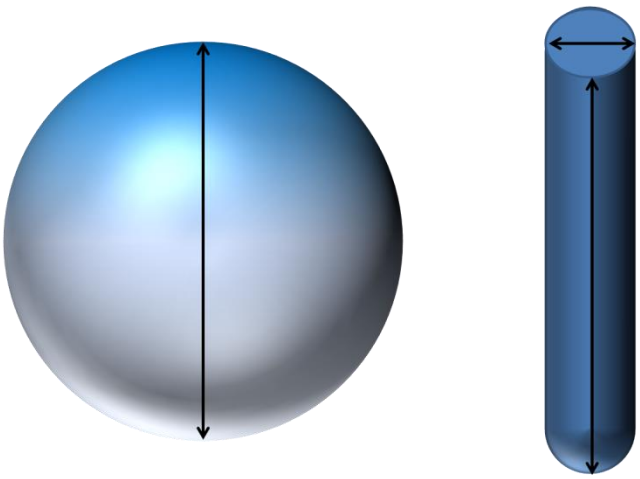

Figure 1-17 - Electron oscillation axes in a sphere and a rod

The peak wavelengths are dependent upon the distance of oscillation. As seen in figure 1-17, the sphere will have one absorption peak. The rod has an oscillation axis that is similar to the oscillation axis of the sphere, which will result in the main plasmon band having a similar peak position. However, the rod has a second oscillation axis and therefore a second plasmon peak in a different position. This much shorter axis of rod will be blue shifted compared to the main axis peak, if the axis was longer, a red shift in the peak position would occur.[36]

The position of the plasmon band of a particle is also sensitive to changes in the local dielectric environment. Typically changes in the environment, such as solvent changes or functionalization of the particles, are observed as wavelength shifts of the UV-Vis peaks in the spectrum in either the red or blue direction depending on the new environment.[38]

An increase in absorbance of near-by molecules is caused by an increase in the electric field surrounding the particle, known as near field enhancement. Figure 1-18 shows how different shapes will increase the electromagnetic field around the particle. The peaks in the UV-Vis spectra of the particles gives an indication about which part of the electromagnetic spectrum the LSPR will cause an increase in absorbance.

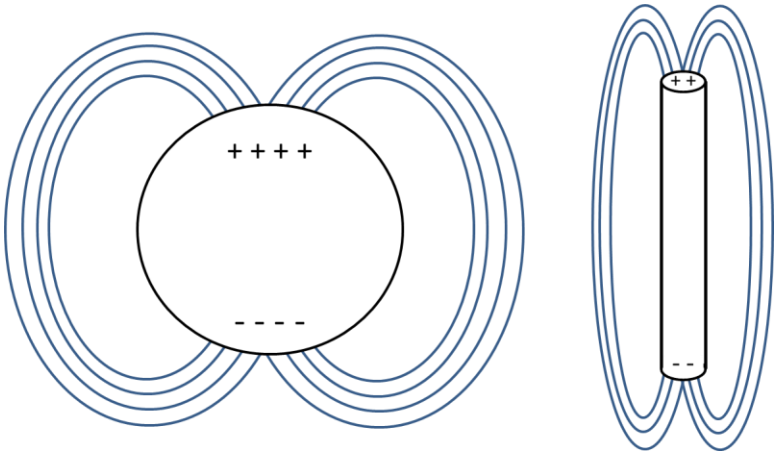

Figure 1-18 - Electric field lines of different shaped nanoparticles

Charges will accumulate in the sharp corners of particles better than at the surface of a spherical particle. This concentration of charge will concentrate the electromagnetic field to the corners. The absorbance of the material surrounding the particle will be enhanced in the areas where the electromagnetic field is enhanced. While nanoparticles with sharp tips or corners are more favourable for increasing the absorbency of their surrounding material, they are more complicated to fabricate and are more likely to decay. This thesis studies mostly silver nanoparticles.

The synthesis process for most all shapes begins with the reduction of a silver salt. It is commonly thought that there may be preferential adsorption of organic molecules such as a surfactant or a polymer to a less stable crystal face.[39] The faces that remain exposed are where the growth of the particle occurs. However this is not always the case. For example, the growth of the silver nanoprisms into its triangular shape occurs from lateral growth along the edge of the particle. Due to lamellar defects in the nanoprisms structure, the edges are what are exposed to the growth solution. The nanoprism particle begins with a hexagonal shape and a defect rich

hexagonal close packed (hcp) layer sandwiched between two uneven face centered cubic (fcc) layers. It is proposed that the more stable {111} faces will grow more slowly than the less stable {100} faces allowing for the triangular growth. [39]

The tips and corners are the vertices of high energy planes within the structure making them vulnerable to degradation. As illustrated in figure 1-19, studies have shown that the halide ions attack at the sharp points of the particle causing a rounding of the particle tips. The chloride ions can coordinate to the silver atoms and dissociate them from the structure. As more atoms are removed, more corners are created allowing for more and more atoms to dissociate until the particle is completely rounded.[40]

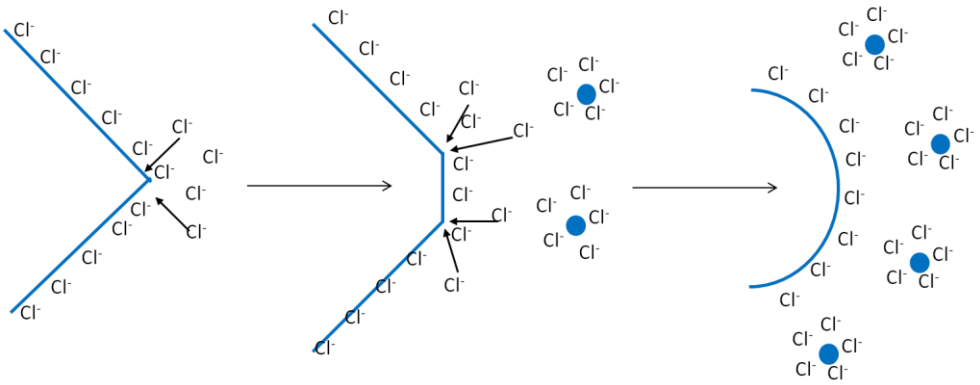

Figure 1-19 - Corner degradation mechanism from halides

Plasmon Enhanced Solar Cells

Introduction

Nanoparticles are an attractive addition to BHJ solar cells because of their plasmonic properties. By properly engineering the nanoparticles, light can be concentrated into the active layer, thereby increasing the absorption.[41] Figure 1-20(a) shows how light can be trapped in the

cell by reflection from nanoparticles. This reflection increases the path length of the light entering the cell, allowing for more light to be absorbed. Figure 1-20(b) shows that light can be trapped in the cell in the form of energy in plasmon modes. These plasmonic enhancements will increase the absorption capability of the active layer surrounding the particles.[41] When light excites the metal nanoparticle, charge separation occurs, causing an electric field to form around the particle. The absorption of the surrounding material is proportional to the square of the electric field intensity, so as electric field increases so does the absorption of the surrounding material.

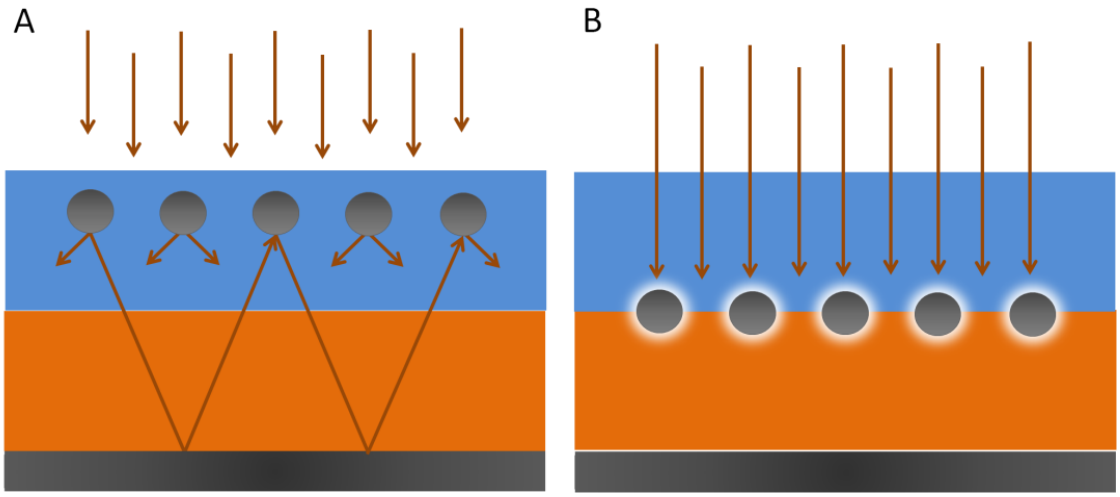

Figure 1-20 - Active layer enhancement using plasmonic particles for (a) light reflection and (b) plasmonic enhancement[41]

Plasmonic enhancements can be expected to occur at the same wavelength as the plasmon band peak in the UV-Vis absorption spectrum. This enhancement is a result of the enhancement of the electric field surrounding the particle. As the electric field of the

Shape, Size and Nanoparticle Materials

A number of research groups have incorporated nanoparticles of different shapes, sizes and materials into solar cells. The two most commonly used materials are silver and gold, but alloys containing these materials are also being studied[15,42]. The most common active layer is a P3HT:PCBM blend, but as mentioned before, other acceptor polymers such as PT7B and PCDTBT are also being examined. [17,19,43]

Similar to this thesis, there are a few different ways nanoparticles have been incorporated into solar cells. Some groups incorporate them into the active layer, some in the PEDOT:PSS hole transport layer, others below the hole transport layer.

The groups that incorporated nanoparticles into the active layer did so using different types and sizes of particles. Wang et al. used 40 nm Ag nanoclusters[19] and in another study used 70 nm octahedral Au nanoparticles[16], Li et al. used of 20 nm Ag nanospheres, 60 nm Ag nanoprisms, and a combination of the two[44], Choi et al. used silica coated 50 nm Ag nanoprisms[17], and Chen et al. used a 20 nm spherical AuAg alloy in their cells.[42] Each group was successful in obtaining an efficiency enhancement upon nanoparticle incorporation. In their PCDTBT:PCBM cell, Wang et al. report an efficiency enhancement in their polymer solar cells from 6.30% to 7.10%.[19] This study looked at adding into the active layer by adding small silver nanoparticles to the aqueous active layer and then spin coating the mixture onto the cell. The spin coating is what causes the larger Ag clusters to form.[19]

Li et al. fabricated P3HT:PCBM cells and upon addition of Ag nanoparticles saw an efficiency enhancement from 3.60% to as high as 4.30%.[44] In their Ag study the group incorporated two different shaped and sized particles into their cells. Upon the addition of 20 nm Ag nanospheres to the active layer, the cell performed with an efficiency of 3.99%. When 60 nm

Ag nanoprisms were incorporated into the P3HT:PCBM layer, the cells showed an efficiency of 4.07%. When both shapes were combined evenly into the active layer, the cells showed their maximum efficiency of 4.30%.[44] They also incorporated 70 nm octahedral Au into P3HT:PCBM cells. The addition of the particles increased the cell efficiency from 3.49% to 4.36%.[16] In both studies the active layer was sonicated before spin-coating on to the cell to try and avoid the agglomeration of the Au particles.

A SiO_2 shell was chosen by Choi et al. to coat and protect their Ag nanoprisms.[17] The shell is designed to protect the LSPR effect of the Ag nanoparticles by preventing the oxidation of the Ag core and also to eliminate any concern about exciton quenching by preventing direct contact of the Ag with the active layer. The 50 nm Ag particles coated with a 10 nm SiO_2 shell were incorporated into either the PTB7:PCBM active layer, or the PEDOT:PSS hole transport layer of the cell and then compared to a reference. The study found that the cells with the particles in the hole transport layer of the cell saw an increase in efficiency from 7.26% to 7.98%, and the cells with the particles in the active layer of the cell saw the efficiency increase to 8.49%.[17]

A combination of both Ag and Au in the form of an alloy was used by Chen et al. in their cells. The study found that there is an optimal ratio of Ag to Au in the particles in order to reach maximum cell efficiency. The group synthesized ~20 nm $Au_{11}Ag_{89}$ particles and incorporated them in to the P3HT:PCBM active layer of the cell. The cells with the alloy particles increased in efficiency from 3.61% to 4.73%. [42]

Research groups have also incorporated nanoparticles into the hole transport layer of their cells. In all cases the hole transport layer used was PEDOT:PSS. Lu et al. used a combination of 40 – 50 nm Au and Ag particles[43], Wu et al. incorporated 45 nm octahedral Au nanoparticles[45],

and Fung et al. used 20 nm spherical Au nanoparticles that had been coated in with poly(ethylene glycol) (PEG).[46] All of these cells also exhibited an increase in efficiency.

The active layer used by Lu et al. in their cells was PTB7:PCBM. The spherical 40-50 nm Ag and Au particles were studied separately and in equal combination in the PEDOT:PSS layer of the cells. The cells that only had the Ag nanoparticles in the hole transport layer showed an efficiency improvement from 7.25% to 8.01%, the cells with only Au nanoparticles showed a maximum efficiency of 8.16%, and when the two materials were combined the maximum efficiency obtained was even higher, 8.67%.[43]

Wu et al fabricated cells using P3HT: PCBM as the active layer. After integrating 45nm octahedral Au nanoparticles into the hole transport layer, the cell efficiency increased from 3.57% to 4.24%. Even though the particles are not in the active layer, the particle size suggests that most of the efficiency enhancement comes from LSPR effects. A particle larger than 100 nm will contribute more to light scattering effects. The 45 nm particles in this study were presumably unable to induce effective light scattering into the cell, concluding that the LSPR effects is what is contributing to the cell efficiency enhancement.[45]

Fung et al. incorporated 20 nm spherical Au nanoparticles in to the PEDOT:PSS hole transport layer of their P3HT:PCBM BHJ cell. Instead of using bare Au particles, the nanoparticles were first functionalized with PEG in order to prevent aggregation of the nanoparticles within the hole transport layer. When the bare Au nanoparticles were incorporated into the PEDOT:PSS layer, there was no observed efficiency enhancement, but when the PEG coated Au nanoparticles were integrated the cell efficiency increased from 3.10% to 3.51% .[46]

Heo et al. incorporated a AuCu alloy into P3HT:PCBM based BHJ cell. These 25 nm hexagonal particles were positioned between the ITO anode and the PEDOT:PSS buffer layer.

The AuCu alloy material as well as pure Au and pure Cu nanoparticles were compared to a reference cell. All of the particles were formed on the ITO using a copolymer template. The cells with the 25 nm Au particles demonstrated an efficiency enhancement from 2.90% to 2.98%. The cells with only the Cu particles showed an average efficiency of 3.22%, and the cells with the AuCu alloy showed an average efficiency of 3.35%. The attractiveness of a bimetallic device is that the absorption wavelengths of the material have a much broader range than a monometallic material. This should enhance the absorption of the BHJ cell across a broader part of the solar spectrum.[15]

Table 1-2 shows a summary of the types of devices discussed above.

Table 1-2 - Efficiency improvements of BHJ cells containing nanoparticles

Particle Material	Shape / Size	Placement	Active Layer Material	Efficiency Before Integration	After Integration	Reference
Ag	Clusters / 40nm	In Active Layer	PCDTBT:PCBM	6.30 %	7.10 %	19
Ag	Spheres / 20nm & Prisms / 60nm	In Active Layer	P3HT:PCBM	3.60 %	4.30 %	44
Ag@SiO2	Prisms / 50nm	In Active Layer	PTB7:PCBM	7.26 %	8.49 %	17
AgAu alloy	Spherical / 20nm	In Active Layer	P3HT:PCBM	3.61 %	4.73%	42
Ag + Au	Spherical / 40-50nm	In PEDOT:PSS	PTB7:PCBM	7.25 %	8.67 %	43
Au	Octahedral / 45nm	In PEDOT:PSS	P3HT:PCBM	3.57 %	4.24 %	45
Au	Octahedral / 70nm	In Active Layer	P3HT:PCBM	3.49 %	4.36 %	16
PEG coated Au	Spherical / 20nm	In PEDOT:PSS layer	P3HT:PCBM	3.10 %	3.51 %	46
AuCu alloy	Hexagonal / 25nm	Between anode and hole transport layer	P3HT:PCBM	2.90%	3.35%	15

There are a number of types of materials in a many shapes and sizes that are being studied. This thesis will look at incorporating protected Ag nanoprisms and spheres into the active layer, and under the hole transport layer of a P3HT:PCBM based device.

References

(1) Gelman, R. 2011 Renewable Energy Data Book; National Renewable Energy Laboratory, 2011.

(2) Chen, C. J. In Physics of Solar Energy John Wiley & Sons, Inc.: 2011, p 1.

(3) National Center for Photovoltaics: 2013.

(4) Burnett, B.; Laboratory, N. R. E., Ed. United States, 2002.

(5) Harris, W. In HowStuffWorks.com 2008; Vol. 2013.

(6) In Nanosolar.com 2013; Vol. 2013.

(7) Grätzel, M. Journal of Photochemistry and Photobiology C: Photochemistry Reviews 2003, 4, 145.

(8) Trimarchi, M. In HowsStuffWorks.com 2009.

(9) Burschka, J.; Pellet, N.; Moon, S.-J.; Humphry-Baker, R.; Gao, P.; Nazeeruddin, M. K.; Gratzel, M. Nature 2013, 499, 316.

(10) Hardin, B. E.; Snaith, H. J.; McGehee, M. D. Nature Photonics 2012, 6, 162.

(11) Facchetti, A. Materials Today 2013, 16, 123.

(12) Tsang, S.-W.; Chen, S.; So, F. Advanced Materials 2013, 25, 2433.

(13) McNeill, C. R.; Abrusci, A.; Zaumseil, J.; Wilson, R.; McKiernan, M. J.; Burroughes, J. H.; Halls, J. J. M.; Greenham, N. C.; Friend, R. H. Applied Physics Letters 2007, 90, 193506.

(14) Liang, Y.; Xu, Z.; Xia, J.; Tsai, S.-T.; Wu, Y.; Li, G.; Ray, C.; Yu, L. Advanced Materials 2012, 22, E135.

(15) Heo, M.; Cho, H.; Jung, J.-W.; Jeong, J.-R.; Park, S.; Kim, J. Y. Advanced Materials 2011, 23, 5689.

(16) Wang, D. H.; Kim, D. Y.; Choi, K. W.; Seo, J. H.; Im, S. H.; Park, J. H.; Park, O. O.; Heeger, A. J. Angewandte Chemie International Edition 2011, 50, 5519.

(17) Choi, H.; Lee, J.-P.; Ko, S.-J.; Jung, J.-W.; Park, H.; Yoo, S.; Park, O.; Jeong, J.-R.; Park, S.; Kim, J. Y. Nano Letters 2013, 13, 2204.

(18) Li, X.; Choy, W. C. H.; Huo, L.; Xie, F.; Sha, W. E. I.; Ding, B.; Guo, X.; Li, Y.; Hou, J.; You, J.; Yang, Y. Advanced Materials 2012, 24, 3046.

(19) Wang, D. H.; Park, K. H.; Seo, J. H.; Seifter, J.; Jeon, J. H.; Kim, J. K.; Park, J. H.; Park, O. O.; Heeger, A. J. Advanced Energy Materials 2011, 1, 766.

(20) Ray, B.; Lundstrom, M. S.; Alam, M. A. Applied Physics Letters 2012, 100, 013307.

(21) Po, R.; Carbonera, C.; Bernardi, A.; Camaioni, N. Energy & Environmental Science 2011, 4, 285.

(22) Shrotriya, V.; Li, G.; Yao, Y.; Chu, C.-W.; Yang, Y. Applied Physics Letters 2006, 88, 073508.

(23) Brabec, C. J.; Shaheen, S. E.; Winder, C.; Sariciftci, N. S. Applied Physics Letters 2002, 80, 1288.

(24) Na, S.-I.; Kim, S.-S.; Jo, J.; Kim, D.-Y. Advanced Materials 2008, 20, 4061.

(25) Yanfei Xu; Yan Wang; Jiajie Liang; Yi Huang; Yanfeng Ma; Xiangjian Wan; Chen, Y. Nano Research 2009, 2, 343.

(26) Hu, Z.; Jiao, B.; Zhang, J.; Zhang, X.; Zhao, Y. International Journal of Photoenergy 2011, 2011.

(27) Mihailetchi, V. D.; Blom, P. W. M.; Hummelen, J. C.; Rispens, M. T. Journal of Applied Physics 2003, 94, 6849.

(28) Shockley, W.; Queisser, H. J. Journal of Applied Physics 1961, 32, 510.

(29) Kirchartz, T.; Taretto, K.; Rau, U. The Journal of Physical Chemistry C 2009, 113, 17958.

(30) Li, G.; Zhu, R.; Yang, Y. Nature Photonics 2012, 6, 153.

(31) Pivrikas, A.; Sariciftci, N. S.; Juška, G.; Österbacka, R. Progress in Photovoltaics: Research and Applications 2007, 15, 677.

(32) Brabec, C. J.; Cravino, A.; Meissner, D.; Sariciftci, N. S.; Fromherz, T.; Rispens, M. T.; Sanchez, L.; Hummelen, J. C. Advanced Functional Materials 2001, 11, 374.

(33) Qi, B.; Wang, J. Physical Chemistry Chemical Physics 2013, 15, 8972.

(34) Maier, S. A. Plasmonics: Fundamentals and Applications; Springer: Bath, UK, 2007.

(35) The British Museum: 2013.

(36) Sarid, D.; Challener, W. A. Modern introduction to surface plasmons : theory, Mathematica modeling, and applications; Cambridge University Press: Cambridge, 2010.

(37) Wiley, B. J.; Im, S. H.; Li, Z.-Y.; McLellan, J.; Siekkinen, A.; Xia, Y. The Journal of Physical Chemistry B 2006, 110, 15666.

(38) Willets, K. A.; Van Duyne, R. P. Annual Review of Physical Chemistry 2007, 58, 267.

(39) Aherne, D.; Ledwith, D. M.; Gara, M.; Kelly, J. M. Advanced Functional Materials 2008, 18, 2005.

(40) An, J.; Tang, B.; Zheng, X.; Zhou, J.; Dong, F.; Xu, S.; Wang, Y.; Zhao, B.; Xu, W. The Journal of Physical Chemistry C 2008, 112, 15176.

(41) Atwater, H. A.; Polman, A. Nat Mater 2010, 9, 205.

(42) Chen, H.-C.; Chou, S.-W.; Tseng, W.-H.; Chen, I. W. P.; Liu, C.-C.; Liu, C.; Liu, C.-L.; Chen, C.-h.; Wu, C.-I.; Chou, P.-T. Advanced Functional Materials 2012, 22, 3975.

(43) Lu, L.; Luo, Z.; Xu, T.; Yu, L. Nano Letters 2012, 13, 59.

(44) Li, X.; Choy, W. C. H.; Lu, H.; Sha, W. E. I.; Ho, A. H. P. Advanced Functional Materials 2013, 23, 2728.

(45) Wu, J.-L.; Chen, F.-C.; Hsiao, Y.-S.; Chien, F.-C.; Chen, P.; Kuo, C.-H.; Huang, M. H.; Hsu, C.-S. ACS Nano 2011, 5, 959.

(46) Fung, D. D. S.; Qiao, L.; Choy, W. C. H.; Wang, C.; Sha, W. E. I.; Xie, F.; He, S. Journal of Materials Chemistry 2011, 21, 16349.

Chapter 2 – Surface Functionalization for Phase Transfer of Silver Nanoprisms

Introduction

The particle shapes used in this study are triangular plates or prisms. By using different shaped particles, the way the LSPR affects the surrounding media can be tuned. Figure 1-18 illustrates the electric field that forms around different shaped particles in response to charge separation within the particle. The magnitude of the enhanced electric field intensity is increased where there are more electric field lines.

The rod shaped particle, with distinct ends, has a much larger electric field at its tips than the edges of the rounded particle. This enhanced electric field allows the active layer to have an increased absorption cross-section; by absorbing more light, more current will be able to flow through the cell.[1] This shows how a particle with corners such as cubes or prisms is a more favourable choice for incorporation into devices.

Cubes are an extremely difficult shape to produce, so even though they could contribute to a large electric field enhancement, they are not a sensible choice. Cube syntheses are time consuming, extremely particular about solvent and chemicals used, and inconsistent in producing the cube shape.[2] A much easier particle shape to synthesize that still has sharp corners is a triangular prism. Prisms syntheses[3,4] are fast and reliable, they are easily reproducible and can be scaled up to produce large quantities. However, the syntheses are done in aqueous solution and then do not allow for the particles to be phase transferred into the organic solvent needed for BHJ cell fabrication. In some cases nanoparticles can be easily phase transferred into organic solvents such as hexanes[5], but often in order to be soluble in other solvents such as chloroform, they will need to be functionalized. There are a number of ways to modify the surface of the

nanoparticles. They can be passivated with a silica shell[6], functionalized with 16-mercaptohexadecanoic acid (MHA)[7,8], or with thiol-terminated PEG-SH[9] in order to be solubilized in a number of different organic solvents.

Given the stability and versatility of alkane thiols in functionalizing silver surfaces[10], PEG-SH was chosen as a ligand to modify the surface chemistry of the silver nanoprisms. The long alkyl chain of the PEG-SH was also chosen to allow for the solubility of the particles in the organic solvents necessary for incorporation into the BHJ cells as the bare particles themselves are insoluble in organic solvents. Incorporation of the particles into the solvent and BHJ cells can be done without particle functionalization[11-14], but if the particles are truly and completely soluble by functionalizing the surface, aggregation and particle settling within the cell can be avoided.

Despite the sharp nanoprism tips being beneficial, the morphology of the particle is not long lasting. Over time the particles degrade and change in shape from triangular plates with sharp, well defined corners to circular disk-like plates. Recent work has demonstrated that silver nanoprisms can be quickly etched into disk shaped nanoplates by halide ions, such as Cl^-, Br^-, or I^-.[7,15,16] It has been reported that functionalization with thiols may terminate or slow this shape transformation by passivating surface sites.[7] However our work demonstrates a shape change is similar to the halide etching when Ag nanoprisms are functionalized with PEG-SH. Better control over particle shape is critical for the plasmonic applications of the particles, where the rounding of the particle corners is expected to have a detrimental effect on the electric field enhancement as illustrated in figure 1-18.

In order to study and fully understand this degradation mechanism of the nanoprism rounding, UV-Vis measurements and X-ray Absorption Near Edge Structure (XANES) were

done. XANES uses a high energy X-ray photon beam to excite electrons from core orbitals (1s, 2s, 2p etc.) into empty conduction band orbitals.[17] In this study, electrons from the 2p orbitals, specifically the $2p_{3/2}$ electrons of Ag atoms are excited. The measured Ag L_3-edge XANES are the transitions from the 2p orbital and are highly sensitive to the oxidation state of Ag.[18,19] The selection rule $\Delta l = \pm 1$ states that the 2p electrons can only be excited into either the d orbital ($\Delta l = +1$) or the s orbital ($\Delta l = -1$). The p → d transition is much stronger than the p → s transition, but due to the d-s orbital hybridization both transitions are observable.[19] Since all of the d states are full in the ground state of Ag, the XANES of Ag metal will be featureless. Upon the loss of an electron (oxidation), there is an increase in the number of unoccupied d states, resulting in a small peak and the absorption threshold (white-line) and is seen in compounds such as Ag_2S and $AgNO_3$. The K-edge of S is also monitored, and follows the transition of a S 1s electron to the unoccupied 3p states. This can be used to study the oxidation state of various S-containing organic compounds as well as inorganic minerals.[20-22]

UV-Vis measurements compared different molecular weights and concentrations of PEG-SH, as well as the effects of the different concentrations on the size and shape transformation. To fully understand the mechanism of the PEG-ylation reaction, XANES at the Ag L_3-edge and the S K-edge are measured before, during, and after the PEG-ylation reaction. The chemical speciation of Ag and S before and after PEG-ylation is explained and a reaction mechanism is proposed for the shape transformation process.

Experimental

Silver Prism Synthesis

Silver nanoprisms were synthesized according to literature procedures[4]. Trisodium citrate (1 mL, 75 mM), silver nitrate (100 μL, 50 mM), poly(vinyl pyrrolidone) (200 μL, 17.5 mM), and

hydrogen peroxide (120 μL, 30%wt) are rapidly stirred in 48.08 mL H_2O. Sodium borohydride (500 μL, 100 mM) is quickly injected and the solution is allowed to stir for 2 hours. Once the reaction was completed, indicated by the solution turning dark blue, the solution was centrifuged at 13000 rpm for 2 hours. The supernatant was removed and the final volume was brought to 25 mL using 5 mM trisodium citrate.

PEG-ylation of Nanoprisms

1 mL of PEG-thiol solution (0.3 mM) in trisodium citrate was added to 2 mL solution of silver nanoparticles in 5 mM trisodium citrate. The solution was stirred vigorously for approximately 15 minutes.

XANES

XANES measurements were conducted at the Soft X-ray Microcharacterization Beamline (SXRMB) at the Canadian Light Source. The beamline is equipped with a double-crystal monochromator using either InSb (111) or Si (111) crystals[23]. XANES spectra were obtained in the mode of X-ray fluorescence yield. The X-ray fluorescence was measured using a 4-element Si(Li) drift detector. For measurements on solid powders, the samples were spread on double-sided carbon tape pieces and attached to the sample holder, which was placed at 45° toward the incident beam. Measurements were then completed under vacuum. Solution samples were filled into polypropylene cells, and sealed with X-ray transparent film (Ultralene® film, 4 μm thick). The sample cell is placed on the sample holder that faces the incident beam at 45° in an aluminum box. During the measurements, the box is purged with helium to provide an air-free environment.

Results and Discussion

Nanoprism Synthesis

The UV-Vis data and TEM images and size distribution data for the particles are shown in figures 2-1, 2-2 and 2-3. From the TEM images as shown in figure 2-2 it is apparent that the reaction did successfully create prism shaped particles, with a narrow size distribution. The average prism size shown in figure 2-3, calculated from the TEM images, is 25 ± 9 nm.

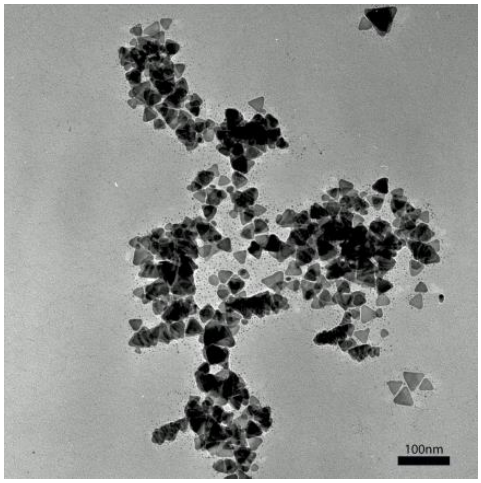

Figure 2-1 - TEM image of Ag nanoprisms

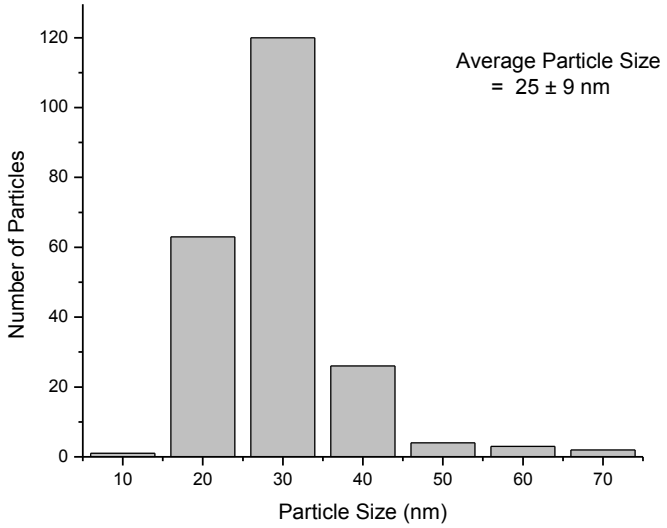

Figure 2-2 - Size distribution of Ag nanoprisms

The main peak in the UV-Vis spectrum shown in figure 2-4 is at 655 nm. This is the peak that corresponds to the main in-plane dipole of the prisms and the small peak that occurs at approximately 335 nm is likely due to the out-plane quadrupole LSPR mode within the particle.[24] The shoulder that occurs at 460 nm could be due to an in plane quadrupole mode.[25]

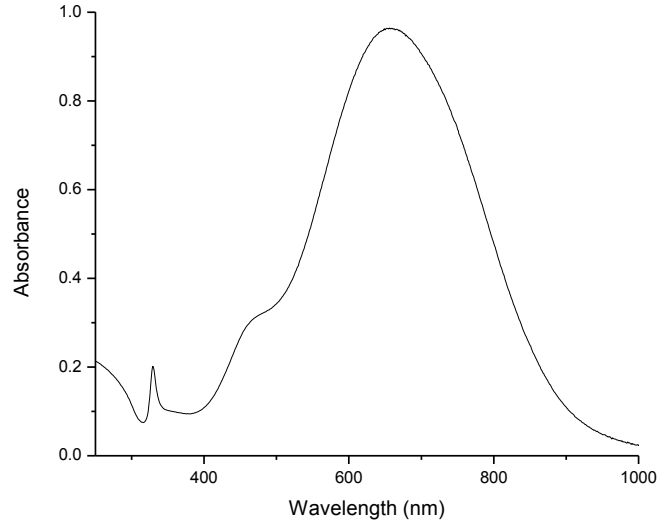

Figure 2-3 - UV-Vis spectrum of Ag nanoprisms

The dipole and quadrupole mode arise from the charge separation in the nanoparticle. Figure 2-4 illustrates these two types of charge separation.

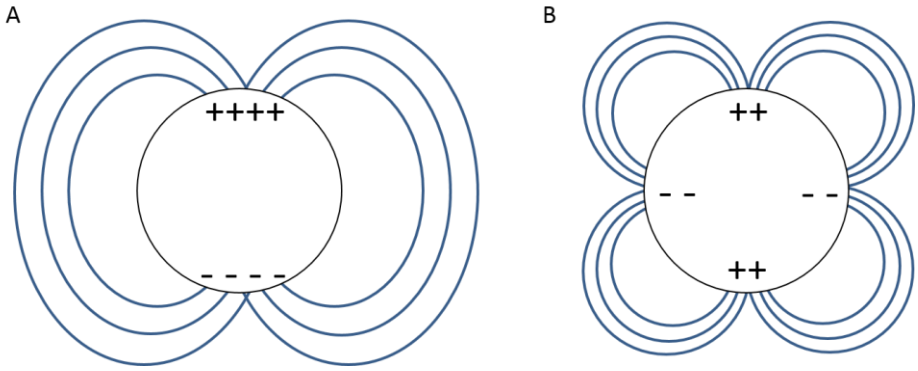

Figure 2-4 – (a) Dipole and (b) quadrupole charge separation

PEG-ylation of Nanoprisms

In order to properly integrate these PEG-SH functionalized particles into BHJ cells, the degradation mechanism also needs to be understood. Silver nanoprisms are known to degrade by a rounding of the tips into disk-like plate structures. This is not beneficial for incorporation into BHJ cells, because the enhancement from the sharp tips is lost. Here, a kinetic and mechanistic study on the PEG-ylation of Ag nanoprisms using in situ UV-Visible spectroscopy and in situ solution phase XANES is reported.

A number of PEG-SH of varying molecular weights were reacted in various concentrations with triangular Ag nanoprisms. Because the LSPR bands of the Ag nanoprisms are sensitive to the particle shape, monitoring the evolution of the UV-Vis absorption features as a function of time, will lead to being able to follow the transformation of the particle shape in real time. However, while the UV and visible region of the spectrum can provide information about nanoparticle shape and size, no information about other components of the reaction

mixture, such as Ag^{+}, very small Ag^{0} clusters, or the PEG-SH can be retrieved. In contrast, the use of XANES makes it possible to gain necessary information on the Ag and PEG-SH local environments during the PEG-ylation reaction.

First the effect of PEG-SH concentration on the underlying Ag nanoprism morphology is investigated. PEG-ylation of the Ag nanoprisms was carried out using 1 kDa molecular weight PEG-SH of 0.1 mM and 1 mM total concentration (based on the mass of the repeat unit). The evolution of the Ag nanoprism UV-Vis spectra are shown as contour plots in Figure 2-5. The color-coding of the optical density is the same for all graphs. It can be seen that the LSPR bands exhibit pronounced shifts as a function of reaction time, indicating that there are substantial changes in the Ag nanoprism's size and shape over the course of the reaction.

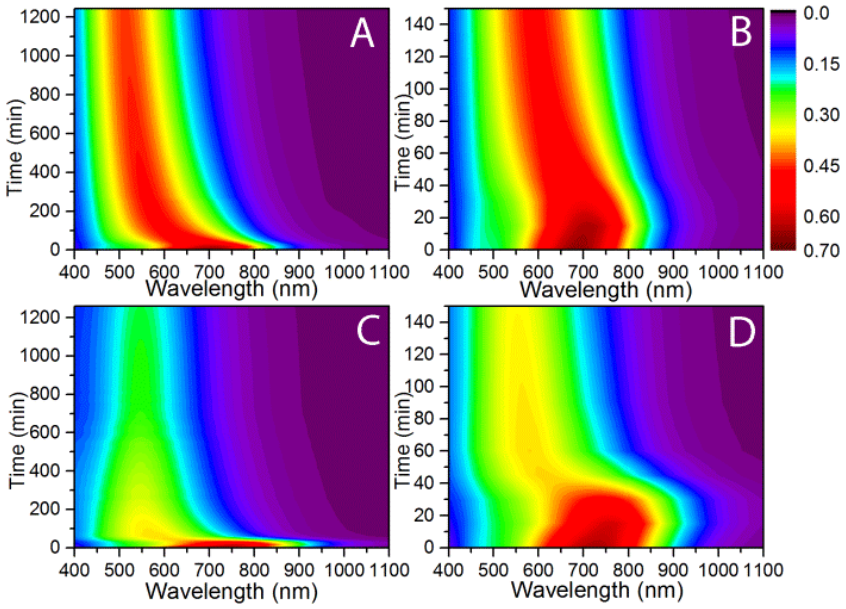

Figure 2-5 - UV-Vis contour plots of Ag nanoprisms reacting with 0.1 mM 1 kDa PEG-SH from (a) 0 – 1200 minutes and (b) 0 – 150 minutes, and Ag nanoprisms reacting with 1 mM 1 kDa PEG-SH from (c) 0 – 1200 minutes and (d) 0 – 150 minutes. The scale bar on the right represents the intensity of the UV-Vis spectra.

Figure 2-5(a) shows the Ag nanoprisms reacting with 0.1 mM PEG-SH from 0 – 1200 minutes, and (b) shows the first 0 to 150 minutes of 0.1 mM PEG-SH reacting with the Ag nanoprisms. As seen in this expanded view of the reaction, the in-plane dipole band of the Ag nanoprisms initially undergoes a 27 nm red shift. The band then gradually undergoes a blue shift, along with a simultaneous decrease in peak intensity. After 120 minutes the peak intensity decreases more slowly but the peak shift remains steady throughout the reaction.

Figure 2-5(c) shows the Ag nanoprisms reacting with 1 mM PEG-SH from 0 – 1200 minutes, and (d) shows the first 0 to 150 minutes of 1 mM PEG-SH reacting with the particles. The expanded view still shows the initial red-shift, but this is followed by a much more pronounced blue-shift. The maximum peak intensity also drastically decreases during the first 40 min of the reaction. After 3 hours, the blue-shift stops and the center of the LSPR band remains at 545 nm as seen in figure 2-5(c). However, the peak intensity keeps decreasing throughout the course of the entire reaction.

The UV-Vis spectra of both concentrations of PEG-SH reacting with Ag nanoprisms exhibit the same trend of an initial red-shift followed by a blue-shift. However, the magnitude and rate of the blue-shift appears to be dependent on the PEG-SH concentration. The red-shift can be easily explained due to the increase in the local dielectric environment upon thiol coordination to the Ag surface. Blue-shifts of the plasmon band are generally due to a decrease in the nanoparticle aspect ratio, which could be due to either a decrease in particle edge length or a truncation of the nanoprism tips. The morphology of the Ag nanoprisms during the course of the PEG-ylation reaction is examined by TEM and presented in Figure 2-6. Since the most noticeable changes in the UV-Vis spectra occur within the first two hours, TEM images were also taken of the particles after two hours of reaction time, as well as of the final product.

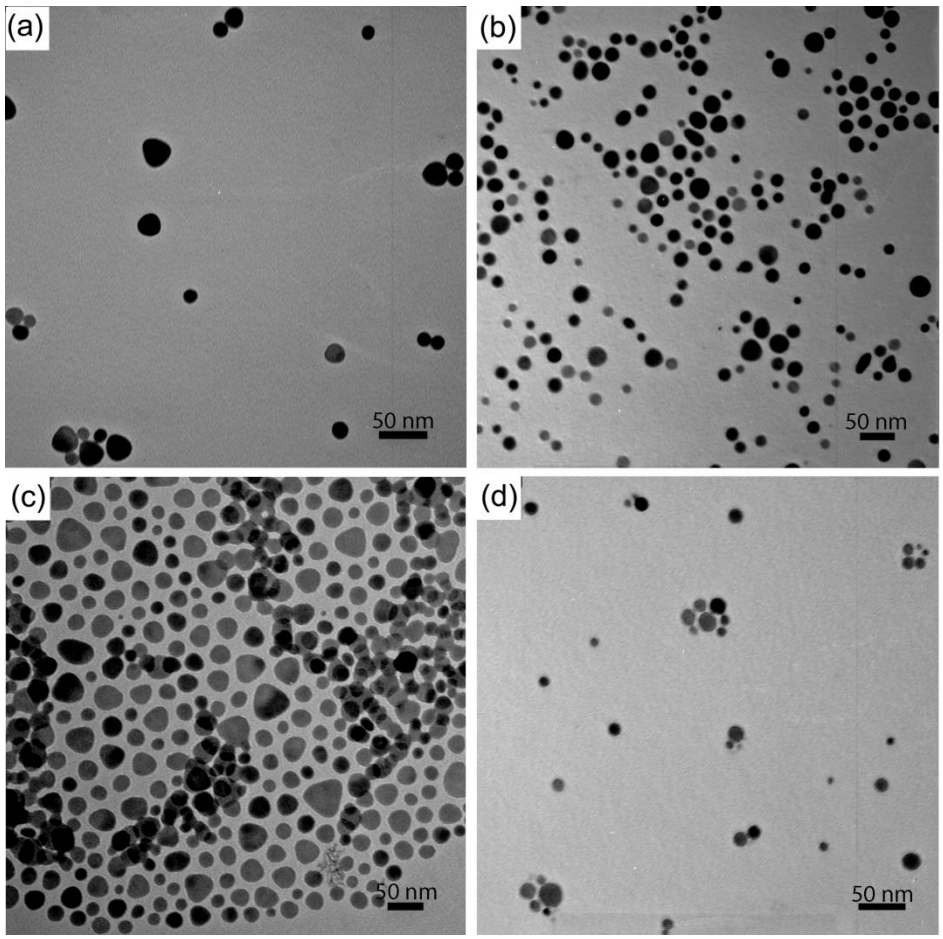

Figure 2-1 - TEM images of Ag nanoprisms reacting with 0.1 mM 1 kDa PEG-SH for (a) 2 hours and (b) 20 hours, and 1 mM 1 kDa PEG-SH for (c) 2 hours and (d) 20 hours.

Figure 2-6 shows the morphology of the Ag nanoprisms reacting with 0.1mM 1 kDa PEG-SH after (a) 2 hours and (b) 20 hours. It is shown that the 0.1 mM PEG-SH causes the Ag nanoprisms to undergo a morphology change from triangular to disk-like plates. The tips of the particles after 2 hours are no longer as sharp as the as synthesized particles and the average size of the nanoparticles decreases over time to approximately 15-27 nm, but the size distribution is now very broad. After 20 hours, most of the particles are transformed to the disk-like shapes and the size range has decreased to 15-20 nm. Figure 2-7 demonstrates that if a triangular prism with an edge length of 35 nm is etched into a disk-like plate, the resulting particle should have a

diameter of approximately 20 nm, which is in agreement of the observed particle size. The relative diameters of the triangle and disk are drawn to scale.

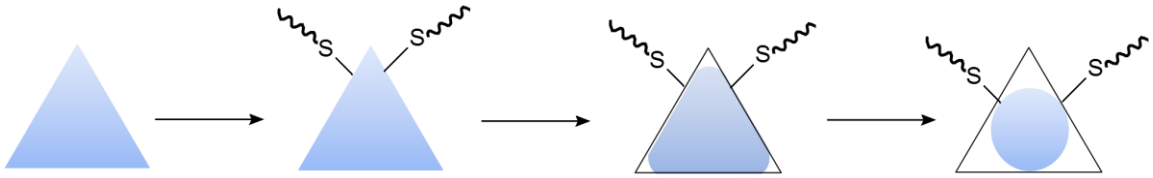

Figure 2-2 - Illustration of the evolution in Ag nanoprism morphology

There is also an increased number of small particles ~5 nm in diameter in the solution, and the number of large particles decreases considerably. This is reflected in how the peak width of the Ag nanoprism plasmon band at 20 hours is narrower than at 2 hours indicating a narrowing of particle size distribution. As shown in figure 2-5(c) after reaction with of 1mM PEG-SH for 2 hours, the Ag nanoprisms still display a broad size distribution. The particles with diameters over 25 nm are still roughly triangular in shape with only slightly rounded tips. The particles that are smaller are more disk-like. After reaction for 20 hours, shown in figure 2-5(d), only disk like particles remain, along with very small particles with diameters less than 2 nm. The overall decrease in LSPR intensity over the course of the reaction is proportional to particle size.

To further examine the role of PEG-SH in changing the Ag nanoprism morphology, UV-Vis spectroscopy was performed using PEG-SH of different molecular weights and concentrations. Figure 2-8 shows the in situ UV-Vis results of Ag nanoprism PEG-ylation using 1, 2, 5, and 10 kDa PEG-SH arranged as a function of both PEG-SH concentration and molecular weight.

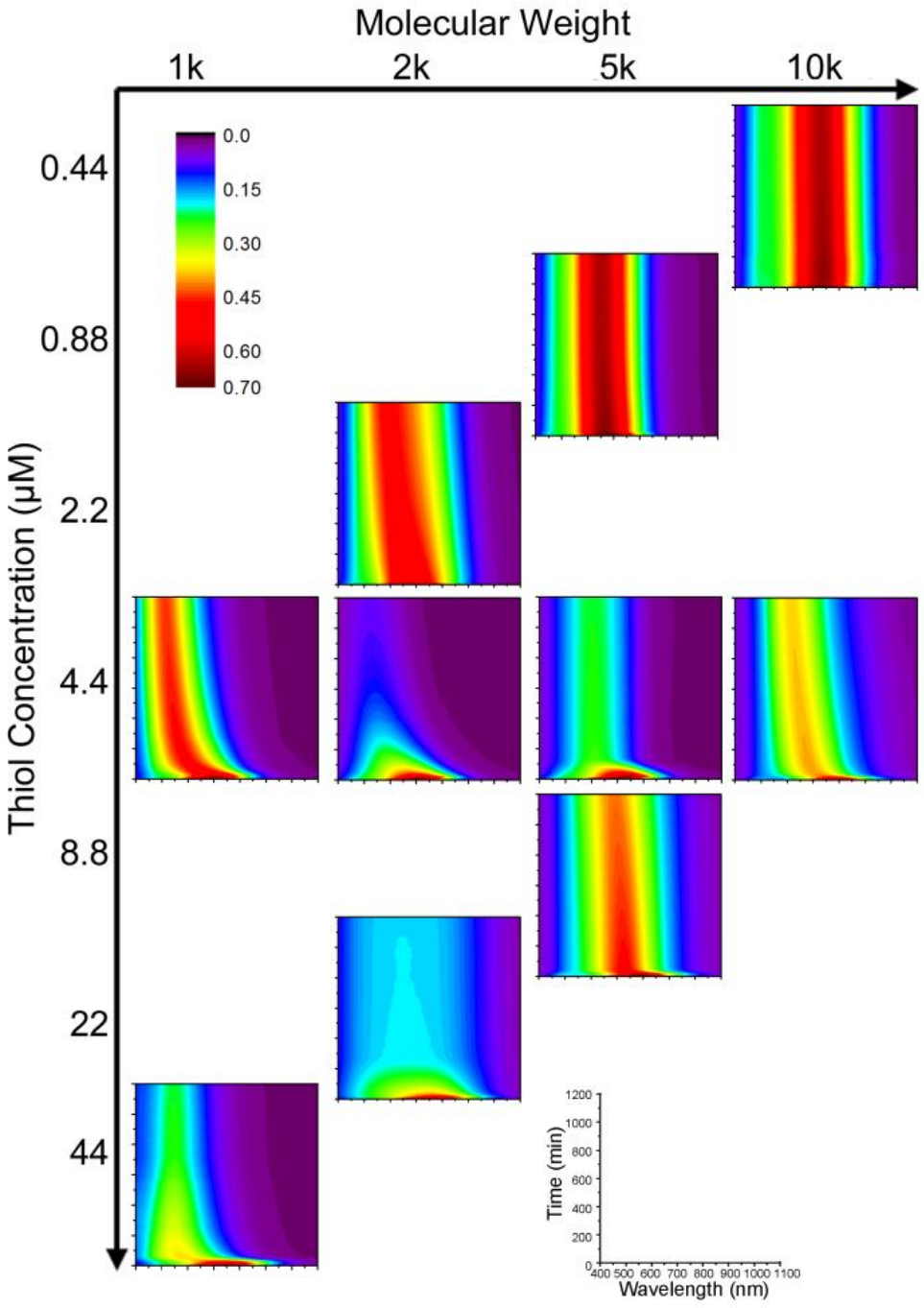

Figure 2-3 - UV-Vis spectra of Ag nanoprisms during PEG-ylation with PEG-SHs of different concentrations and molecular weights

Since solutions of constant polymer concentration but variable molecular weight will have varying concentrations of –SH end groups, a series of reactions were carried out at both

constant polymer concentration and constant –SH concentration. For example, the 0.1 mM, 1 kDa PEG-SH is 4.4 μM in –SH, while the 0.1 mM, 2 kDa PEG-SH contains 2.2 μM of –SH. Plots along the same diagonal line were carried out at the same polymer concentration, while plots along the same horizontal line indicate a constant –SH concentration. The x and y axes are shown in the bottom right corner of the figure.

At fixed molecular weight (vertical columns), increasing PEG-SH concentration generally results in a faster tip-rounding process, as shown by a more rapid blue-shift of the LSPR band. For a fixed polymer concentration (diagonal direction), PEG-SH of higher molecular weight have weaker morphology changing effects on the particles, and appear to do better at preserving the original particle shape. The LSPR band remains mostly constant when the Ag nanoprisms are reacted with 0.1 mM (0.44 μM by –SH) PEG-SH of 10 kDa. For constant –SH concentrations (horizontal direction), the higher molecular weight polymers, better protect the Ag nanoprism shape. This is however not always the case. For example, PEG-ylation using 2 kDa instead of 1 kDa PEG-SH leads to an almost complete quench of the nanoprism LSPR band. As a result, both the PEG unit and –SH unit functions need to be considered in the PEG-ylation process of the nanoprisms. The UV-Vis spectra and TEM images clearly reveal not only a gradual change in particle shape from triangular to disk-like, but also an overall decrease in the particle size and LSPR band intensity.

To better understand the reason for these spectral and morphological changes identified by the UV-Vis and TEM data, reaction by-products must also be identified. In order to determine the chemical speciation of both Ag and S over the course of the PEG-ylation reaction, solution-phase XANES experiments were carried out. The reaction between the Ag nanoprisms and PEG-

SH of 1 kDa and 10 kDa, respectively, both at a concentration ratio of [Ag]:[polymer] = 1:10, were chosen as representative systems.

In order to obtain spectra with a good signal-to-noise ratio, the Ag nanoprism solutions were concentrated by centrifugation to achieve a molar concentration on the order of 5 mM Ag. The concentrated Ag nanoprism solution and a PEG-SH solution of 50 mM were mixed in a 1:1 volume ratio. For ex situ measurements, spectra were taken 20 hours after the beginning of the reaction. For in situ measurements, Ag nanoprisms and 1 kDa PEG-SH were mixed and sealed in the sample cell, and the reaction was conducted under magnetic stirring throughout the measurement.

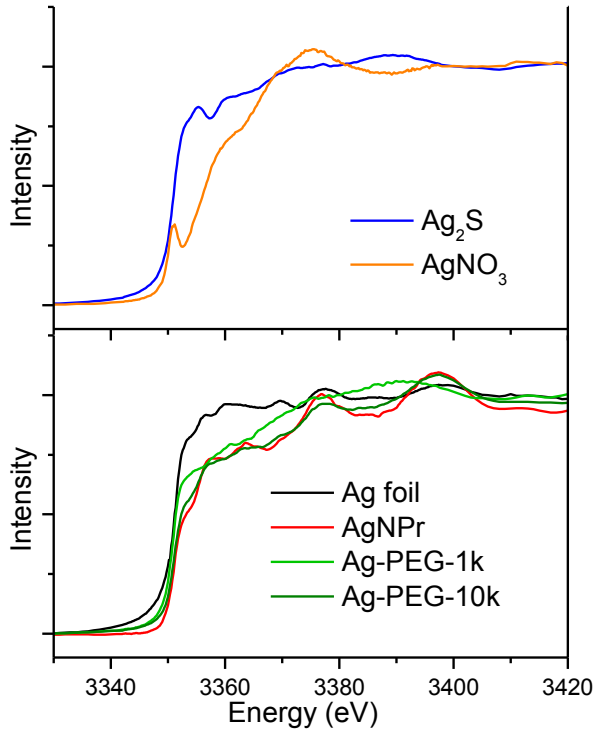

Figure 2-4 - Ag L_3-edge XANES of Ag nanoprisms before and after PEG-ylation compared to Ag references

The Ag L_3-edge XANES of the Ag nanoprisms before and after PEG-ylation are shown in figure 2-9. These spectra are compared to select Ag reference samples. The citrate-protected Ag nanoprisms exhibit features that are similar to bulk Ag foil. The broad post-edge features and higher white-line intensity in the Ag foil are likely due to fluorescence signal saturation, but may also be caused by a surface oxide layer. Regardless of the difference in the spectra, the well-defined profile and the absence of a sharp edge peak in Ag nanoprisms spectrum suggests that the nanoprisms are in the Ag^0 oxidation state. After PEG-ylation with 10kDa PEG-SH, the overall profile of the spectrum remains very similar, with only a very slight increase in white-line intensity. This suggests that the PEG-ylated nanoprisms remain metallic with only a slight oxidation on the surface. The intensity of the white-line is more prominent when the reaction is done with the 1 kDa PEG-SH, as well as a loss of fine structure in the post edge features. This larger increase suggests that more of the Ag is oxidized, but the sharp peak in the spectrum that is seen for $AgNO_3$ or Ag_2S is not present, suggesting that the degree of this oxidation is still low. This oxidation could be from the formation of silver thiolates[26], which may form as a result of an oxidative addition of thiol to the silver surface.

The broadening to the post edge peak may be from a decrease in the crystallinity of the Ag nanoprisms. These post edge oscillations originate from multiple scattering form neighbouring atoms and when the Ag becomes more disordered, such fine spectral features get broadened.[27] This could be due to the formation of small Ag clusters that have Ag atoms lacking long-range order. This hypothesis is consistent with the observation of very small nanoparticles in the TEM images. It is clear from this data that the material that is being lost from the tips of the nanoprisms, but continues to be Ag^0 in the form of small clusters in the solution. Because the clusters are so small, they will not have a visible plasmon band in UV-Vis measurements.[28]

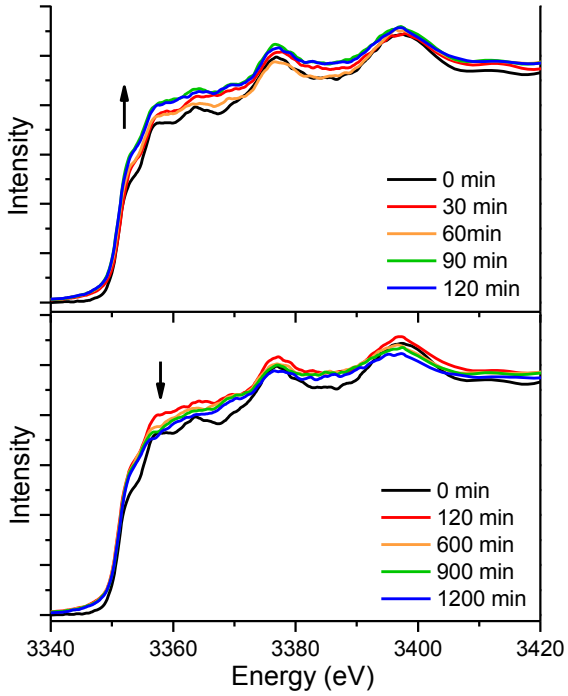

Figure 2-5 - Ag L_3-edge XANES of in situ reaction of 1 kDa PEG-SH with Ag nanoprisms

Figure 2-10 shows the Ag L_3-edge XANES of the Ag nanoprisms reacting with the 1 kDa PEG-SH over 20 hours. It shows that the oxidation of the Ag nanoprisms is foremost within the first 2 hours, as indicated by the slow increase in the intensity of the white line. After the first 2 hours the intensity of the white line stays constant, but the broadening and the loss of intensity in the post edge peaks indicated a loss of crystallinity of Ag, or the presence of dissolve Ag in the reaction solution.

The PEG-ylation process was also explored from the S point of view. Figure 2-11 shows the S K-edge XANES of the PEG-SH solution before and after reaction with the Ag nanoprisms, and is compared to selected S-containing compounds for reference.

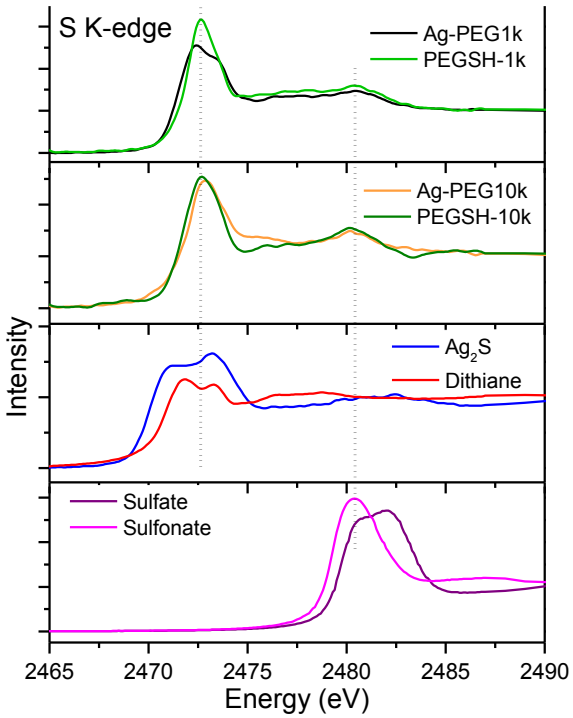

Figure 2-6 - S K-edge XANES of PEG-SH before and after reaction with Ag Nanoprisms

The PEG-SH spectra show an intense peak that is centered at 2472.7 eV, and a weak shoulder-like feature on the higher energy side. These peaks originate from S 1s→σ* (S−H) and S 1s→σ* (S−C) electronic transitions, respectively.[22,29,30] In the 1 kDa PEG-SH sample, it is seen that after reaction with the Ag nanoprisms, there is clear evidence of disulfide formation as indicated by the doublet at 2472.4 eV and 2473.4 eV. Comparable features are present in the dithiane reference compound. These two peaks in the S K-edge spectrum are from the S 1s→σ* (S−S) and S 1s→σ* (S−C) transitions, respectively.[29,31] Conversely, there is no significant change in the 10 kDa PEG-SH after reaction with the Ag nanoprisms. A minor peak shift is an indication of the disappearance of the S–H bond, which usually appear at the lower energy side, leaving only the peak due to the S–C bond.[22,32] The very small pre-edge feature at 2470 eV is indication of the Ag–S bond.[33] In the 1 kDa PEG-SH functionalized Ag nanoprisms this feature

is absent. Based on results from TEM, UV-Vis, and Ag L_3-edge XANES, the form of Ag after functionalization with 1 kDa PEG-SH is PEG-ylated Ag nanoparticles of significantly reduced size. This agrees with the absence of the pre-edge feature, as it has been reported that the intensity of this pre-edge feature decreases as the metal nanoparticle size decreases.[34]

In both the 1 kDa and 10 kDa PEG-SH and PEG-ylated Ag nanoprism samples, it is important to note that there is a broad peak at 2481 eV, which corresponds to S of higher oxidation state. Upon comparison with reference compounds it is concluded that this peak is due to the presence of sulfonates. Because the intensity of this peak shows no significant variation before and after the reaction with the Ag nanoprisms, it suggests that the product of PEG-SH oxidation is almost exclusively the disulfide, and any pre-existing sulfonate impurities have little to no effect on the PEG-ylation process.

It can be seen from the XANES data that the shape transformation that occurs when the Ag nanoprisms are reacted with 1 kDa PEG-SH is correlated with the oxidation of the thiol to the disulfide. In order to investigate the effect of O_2, a UV-Vis kinetic study was carried out in an anaerobic environment. Ag nanoprisms and PEG-SH solutions (1 kDa, 1 mM) were degassed and then combined under a N_2 atmosphere using standard Schlenk techniques, the reaction mixture was then sealed in a cuvette that had been fitted with a vacuum valve.

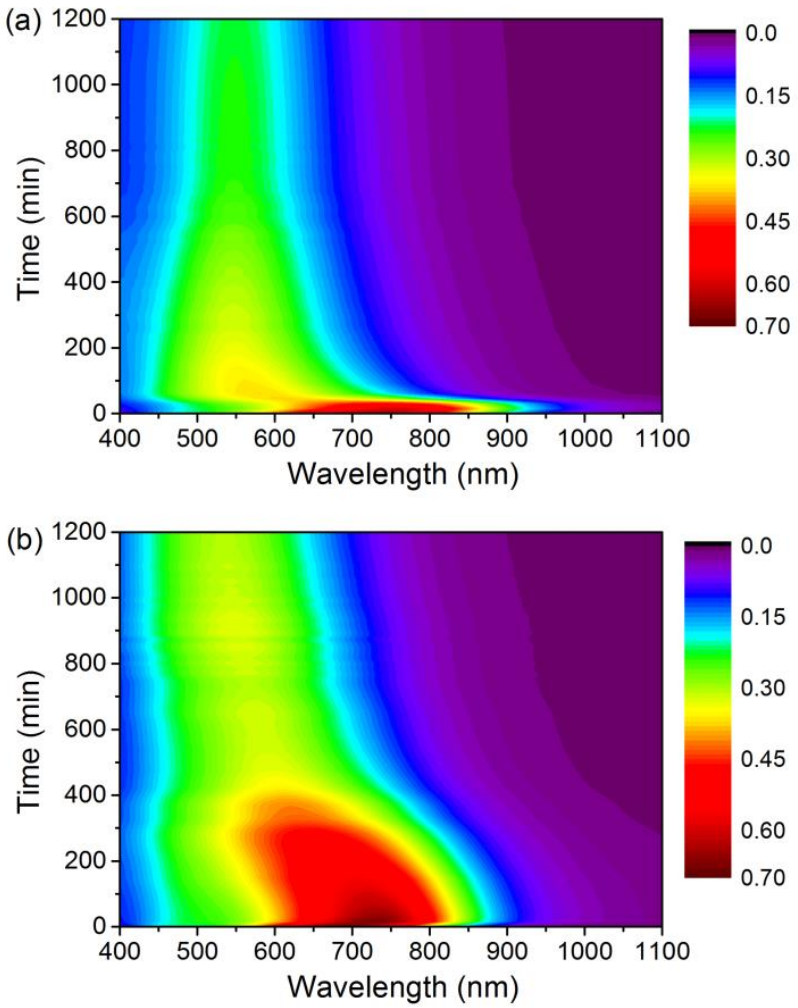

Figure 2-7 – UV-Vis over time of PEG-ylation reaction in both (a) O_2 and (b) N_2

Figure 2-12 shows a comparison the UV-Vis spectra of the Ag nanoprisms during the PEG-ylation reaction. Figure 2-12(a) shows the reaction in an ambient O_2 environment and figure 2-12(b) shows the reaction under an N_2 atmosphere. In the nitrogen atmosphere, the LSPR band still displays a blue-shift over time. However, the rate of the blue-shift is reduced by almost an order of magnitude. In case of the reaction conducted in ambient air, the LSPR band blue-shifts by approximately 140 nm within the first 45 min. In the N_2 environment, it takes nearly 460 min to achieve the same magnitude of shift. This demonstrates that O_2 must play an

important role in the rounding of the Ag nanoprism tips in the presence of PEG-SH. Conversely, the blue-shift that occurs even in the absence of O_2 also indicates that there must be another reaction pathway, although a much slower one, that still can transform the shape of the Ag nanoprisms.

From these UV-Vis kinetic studies, it is found that the thiol concentration is one of the key factors in determining the degree of Ag nanoprism tip-rounding; the molecular weight of the PEG-SH affects the final shape of the Ag nanoprisms; and the shape transformation process of the Ag nanoprisms can be accelerated by O_2. Based on all these results, the reaction mechanism shown in figure 2-11 is proposed for the PEG-ylation of Ag nanoprisms.

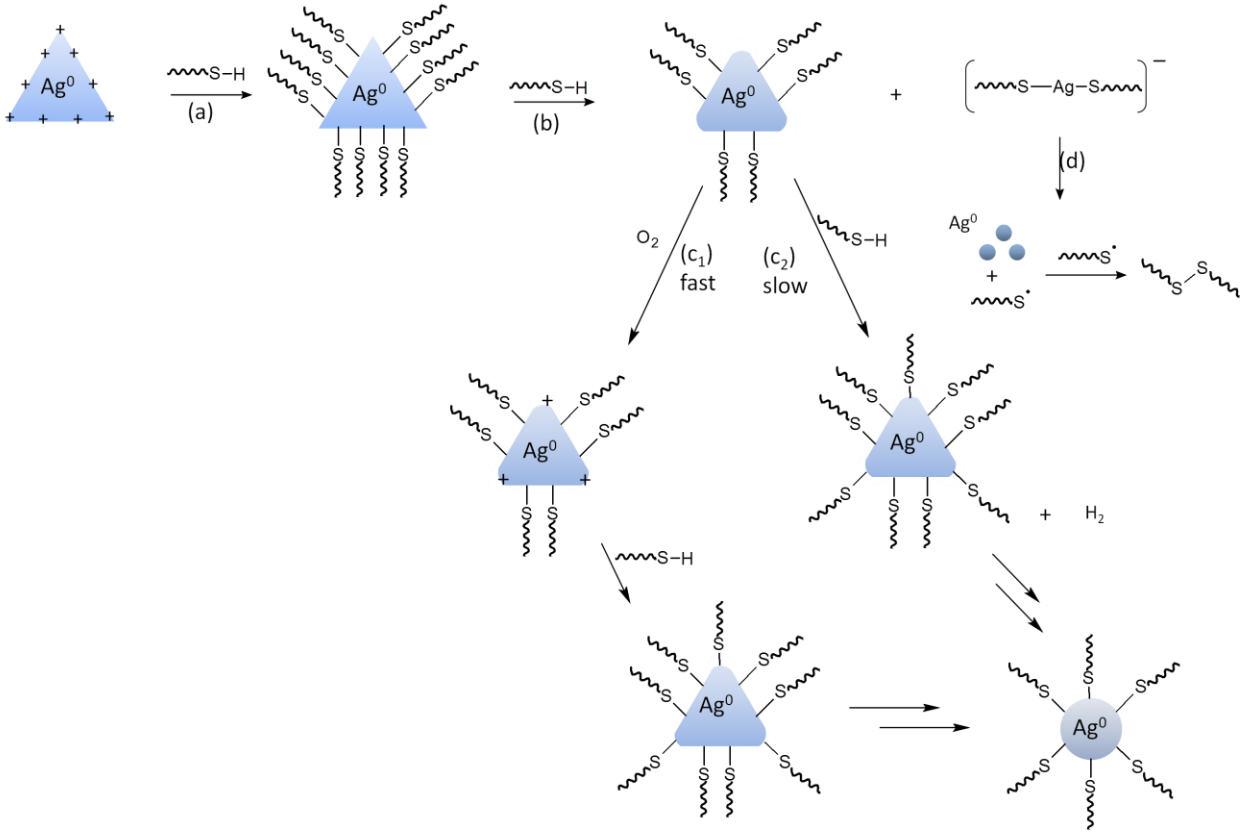

Figure 2-8 - Proposed reaction mechanism for Ag nanoprism PEG-ylation

The prepared Ag nanoprisms are electrostatically stabilized by citrate ions that are adsorbed to the surface of the particle. Reports in the literature suggest that the surface of the Ag nanoprisms likely consist of a monolayer of Ag^+.[35,36] The pH of the aqueous citrate reaction solution is ~ 9 – 10 ensuring that a considerable portion of the PEG-SH exists as the thiolate anion. Step (a) in figure 2-13, the reaction between the Ag+ atoms on the surface of the particle and the thiolate, is expected to be very rapid. This produces the PEG-ylated, triangular Ag nanoprisms, evidence for which can be found in the initial red-shift of the LSPR band.

The tips of the nanoprisms are where the planes of the prism meet at a vertex. The growth of the particles produces a {111} basal plane and {110} plane along the short axis.[37,38] The tips therefore have a very high surface energy and the low stability due to a lack of neighboring atoms. These tips are consequently susceptible to attack by thiolates, forming a silver thiolate complex which can dissociate from the surface as illustrated in step (b) of figure 2-13, exposing the nanoparticle underneath to the solution. If O_2 is present, the bare metal surface is easily oxidized, as shown in step (c1), and can then react further with excess PEG-SH. This will continue until all of the surface energy is evenly distributed and the particle is a disk-like shape. The etching process then slows and becomes more isotropic in nature. If no O_2 is present, the oxidation of the particle surface is much slower and may be accompanied by the generation of H_2 as shown in step (c2).[39] The generation of H_2 is kinetically unfavourable, so this accounts for the decrease of the reaction rate in the absence of oxygen, and also provides a plausible mechanism for the shape transformation that is observed under anaerobic conditions.

Due to the lack of any Ag(I) observed in the XANES measurements, the silver thiolate complex must not persist in solution. Reduction of Ag^+ to Ag^0 with the associated oxidation of the thiolate to a sulfur radical[40] would explain why no edge peak is seen in the Ag L_3-edge

spectra. The recombination of the sulfur radicals would lead to disulfide which is seen clearly in the S K-edge spectra, as shown in step (d) of figure 2-13.

When no O_2 is present, the oxidation of the silver particle surface appears to be the rate limiting step. However, under ambient conditions, this process is expected to be fast. Factors such as polymer molecular weight and concentration therefore control the rate and degree of the reaction.

When the concentration of the PEG-SH is low, the rate of formation of free silver thiolate shown in step (b) is repressed. This may be an explanation for the relative stability of the Ag nanoprisms at lower polymer concentrations (0.1 mM). However, because the thiol concentration is so low, the thiol becomes the limiting reagent. Therefore, once all of the thiol is converted to disulfide the reaction stops. This provides an explanation for the reduced rate and limited shape transformation for low PEG-SH concentrations regardless of molecular weight.

When the –SH concentrations are fixed, the 2 and 5 kDa polymers seem to do the worst at passivating the surface of the Ag nanoprisms (Figure 2-8). At 1 kDa molecular weight, the PEG chains can self-organize and form a densely packed layer on the surface of the particle which can prevent further attack by the thiolates and the liberation of the silver thiolate complex as illustrated in figure 2-14.

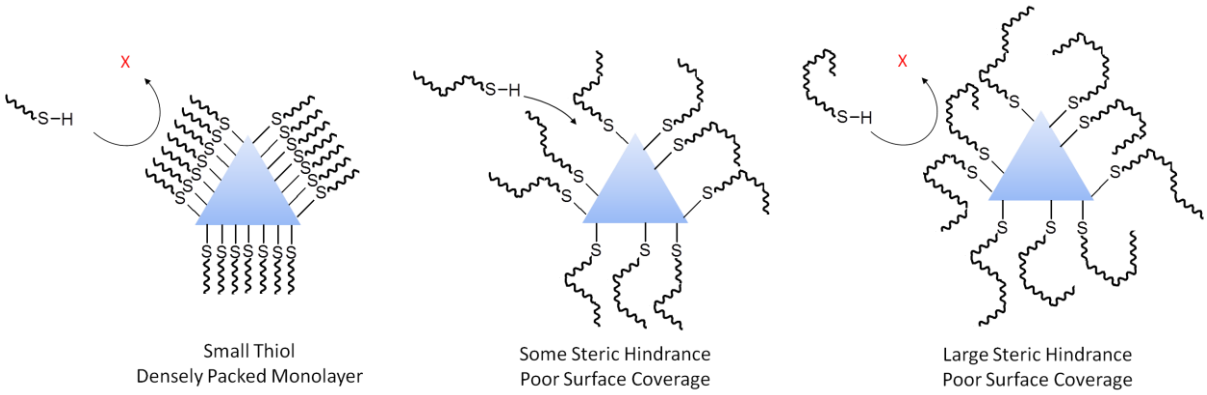

Figure 2-9 - Monolayer formation on Ag nanoprisms using thiols of different molecular weights

This also explains how small molecule thiols such as MHA are successful at passivating the Ag nanoprisms surface. An increase in the chain length of the polymer leads to a more sporadic coverage of the Ag nanoprisms due to steric constraints, which leads to a more porous passivating layer and a faster etching. This is why the 2 and 5 kDa lead to faster rounding of the particles compared to the 1 kDa polymer. On the other hand, increasing the molecular weight of the polymer will increase the steric bulk and prevent the PEG-SH from closely approaching the surface of the Ag nanoprism and prevent the release of the frees silver thiolate into solution. As a result, the 10 kDa molecular weight PEG-SH is the most effective at preserving the particles original triangular shape.

Conclusions

Developing methods to increase the stability of the Ag nanoprisms and to preserve their sharp tips will be essential to maximize near-field effects in various plasmonic applications. The proposed mechanism for the shape transformation of Ag nanoprisms takes into consideration factors such as PEG-SH molecular weight and concentration, as well as the O_2 in the ambient environment. Any excess PEG-SH in the reaction solution will react with silver ions at the high

surface energy tips of the nanoprism, resulting in the formation of silver thiolate complexes and the rounding of the nanoprism tips. An important part of the tip rounding process includes O_2 accelerating the tip-rounding process by continuously oxidizing the silver surface. The Ag thiolate complex then undergoes a spontaneous redox reaction, resulting in the formation of small Ag clusters and the PEG disulfide. These results demonstrate that it is low concentrations of high molecular weight PEG-SH that are critical for the stability of the nanoprisms.

References

(1) Atwater, H. A.; Polman, A. Nat Mater 2010, 9, 205.

(2) Skrabalak, S. E.; Au, L.; Li, X.; Xia, Y. Nat. Protocols 2007, 2, 2182.

(3) Aherne, D.; Ledwith, D. M.; Gara, M.; Kelly, J. M. Advanced Functional Materials 2008, 18, 2005.

(4) Zhang, Q.; Li, N.; Goebl, J.; Lu, Z.; Yin, Y. Journal of the American Chemical Society 2011, 133, 18931.

(5) Kulkarni, A. P.; Munechika, K.; Noone, K. M.; Smith, J. M.; Ginger, D. S. Langmuir 2009, 25, 7932.

(6) Choi, H.; Lee, J.-P.; Ko, S.-J.; Jung, J.-W.; Park, H.; Yoo, S.; Park, O.; Jeong, J.-R.; Park, S.; Kim, J. Y. Nano Letters 2013, 13, 2204.

(7) Lee, B.-H.; Hsu, M.-S.; Hsu, Y.-C.; Lo, C.-W.; Huang, C.-L. The Journal of Physical Chemistry C 2010, 114, 6222.

(8) Liu, L.; Kelly, T. L. Langmuir 2013, 29, 7052.

(9) Otsuka, H.; Nagasaki, Y.; Kataoka, K. Advanced Drug Delivery Reviews 2012, 64, Supplement, 246.

(10) Love, J. C.; Estroff, L. A.; Kriebel, J. K.; Nuzzo, R. G.; Whitesides, G. M. Chemical Reviews 2005, 105, 1103.

(11) Li, X.; Choy, W. C. H.; Lu, H.; Sha, W. E. I.; Ho, A. H. P. Advanced Functional Materials 2013, 23, 2728.

(12) Chen, H.-C.; Chou, S.-W.; Tseng, W.-H.; Chen, I. W. P.; Liu, C.-C.; Liu, C.; Liu, C.-L.; Chen, C.-h.; Wu, C.-I.; Chou, P.-T. Advanced Functional Materials 2012, 22, 3975.

(13) Heo, M.; Cho, H.; Jung, J.-W.; Jeong, J.-R.; Park, S.; Kim, J. Y. Advanced Materials 2011, 23, 5689.

(14) Wang, D. H.; Kim, D. Y.; Choi, K. W.; Seo, J. H.; Im, S. H.; Park, J. H.; Park, O. O.; Heeger, A. J. Angewandte Chemie International Edition 2011, 50, 5519.

(15) An, J.; Tang, B.; Zheng, X.; Zhou, J.; Dong, F.; Xu, S.; Wang, Y.; Zhao, B.; Xu, W. The Journal of Physical Chemistry C 2008, 112, 15176.

(16) Tang, B.; Xu, S.; An, J.; Zhao, B.; Xu, W.; Lombardi, J. R. Physical Chemistry Chemical Physics 2009, 11, 10286.

(17) Sham, T. K. Physical Review B 1985, 31, 1888.

(18) Bzowski, A.; Sham, T. K. Physical Review B 1994, 49, 13776.

(19) Miyamoto, T.; Niimi, H.; Kitajima, Y.; Naito, T.; Asakura, K. Journal of Physical Chemistry A 2010, 114, 4093.

(20) George, G. N.; Gnida, M.; Bazylinski, D. A.; Prince, R. C.; Pickering, I. J. Journal of Bacteriology 2008, 190, 6376.

(21) Fleet, M. E. The Canadian Mineralogist 2005, 43, 1811.

(22) Beyhan, S.; Hu, Y.; Urquhart, S. G. The Journal of Chemical Physics 2011, 134, 244304.

(23) Hu, Y. F.; Coulthard, I.; Chevrier, D.; Wright, G.; Igarashi, R.; Sitnikov, A.; Yates, B. W.; Hallin, E. L.; Sham, T. K.; Reininger, R. AIP Conference Proceedings 2010, 1234, 343.

(24) Kelly, K. L.; Coronado, E.; Zhao, L. L.; Schatz, G. C. The Journal of Physical Chemistry B 2002, 107, 668.

(25) Hutter, E.; Fendler, J. H. Advanced Materials 2004, 16, 1685.

(26) Gondikas, A. P.; Morris, A.; Reinsch, B. C.; Marinakos, S. M.; Lowry, G. V.; Hsu-Kim, H. Environmental Science and Technology 2012, 46, 7037.

(27) Konigsberger, D. C.; Prins, R. X-Ray Absorption - Principals, Applications, Techniques of EXAFS, SEXAFS, and XANES Wiley - Interscience, 1988.

(28) Peng, S.; McMahon, J. M.; Schatz, G. C.; Gray, S. K.; Sun, Y. Proceedings of the National Academy of Sciences 2010, 107, 14530.

(29) Pickering, I. J.; Prince, R. C.; Divers, T.; George, G. N. FEBS Letters 1998, 441, 11.

(30) Hitchcock, A. P.; Bodeur, S.; Tronc, M. Physica B: Condensed Matter 1989, 158, 257.

(31) Chauvistre, R.; Hormes, J.; Hartmann, E.; Etzenbach, N.; Hosch, R.; Hahn, J. J. Chem. Phys. 1997, 293.

(32) Padmos, J. D.; Zhang, P. The Journal of Physical Chemistry C 2012, 116, 23094.

(33) Chaudhuri, A.; Odelius, M.; Jones, R. G.; Lee, T. L.; Detlefs, B.; Woodruf, D. P. J. Chem. Phys. 2009.

(34) MacDonald, M. A.; Zhang, P. J. J. Phys. Chem. Letters 2010, 1821.

(35) Liu, J.; Hurt, R. H. Environmental Science and Technology 2010, 2169.

(36) Zhang, W.; Yao, Y.; Sullivan, N.; Chen, Y. Environmental Science and Technology 2011, 422.

(37) Lofton, C.; Sigmund, W. Advanced Functional Materials 2005, 15, 1197.

(38) Elchiguerra, J. L.; Reyes-Gasga, J.; Yacaman, M. J. Journal of Materials Chemistry 2006, 16, 3906.

(39) Laibinis, P. E.; Whitesides, G. M.; Allara, D. L.; Tao, Y. T.; Parikh, A. N.; Nuzzo, R. G. Journal of the American Chemical Society 1991, 113, 7152.

(40) Singh, S.; Chaturvedi, J.; Bhattacharya, S.; Noth, H. Polyhedron 2011, 30, 93.

Chapter 3 – Incorporation of Nanoparticles into Bulk Heterojunction Solar Cells

Solar Cell Fabrication

There are many different types of solar cells, all with the same general function. Solar energy is captured by the device and converted into electrical energy. One of the branches of solar cell types is organic solar cells, or OPV. There are a number of types of organic solar cells, the main type being BHJ cells. The general structure of a BHJ is shown in figure 1-4.

In order to try and enhance the efficiency of these cells, this study looks at incorporating nanoparticles into the body of the cell. The main architecture of the cell in this study is what is illustrated in figure 1-4. The active layer is the heavily studied blend P3HT:PCBM. This active layer was chosen because of its extensive use in the literature. Hole transport layers were chosen based on how the Ag nanoparticles were incorporated.

The nanoparticles of different shapes, sizes and materials were integrated in to two places within the cell structure. The particles studied in this thesis include both 10 and 60 nm spherical silver and gold nanoparticles, as well as 25 nm triangular silver nanoparticles. Figure 3-1 shows the nanoparticles incorporated (a) on top of the anode, under the hole transport layer of the cell, and (b) into the active layer of the cell.

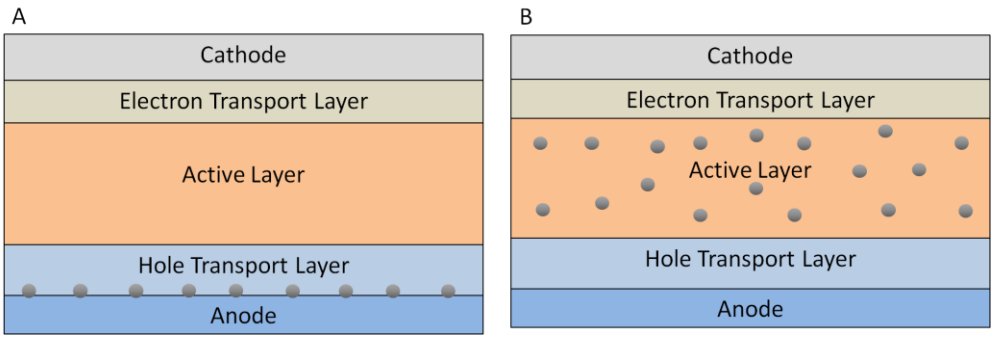

Figure 3-1 - Nanoparticles incorporated (a) under the hole transport layer and (b) into the active layer

The two different placements of nanoparticles within the cell were chosen to compare the effects of light reflection and plasmon enhancement. The nanoparticle under the hole transport layer will only contribute to light reflection within the cell. The nanoparticles that are incorporated into the active layer of the cell could cause enhancement from both the light reflection and plasmon enhancement.

All five types of nanoparticles were incorporated into the active layer of the solar cell to determine if they will contribute to efficiency enhancement. The silver triangular prisms were also incorporated under the hole transport layer to attempt to increase the efficiency of the cell. The different nanoparticle shapes were chosen to see if the sharp corners of the triangles were more beneficial. The different sizes of the particles were compared to see if there is any dependence of efficiency on particle size. The different materials were chosen to see if one material will perform better than the other.

Experimental

Silver Prism Synthesis 1

In this synthesis[1], silver prisms were synthesized by rapidly stirring 1 mL trisodium citrate (75 mM), 100 µL silver nitrate (50 mM), 200 µL poly(vinyl pyrrolidone) (17.5 mM), and

120 μL hydrogen peroxide (30% wt) in 48.08 mL H_2O. 500 μL sodium borohydride (100 mM) is quickly injected and the solution is allowed to stir for 2 hours. Once the reaction was completed, indicated by the solution turning dark blue, the solution was centrifuged at 13000 rpm for 2 hours. The supernatant was removed and the final volume was brought to 25 mL using 5 mM trisodium citrate.

Silver Prism Synthesis 2

Silver nanoprisms were synthesized according to literature procedures.[2] Trisodium citrate (5 mL, 2.5 mM), poly (sodium styrenesulphonate) (0.25 mL, 500 mg/L), and $NaBH_4$ (0.3 mL, 0.5 mM) are combined. While stirring, $AgNO_3$ (5 mL, 0.5 mM) was added drop wise at a rate of 120 mL/hour to create a seed solution. In separate vials, Millipore water (5 mL), L-ascorbic acid (75 μL, 10 mM), and varying amounts of seed solution are combined. To each vial, $AgNO_3$ (3 mL, 0.5 mM) was added drop wise at a rate of 60 mL/hour, followed by trisodium citrate (0.5 mL, 25 mM). The resulting particle solutions were centrifuged at 13000 rpm for 2 hours. The supernatant was removed and the remaining nanoparticle solution was brought back to original volume with 5 mM trisodium citrate.

Nanoparticle PEG-ylation

The particles to be PEG-ylated are synthesized 25 nm Ag prisms from synthesis 1, purchased 10 nm Ag particles (Sigma Aldrich), purchased 60 nm Ag particles (Sigma Aldrich), purchased 10 nm Au particles (Sigma Aldrich), and purchased 60 nm Au particles (Sigma Aldrich). The particles from Sigma Aldrich were stabilized in sodium citrate and used as received. One part PEG-thiol solution (0.3 mM) in trisodium citrate was added to 2 parts nanoparticle solution. The solution was stirred vigorously for 15 minutes and then centrifuged at 13000 rpm for 2 hours. The supernatant is removed and the remaining PEG particle solution is

dispersed in a small amount of 5 mM citrate. The PEG particle solution is added to equal parts $CHCl_3$ and stirred vigorously to encourage phase transfer. The 5 mM trisodium citrate layer was removed leaving the PEG particles dispersed in $CHCl_3$. If the particles are to be used in the glove box, the solvent is removed via rotary evaporation. The dried particles are transferred into the glove box and redispersed in dry solvent, where they can be incorporated into the active layer mixture for cell fabrication. Particles are diluted in $CHCl_3$ to make solutions with optical densities of 2.00, 1.00, 0.50, 0.20, 0.10, and 0.50. These solutions are combined in a 1:1 ratio with P3HT:PCBM solution that is 2x the desired concentration. The final solutions are 2 %wt P3HT:PCBM in $CHCl_3$ containing particles with optical densities of 1.00, 0.50, 0.25, 0.10, 0.05, and 0.025.

Characterization

UV-Vis measurements were performed using a Cary 6000 UV-Vis spectrometer. Film thickness measurements were performed using a KLA Tencor profilometer.

Substrate Preparation

The ITO substrate is commercially available as a polished float glass, 25x25x0.7 mm, that is a SiO_2 passivated/ITO coated on one surface with series resistance of 4-8 Ω. Glass and ITO substrates are sonicated in 5% detergent solution for 15 minutes. The slides are then sonicated in milli-Q H_2O for 15 minutes, in isopropanol for 15 minutes, and ethanol for 15 minutes. The slides are allowed to air dry, then cleaned in a UV-Ozone cleaner for 15 minutes immediately before use.

3-Aminopropyltriethoxysilane Functionalization

Deposition of 3-aminopropyltriethoxysilane (APTES) on to cleaned glass substrates was done in a small plastic dessicator with a small open vial of APTES under static vacuum. The dessicator was allowed to come up to room pressure over 3 days. After removal from the dessicator, the substrates are dip rinsed in toluene to remove any excess or non-bonded APTES from the surface. To determine if an annealing step is necessary, some of the substrates are annealed on a hot plate at 70 °C for 15 minutes.

Nanoparticle Deposition

Nanoparticles that are incorporated on to the APTES layer are synthesized nanoprisms from both syntheses. The APTES functionalized substrates are allowed to soak in the as synthesized nanoparticle solution for 24 hours. The excess particle solution is removed; the substrates are rinsed in milli-Q water, and dried with N_2 flow. To avoid particle oxidation the substrates are stored for transfer in petri dishes backfilled with N_2 and then promptly transferred to the glove box.

Active Layer Preparation

The active layer is a 2% wt P3HT:PCBM blend in chloroform, ortho-dichlorobenzene (oDCB), or 1:1 $CHCl_3$:oDCB. P3HT was purchased from Rieke Metals Inc. and used as received. PCBM was purchased from Nano C and used as received. For this study a 1:0.8 ratio of P3HT:PCBM was chosen. It is extremely important to ensure that the ratio of P3HT:PCBM is always consistent.[3] For calibration studies the spin coating is done in air, but for cell fabrication the spin coating is done in a N_2 atmosphere to avoid any degradation that may occur from exposure to O_2 or moisture. Once coated the substrates are set aside for solvent evaporation before further use.

Hole Transport Layers

PEDOT:PSS blend was purchased from Baytron and used as received. PEDOT:PSS was deposited on to clean substrates for spin coating through a 45 μm syringe filter. After spin coating the substrates are annealed at 150 °C for 1 – 2 minutes. When spin coating for device fabrication the substrate was spun for 10 seconds at 200 rpm to allow for even coating of the substrate, then 5000 rpm for 40 seconds to form a 30 nm thick film. Once annealed, the films are transferred in to the N_2 environment within 5 minutes to avoid degradation from moisture and O_2.

MoO_3 was purchased as powder then pressed in to small pellets for use in the thermal evaporator. The MoO_3 was thermally evaporated at high vacuum and low pressure, approximately $1x10^{-6}$ mbar, to obtain a 3 nm thick film.

Electron Transport and Cathode Layers

The electron transport layer and cathode was deposited by thermal evaporation of LiF and Al. The LiF is used as purchased and a 0.8nm thick layer is thermally evaporated. The 100nm thick Al cathode is also thermally evaporated within the same evaporation cycle. The now completed solar cell is annealed at 150°C for 20 minutes and allowed to cool before testing.

Cell Testing

JV curve and cell parameter testing is done as soon as possible after fabrication. Testing is down in the N_2 environment using a Oriel Sol3A class AAA solar simulator with 100 $mWcm^{-2}$ AM1.5 output along with Newport calibrated 2x2 cm silicon reference cell. EQE testing is done in air using an EQ/IPCE measurement kit from Newport Oriel.

Results and Discussion

Layer Optimization of P3HT:PCBM

Before any nanoparticles can be incorporated into the solar cell, the deposition conditions for spin coating the active layer must be optimized. The goal thickness for the active layer is 100 nm. This thickness is thick enough to capture photons, but thin enough to encourage charge transfer[4-7]. Three different solvent systems were investigated. Chloroform, o-dichlorobenzene and a 1:1 combination of $CHCl_3$ and oDCB were chosen. The calibration curve for the P3HT:PCBM in $CHCl_3$ is shown in figure 3-2.

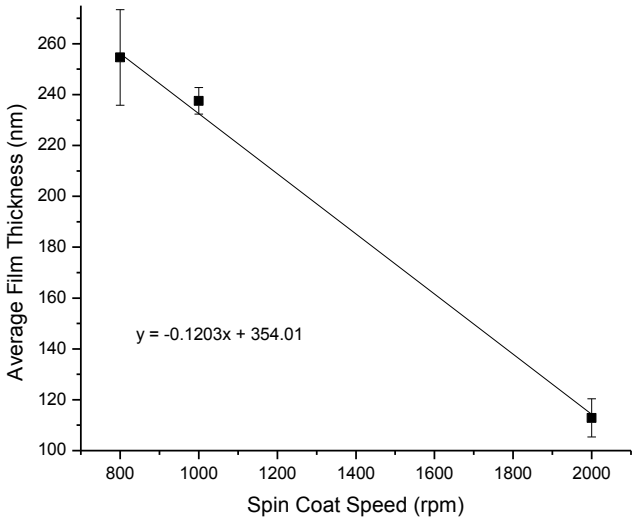

Figure 3-2 - P3HT:PCBM in $CHCl_3$ spin coating calibration curve

The data presented in figure 3-2 are average values and the error bars represent variation in the film thickness. Figure 3-2 shows that in order to get a film that is 100 nm thick, the optimal spin speed for spin coating P3HT:PCBM on to glass substrates from $CHCl_3$ is approximately 2000 rpm. The calibration curve for P3HT:PCBM in oDCB is shown in figure 3-3.

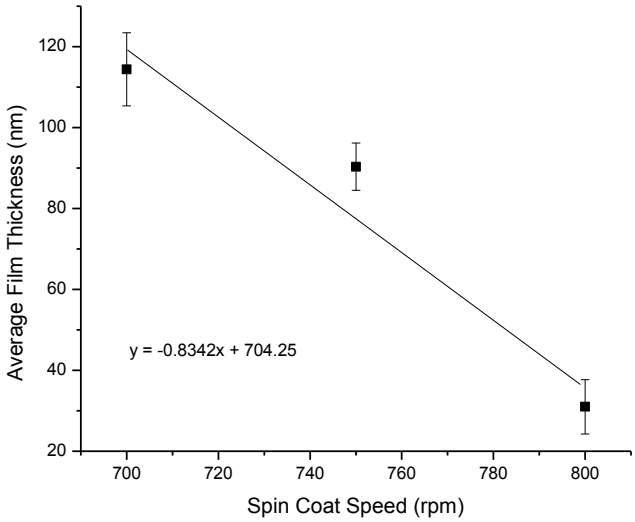

Figure 3-3 - P3HT:PCBM in oDCB spin coating calibration curve

The data presented in figure 3-3 are average values and the error bars represent variation in the film thickness. Figure 3-3 shows that in order to obtain a 100 nm thick film, the optimal speed for spin coating P3HT:PCBM on to a glass substrate from oDCB is approximately 725 rpm. The calibration curve for P3HT:PCBM in 1:1 $CHCl_3$:oDCB is shown in figure 3-4.

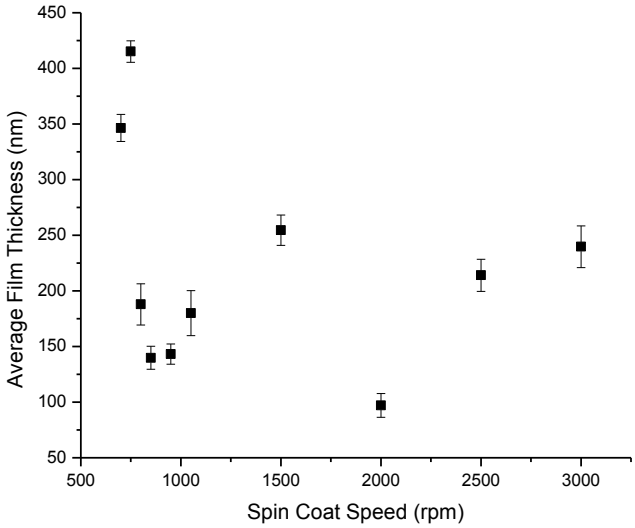

Figure 3-4 – P3HT:PCBM in $CHCl_3$:oDCB spin coating calibration curve

The data presented in figure 3-4 are average values and the error bars represent variation in the film thickness. Figure 3-4 shows that the spin coating of P3HT:PCBM on to glass from 1:1 $CHCl_3$:oDCB was unsuccessful. There was not a linear relationship between the spin coating speeds and the film thickness, so an average speed to create a 100 nm thick film was not found. As well the films were often non-uniform in thickness or did not completely coat the substrate.

Nanoparticle Synthesis 1

Triangular silver nanoparticles were synthesized according to literature procedures.[1] From the TEM images as shown in figure 2-1 it is apparent that the reaction did successfully create triangular shaped particles, with a narrow size distribution. The average prism size shown in figure 2-2, calculated from the TEM images, is 25 ± 9 nm. The UV-Vis spectrum for these particles is shown in figure 2-3, and the peak assignments were discussed previously on page 39.

Nanoparticle Synthesis 2

The particles were synthesized according to literature procedures.[2] The UV-Vis spectra for the second synthesis are shown in figure 3-5. This synthesis is much more size tunable than the other synthesis.

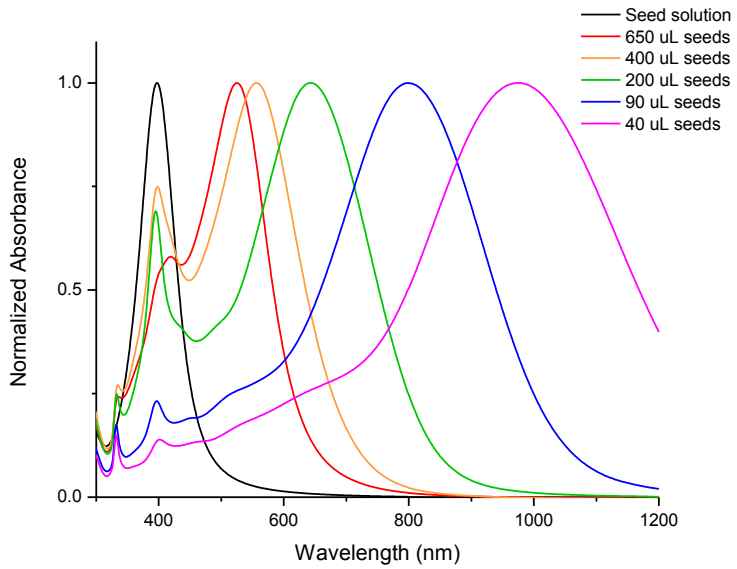

Figure 3-5 - UV-Vis spectra of varying sizes of Ag nanoprisms from synthesis 2

By varying the amount of seed solution but not changing the amount of additional $AgNO_3$ added, the resulting sizes of particles will vary. If less seed solution is introduced the particles will be larger, because there is more $AgNO_3$ available to each seed particle to create larger prism particles. This is seen as a red shift in the plasmon band of the nanoparticles. If there are more seeds, the prism particles will be smaller, because there is less $AgNO_3$ available per seed to create the prisms. The shape characteristics of the spectra in figure 3-5 are the same as the spectra from synthesis 1 (figure 2-3), indicating that the shape of the nanoparticles is also triangular.

PEG-ylation of Nanoparticles

Synthesized nanoprisms and purchased nanoparticles are functionalized with PEG-SH in order to become soluble in organic solvents. While the particles phase transfer successfully into $CHCl_3$ and 1:1 $CHCl_3$:oDCB, they did not transfer into oDCB alone. The particles studied include; synthesized 25 nm Ag prisms, purchased 10 nm Ag particles, purchased 60 nm Ag

particles, purchased 10 nm Au particles and 60 nm Au particles. Figure 3-6 shows the PEG-ylation reaction of the various particles.

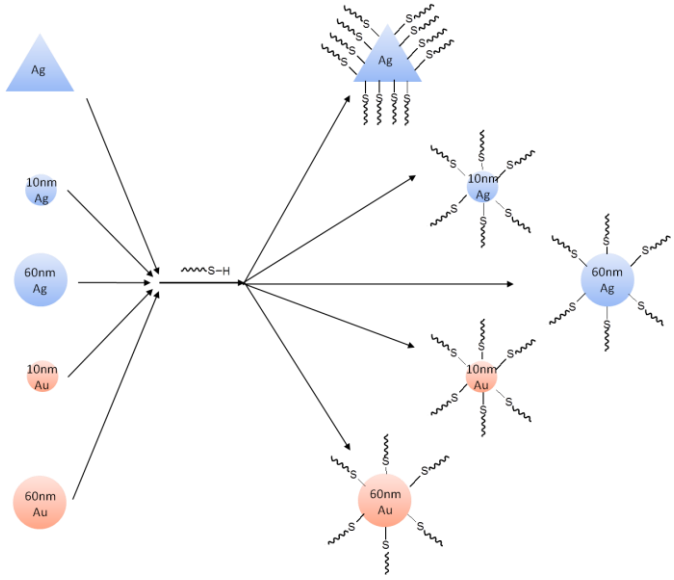

Figure 3-6 - PEG-ylation reaction with nanoparticles

The solvent used in the remainder of the experiments and BHJ cell fabrication is $CHCl_3$. The oDCB was unsuccessful for solubilizing nanoparticles and the blend of $CHCl_3$:oDCB was unsuccessful as a P3HT:PCBM solvent because it produced inhomogeneous films on the substrate surface.

APTES Functionalization of ITO

In order to incorporate the nanoparticles underneath the active layer of the cell, the ITO substrate must be functionalized. This will allow for the particles to adhere to the surface of the anode. APTES was chosen because it is commonly used to functionalize glass substrates by forming an amine functionalized film that is tightly attached to the substrate surface[8]. The reaction of the triethoxy silane group of APTES with the silca on the substrate allows the APTES

to become immobilized on the substrate with the NH_2 groups free to bond with the silver particles as shown in figure 3-7.

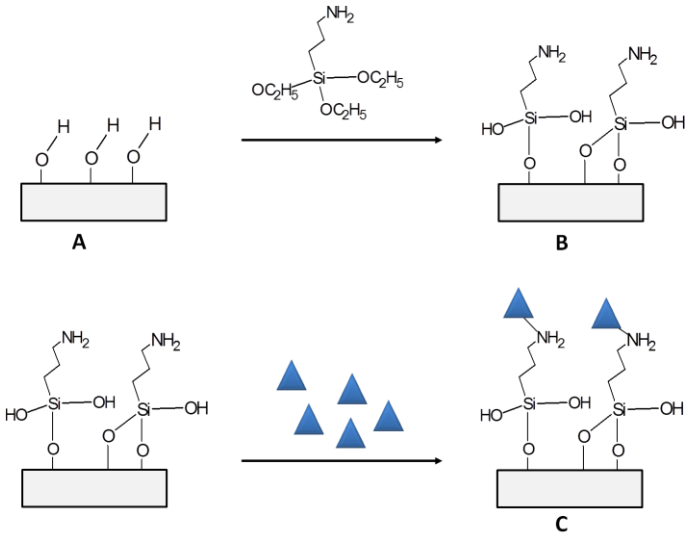

Figure 3-7- Reaction of APTES with substrate and nanoparticles

Figure 3-7(a) shows the cleaned glass substrate containing hydroxyl groups available to react with the APTES. Figure 3-7(b) shows how a layer of APTES reacts with the substrate surface. The free NH_2 groups on the ends of the APTES are left available for reaction with the Ag particles as shown in figure 3-7(c).

The bare glass substrate is much more hydrophilic than the hydrophobic APTES layer. This allows for confirmation of the functionalization using contact angle measurements. If the glass substrates (both non-functionalized and functionalized) are assumed to be perfectly flat, the Young equation (equation 3-1) can be used;

$$0 = \gamma_{SG} - \gamma_{SL} - \gamma_{LG}\cos\theta \qquad (3\text{-}1)$$

Where γ_{SG} is the surface tension between the substrate and the air, γ_{SL} is the surface tension between the substrate and the liquid droplet, γ_{LG} is the surface tension between the liquid

droplet and the air, and θ is the contact angle between the droplet and the surface as shown in figure 3-8.

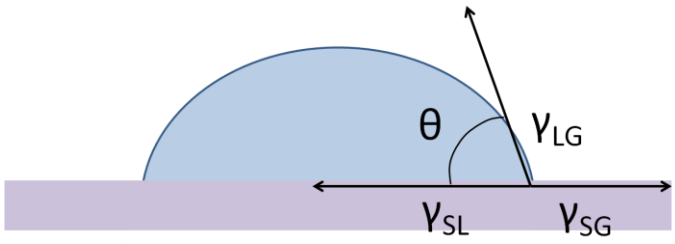

$$0 = \gamma_{SG} - \gamma_{SL} - \gamma_{LG}\cos\theta$$

Figure 3-8 - Contact angle measurement of a water droplet

To confirm the presence of the APTES on the substrate surface, contact angle measurements were done. Figure 3-9(a) shows the bare glass, figure 3-9(b) shows bare ITO, figure 3-9 (c) shows the APTES functionalized glass, and figure 3-9(d) APTES functionalized ITO substrates, all with a 7 μL droplet of water on the surface.

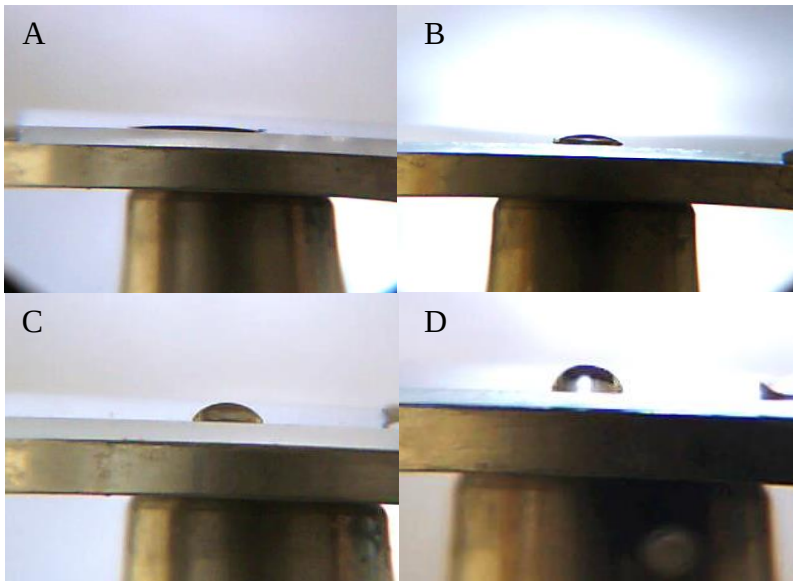

Figure 3-9 - Water Droplets on (A) clean glass, (B) clean ITO, (C) APTES on glass, and (D) APTES on ITO

The larger contact angle of the water with the functionalized surface shows that the APTES has created a layer on the surface of the glass and ITO. A more hydrophobic substrate will repel the water from its surface. The repulsion of the water will lift the droplet away from the surface, creating a taller droplet and a larger contact angle. The results for the contact angle measurements are shown in Table 3-1.

Table 3-1 - Contact angle measurements

Substrate	**Contact Angle**	**Substrate**	**Contact Angle**
Clean Bare Glass	22 ± 6°	Clean Bare ITO	47 ± 4°
APTES Glass	73 ± 7°	APTES ITO	73 ± 4°
Annealed APTES Glass	73 ± 3°	Annealed ITO Glass	79 ± 2°
Difference between Anneal & No Anneal	0 ± 8°	Difference between Anneal & No Anneal	6 ± 4°

The data illustrates that there is a significant increase in the contact angle of the water once the APTES layer has been applied to the substrate surface. This is an indication that the functionalization of the APTES was successful. The data also shows that there is only a small difference in contact angle between the ATPES substrates that were annealed and the ones that were not. This indicates that the annealing step is unnecessary for increasing the contact angle and the hydrophobicity of the substrates.

To ensure that the layer of APTES will not disrupt cell function sheet resistance measurements were made. In order to find the resistivity of a sample, the geometrical dimensions of the sample must also be known. Sheet resistance is calculated by equation 3-2;

$$R_s = CF \cdot \frac{V}{I} \qquad (3\text{-}2)$$

Where I is the current passed through the sample, V is the measured voltage, and CF is a correction factor (approximately 0.9864). The results that were collected are shown in table 3-2.

Table 3-2 - Resistivity Measurements

Substrate	**R_S (Ω)**
Clean Bare ITO	10.2 ± 0.9
APTES ITO Average	10.2 ± 1.7
Annealed APTES ITO Average	10.5 ± 0.3
Difference Between ITO & APTES ITO	0.0 ± 1.9
Difference Between ITO & Annealed APTES ITO	0.03 ± 0.95
Difference Between APTES ITO & Annealed APTES ITO	0.03 ± 2.12

The results indicate that the addition of the APTES layer does not affect the resistivity of the substrate, and therefore the addition of this layer will hopefully not affect cell performance. Often an annealing step is required to form cross-links between the silane in the APTES and the substrate. The data shows that the difference between the resistivity of the substrates that were annealed and not annealed is negligible. So based on both contact angle and resistivity

measurements, the annealing of the APTES layer at 70°C for 1.5 hours was found to not be necessary.

The incorporation of the nanoparticles onto the APTES functionalized surface after immersion in nanoparticle solution was successful as illustrated in figure 3-10.

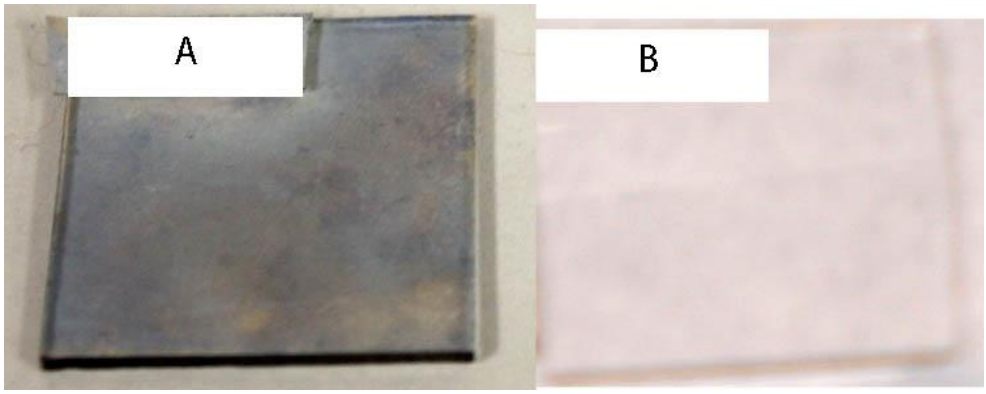

Figure 3-10 - (a) Ag Nanoprisms on APTES functionalized substrate and (b) bare glass substrate

However, the hydrophoicity of the APTES layer presents a problem for cell fabrication. The aqueous based PEDOT:PSS will not be able to effectively spin coat on to the APTES functionalized surface, so a different hole transport layer is required.

PEDOT:PSS Layer Optimization

In order to determine the best spin coating conditions a number of samples were spin coated at different speeds for different amounts of time. The chosen thickness for this layer is 30 nm, as used in a number of literature examples[5-7,9]. The calibration curve for the optimization is shown in figure 3-11.

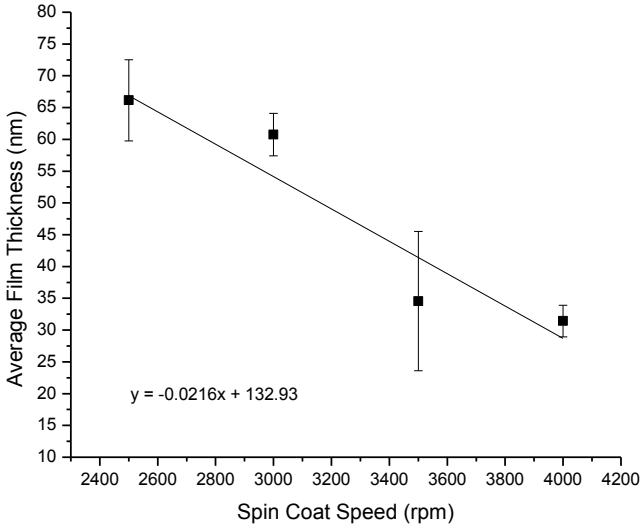

Figure 3-11 - PEDOT:PSS Spin coating Calibration Curve

Figure 3-11 shows that the optimal spin coating speed for a 30 nm film is 4000 rpm. It was found that for device fabrication it is necessary to first deposit the PEDOT:PSS onto the substrate surface and then spin at 200 rpm for 10 seconds for allow the PEDOT:PSS to spread across the entire substrate, then increase the speed to 4000 rpm for 40 seconds to create the 30 nm film.

Layer Optimization of MoO_3

Layers of MoO_3 are not deposited by spin coating. MoO_3 can be thermally evaporated on to the APTES layer after the nanoparticles have been attached. Cells are fabricated by thermally evaporating different thicknesses of MoO_3 onto the substrate, and then device performance is compared to that of a cell containing PEDOT:PSS. MoO_3 has been found in the literature to be an effective substitute for PEDOT:PSS as a buffer layer in BHJ OPVs.[10] Figure 3-12 compares the JV curves of a cell with a 2 nm layer of MoO_3 to a cell with a 30 nm layer of PEDOT:PSS as the hole transport layer. This demonstrates that the MoO_3 is as effective as PEDOT:PSS as a hole transport layer.

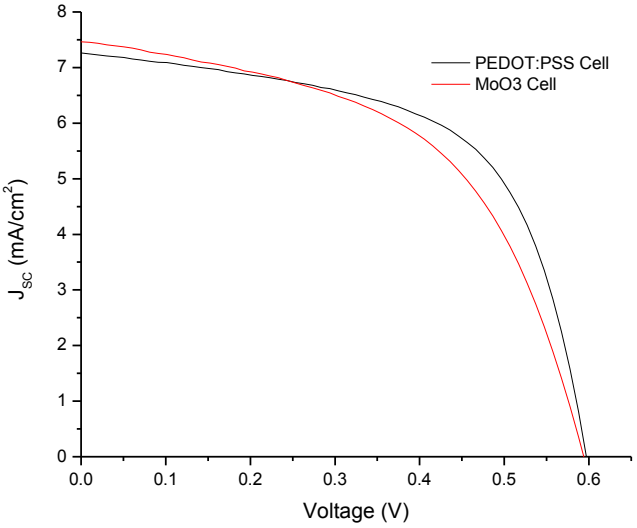

Figure 3-12 – JV curves for MoO_3 and PEDOT:PSS BHJ cells

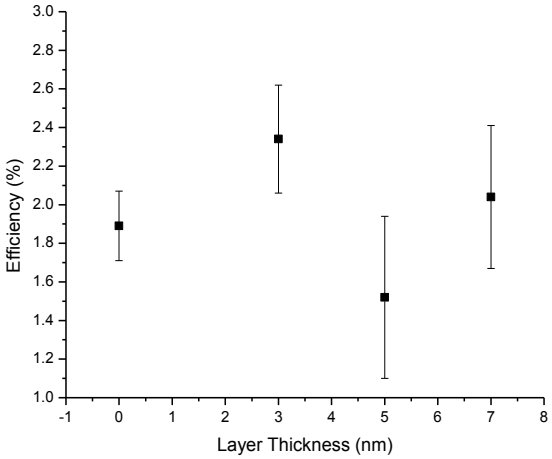

Figure 3-13 – Cell efficiency data for MoO_3 layer thickness calibration

Figure 3-13 shows the efficiency of cells with varying layer thickness of MoO_3. The cell with the best performance had and MoO_3 layer that was 3 nm thick. Therefore, the remainder of the experiments will use 3 nm thick films of MoO_3 in order to maximize the efficiency of the cells.

Control Cell Fabrication

The BHJ cell fabrication is a multistep process. The layer fabrication steps have been optimized throughout the individual layer calibration processes. The layouts of the control cells are shown in figure 3-14.

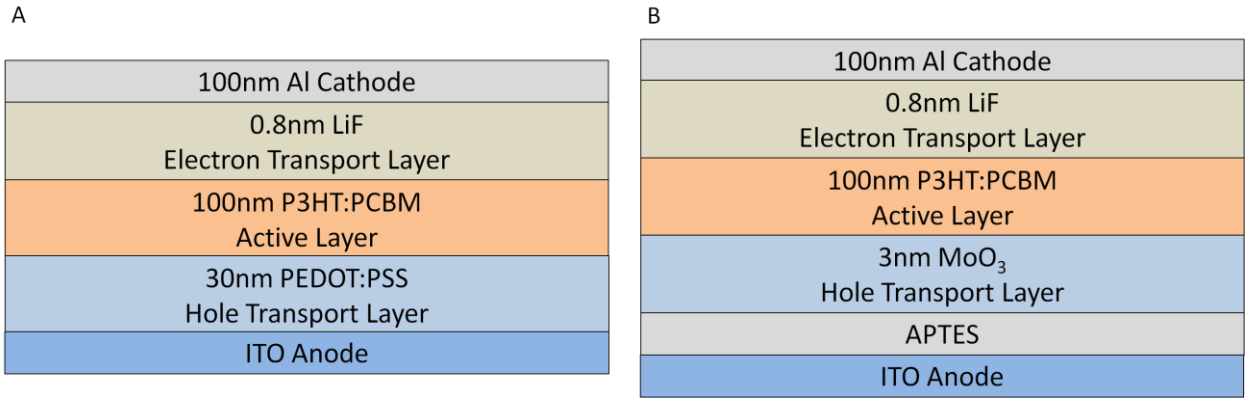

Figure 3-15 - Control cell structures

Figure 3-14(a) shows the device structure of the cell containing PEDOT:PSS as the hole transport layer. This type of cell is the control for the devices that will contain nanoparticles incorporated into the active layer. Figure 3-14(b) shows the device structure of the cell containing the APTES functionalized ITO substrate and MoO_3 as the hole transport layer. This type of cell will be the control for devices that will have nanoparticles incorporated below the hole transport layer.

These cells are built beginning with a cleaned ITO substrate. If fabricating the cell shown in figure 3-14(a), a 30 nm layer of PEDOT:PSS is spin coated on to the surface of the anode. The substrate is quickly transferred into the glove box and a 100 nm layer of P3HT:PCBM is spin coated on top. After drying, the 0.8 nm layer LiF electron transport layer, and 100 nm layer of Al cathode are thermally evaporated. Annealing of the active layer is done after this step to ensure a

better film morphology. If fabricating the cell type shown in figure 3-14(b), APTES is functionalized to the anode surface. The substrate is transferred into the glove box and 3 nm of MoO_3 is thermally evaporated on top of the APTES. A 100 nm layer of P3HT:PCBM is spin coated on top and allowed to dry. After drying, the 0.8 nm LiF electron transport layer, and the 100 nm Al cathode, are thermally evaporated over the active layer. Annealing of the active layer is completed after capping with LiF and Al, to encourage even active layer film morphology. The JV representative curves for the control cells are shown in figure 3-15.

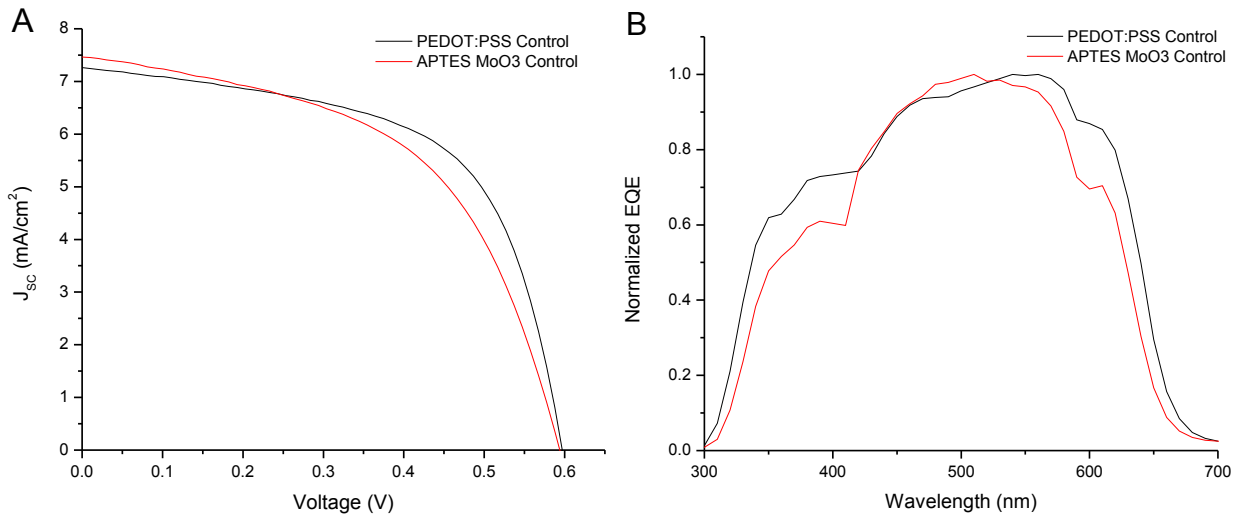

Figure 3-15 – (a) JV curves and (b) normalized EQE spectra of BHJ control cells

The JV curve data shown in figure 3-15(a) is from a cell that is representative of the average of the cells. To better compare the shapes of the spectra, the normalized EQE results are shown in figure 3-15(b), and are also representative of the average results.

The EQE spectra show that the APTES MoO_3 control cells have a narrower absorption band than the PEDOT:PSS control cells, but the overall shape of the spectra are similar. These slight changes may be due to the different absorption of the different hole transport layers.

The device performance parameters are summarized in table 3-3. The data in the brackets are the values from the cell with the highest efficiency.

Table 3-3 - Cell performance parameters for BHJ control cells

Control Cell Type	V_{OC} (V)	J_{SC} (mA/cm^2)	Fill Factor	Efficiency (%)
PEDOT:PSS	0.59 ± 0.01 (0.59)	7. 8 ± 1.1 (9.0)	56 ± 6 (63)	2.6 ± 0.4 (3.4)
APTES MoO_3	0.63 ± 0.03 (0.59)	5.4 ± 2.4 (7.5)	51 ± 2 (52)	1.7 ± 0.6 (2.3)

The number of control cells fabricated is large in order to narrow the error of the cell parameters. There were 44 PEDOT:PSS control cells produced, tested, and averaged, and 10 APTES MoO_3 control cells. The number of APTES MoO_3 control cells is much lower due to a high device failure rate. The control cells are now compared to cells containing metal nanoparticles to determine whether the incorporation of the nanoparticles will enhance the performance of the BHJ cells.

25 nm Ag Nanoprisms

Once the device fabrication is optimized, the PEG-ylated nanoparticles can be incorporated into the active layer. The particles are incorporated into the cell in different concentrations. The concentrations of particles are varied in terms of optical density, or how much the particles absorb in a UV-Vis measurement. The concentrations of Ag nanoprisms that are incorporated into the BHJ cells are equivalent to optical densities of 0.1, 0.05 and 0.25. This means that the final concentration of nanoparticles in the active layer solution would show absorbances of 0.1, 0.05 and 0.025. The 25 nm Ag nanoprisms are subject to shape degradation as discussed in Chapter 2. The sharp tips that are expected to enhance the absorption properties of the active layer may have rounded once incorporated into the cell. It is expected that within

the short time frame of fabrication and testing the particles retain their triangular shape, but there is no way to confirm that the cell fabrication does not accelerate this morphology change. The JV curve and EQE results for cells containing the PEG-ylated 25 nm Ag nanoprisms in the active layer are shown in figure 3-16.

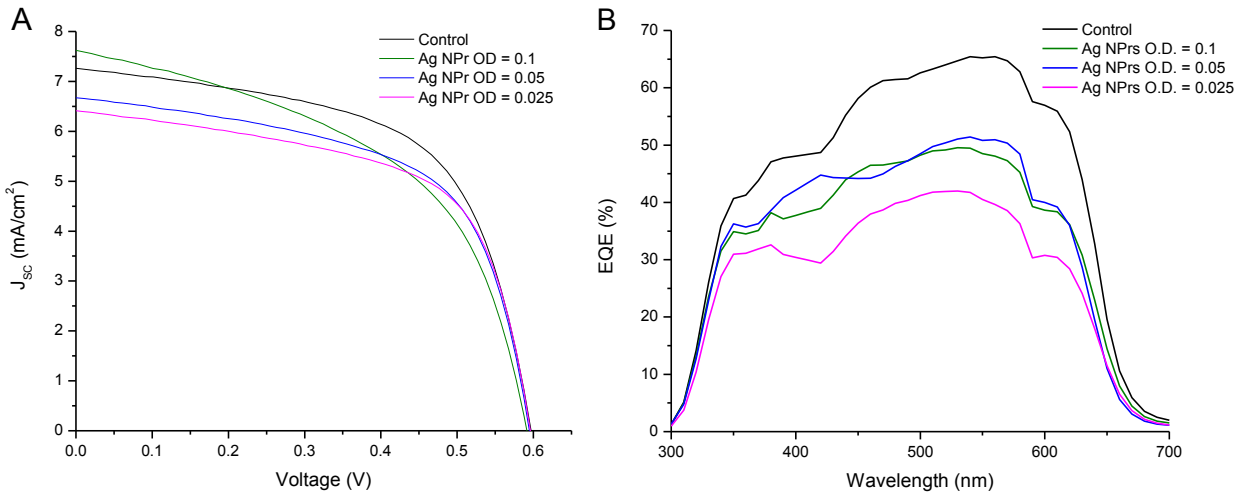

Figure 3-16 – (a) JV curves and (b) EQE spectra of BHJ cells with 25 nm Ag nanoprisms

The data presented in figure 3-16 are from cells that are representative of the average values. All of the cells tested that contained the 25 nm Ag nanoprisms had JV curves that show lower current densities than the control cell as shown in figure 3-16(a). This result is echoed in the EQE spectra shown in figure 3-16(b). There is a significant decrease in EQE for all of the cells containing the Ag nanoprisms, as well as not much of a change in the shape of the spectra.

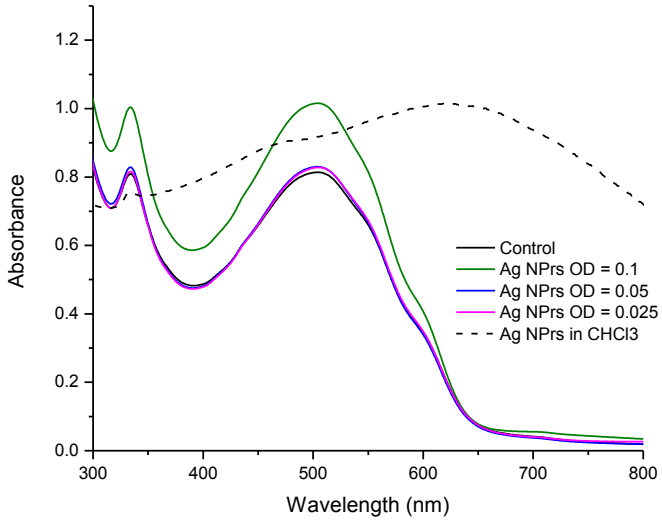

Figure 3-17 - UV-Vis spectra of active layers of BHJ cells with 25 nm Ag nanoprisms

Figure 3-17 shows the UV-Vis spectra of the active layers of the cells containing Ag nanoprisms. It compares the cells to a control cell as well as to the UV-Vis spectrum of the PEG-ylated Ag nanoprisms in $CHCl_3$. As in the characterization before, there is not much of a change in the UV-Vis spectra of the active layers containing the Ag nanoprisms compared to the control spectrum. The increase in absorbance in the active layer containing an Ag optical density of 0.1, is most likely due to film thickness, because no increase in performance or light conversion is seen in any other type of characterization.

The cell performance data for BHJ cells containing 25 nm Ag nanoprisms are tabulated in table 3-4. The values are given as averages of a number of measurements; the numbers in brackets are the values from the best performing cell.

Table 3-4 – Cell performance parameters for BHJ cells with 25 nm Ag nanoprisms

Ag Optical Density	V_{OC} (V)	J_{SC} (mA/cm^2)	Fill Factor	Efficiency (%)
Control	0.59 ± 0.01 (0.59)	7.78 ± 1.1 (9.0)	56 ± 6 (63)	2.6 ± 0.4 (3.4)
0.1	0.60 ± 0.01 (0.59)	7.1 ± 0.3 (7.1)	52 ± 5 (56)	2.2 ± 0.2 (2.4)
0.05	0.59 ± 0.00 (0.61)	6.7 ± 0.0 (7.9)	58 ± 1 (62)	2.3 ± 0.0 (2.9)
0.025	0.59 ± 0.01 (0.59)	6.6 ± 0.5 (7.1)	59 ± 4 (61)	2.3 ± 0.3 (2.6)

It is seen in table 3-4 that the efficiencies of the cells do not seem to change much at all. This suggests that the addition of the nanoprisms does not change the efficiency of the BHJ cells, either or better or for worse. The results are the same for the J_{SC} values of the measured cells. The results show that the J_{SC} values decrease upon the addition of the nanoprisms, suggesting that the particles may be negatively affecting the cell function. However these values are all within the error of the J_{SC} of the control cell, illustrating that the nanoprisms do not affect the J_{SC} of the cells.

To confirm these results a t-test was done comparing the J_{SC} values of the cells comparing the Ag nanoprisms to the control cell. These results are shown in table 3-5.

Table 3-5 - Ag nanoprisms t-test results for J_{SC} values

Ag Optical Density	t Statistic	t Critical	Average Value Compared to Control	Conclusion
0.10	3.60	2.45	Decreased	t stat > t crit Reject Null Hypothesis Difference
0.05	4.22	2.02	Decreased	t stat > t crit Reject Null Hypothesis Difference
0.025	1.55	4.30	Decreased	t stat > t crit Accept Null Hypothesis No Difference

When Ag nanoprisms were incorporated into the cell, there was a statistically significant decrease in the J_{SC} values at all concentrations of nanoparticles and a statistically significant decrease in the cells that contain the 0.1 and 0.05 optical densities of particles. The efficiency of the cell containing an Ag optical density of 0.025 showed no statistically significant difference from the control cell. These conclusions are echoed in the JV curves and EQE spectra of the devices, and UV-Vis spectra of the active layers.

10 nm Ag Nanoparticles

The JV curves and EQE spectra for the fabricated cells containing 10 nm Ag nanoparticles in the active layer are shown in figure 3-18.

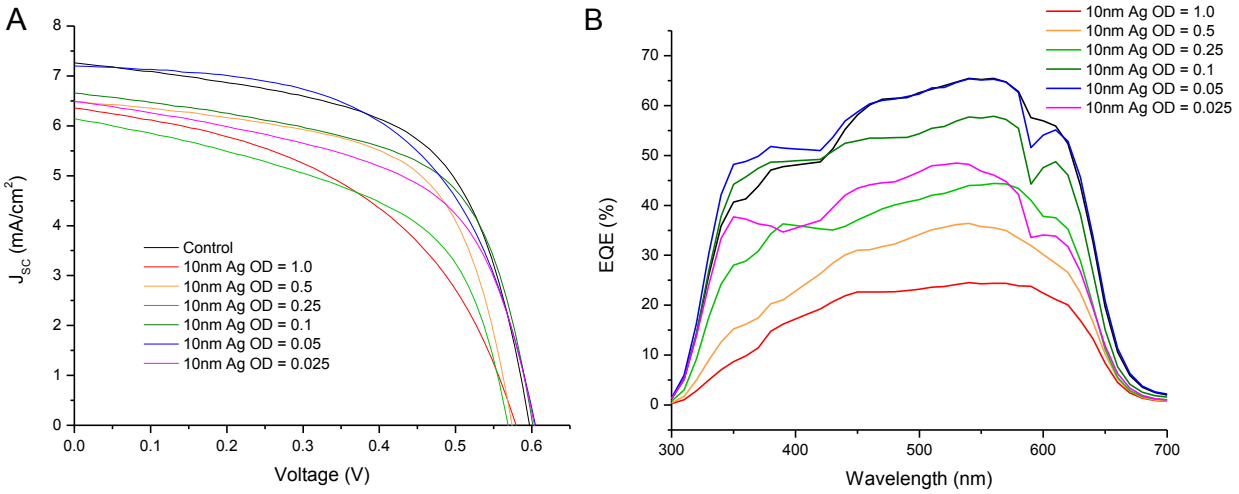

Figure 3-18 – (a) JV curves and (b) EQE spectra of BHJ cells with 10 nm Ag nanoparticles

The data presented in figure 3-18 are of cells that are representative of the average data. Figure 3-18(a) shows how almost all of the cells that have 10 nm Ag nanoparticles incorporated are not as efficient as the control cell. The only one that is comparable is the cell containing Ag nanoparticles with an optical density of 0.05. None of the cells with 10 nm Ag nanoparticles perform better than the control cell. The EQE data in figure 3-18(b) shows over which wavelengths the cell absorbs light and converts it to electrical energy. The cells that have 10 nm Ag nanoparticles with optical densities of 0.1 and 0.05 show a slight increase compared to the control in the 330-450 nm range. The cells with the highest concentration of 10 nm Ag nanoparticles, as well as the cell with only a very small about of 10 nm Ag nanoparticles show a large decrease compared to the control cell.

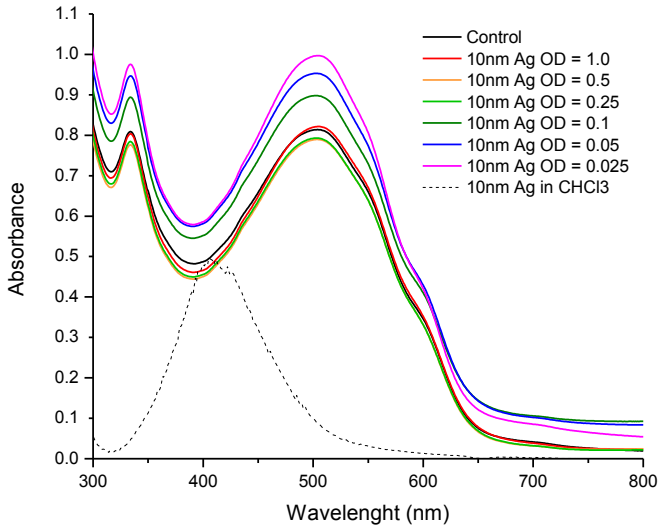

Figure 3-19 - UV-Vis of active layers of BHJ cells with 10 nm Ag nanoparticles

Figure 3-19 shows the UV-Vis spectra of the active layers of the cells containing 10 nm Ag nanoparticles. It compares the cells to a control cell as well as to the UV-Vis spectrum of the PEG-ylated 10 nm Ag nanoparticles in $CHCl_3$. If the 10 nm Ag nanoparticles contributed to an increase in the absorbance of the active layer, an increase in absorbance of the active layers in the same region that the particles alone absorb is expected. Some of the spectra do show an increase in absorbance compared to the control, but this increase occurs over the entire absorption spectrum, meaning it is likely due to variance in film thickness, not the particles.

Table 3-6 shows the cell performance data for BHJ cells containing 10 nm Ag nanoparticles. The values are given as averages with standard deviation, and the numbers in brackets are the values from the best performing cell.

Table 3-6 - Cell performance parameters for BHJ cells with 10 nm Ag nanoparticles

Ag Optical Density	V_{OC} (V)	J_{SC} (mA/cm^2)	Fill Factor	Efficiency (%)
Control	0.59 ± 0.01 (0.59)	7.8 ± 1.1 (9.0)	56 ± 6 (63)	2.6 ± 0.4 (3.4)
1.00	0.58 ± 0.00 (0.58)	6.2 ± 1.3 (6.7)	48 ± 8 (60)	1.8 ± 0.6 (2.4)
0.50	0.59 ± 0.01 (0.60)	6.7 ± 0.6 (7.6)	59 ± 2 (60)	2.3 ± 0.3 (2.7)
0.25	0.59 ± 0.01 (0.58)	6.2 ± 0.3 (6.2)	49 ± 5 (57)	1.8 ± 0.2 (2.2)
0.10	0.60 ± 0.01 (0.60)	7.9 ± 0.7 (8.7)	47 ± 13 (63)	2.3 ± 0.7 (3.3)
0.05	0.60 ± 0.00 (0.60)	7.8 ± 1.4 (9.2)	53 ± 9 (57)	2.4 ± 0.4 (3.1)
0.025	0.60 ± 0.00 (0.60)	6.5 ± 0.5 (7.4)	56 ± 3 (57)	2.2 ± 0.2 (2.5)

The V_{OC} values for these cells, like the cells that contain 10 nm Ag nanoparticles are unremarkable. This is an indication that addition of the nanoparticles does not affect the active layer and the electrode-organics interface remains unchanged.[11] The data illustrates that there is no increase in overall cell efficiency after the addition of these particles. The cells with the particles all show a decrease in overall efficiency. The results are the same for the J_{SC} values of the measured cells. It is seen that there may be a slight increase in the J_{SC} values for the cells with the Ag optical density of 0.05, but upon further mathematical analysis it is found to not be statistically significant. A t-test was completed comparing the efficiency values of the cells containing the 10 nm Ag nanoparticles with the control cell, with the results shown in table 3-7. It was found that only half of these efficiencies (Ag optical densities of 1.00, 0.25, and 0.025) had a statistically significant decrease.

Table 3-7 – 10 nm Ag nanoparticles t-test results for efficiency values

Ag Optical Density	t Statistic	t Critical	Average Value Compared to Control	Conclusions
1.00	2.96	2.78	Decreased	t stat > t crit Reject Null Hypothesis Difference
0.50	1.98	2.26	Decreased	t stat < t crit Accept Null Hypothesis No Difference
0.25	7.90	2.12	Decreased	t stat > t crit Reject Null Hypothesis Difference
0.10	1.31	2.31	Decreased	t stat < t crit Accept Null Hypothesis No Difference
0.05	0.81	2.26	Decreased	t stat < t crit Accept Null Hypothesis No Difference
0.025	3.48	2.20	Decreased	t stat > t crit Reject Null Hypothesis Difference

All of the J_{SC} values showed a statistically significant decrease compared to the control except for the cells containing an optical density of 0.5 and 0.25. The results of the t-tests comparing the J_{SC} values of control cell to the cells containing the 10 nm Ag nanoparticles are shown in table 3-8.

Table 3-8 – 10 nm Ag nanoparticles t-test results for J_{SC} values

Ag Optical Density	t Statistic	t Critical	Average Value Compared to Control	Conclusions
1.00	2.62	2.57	Decreased	t stat > t crit Reject Null Hypothesis Difference
0.50	3.62	2.23	Decreased	t stat > t crit Reject Null Hypothesis Difference
0.25	7.99	2.02	Decreased	t stat > t crit Reject Null Hypothesis Difference
0.10	0.54	2.12	Increased	t stat < t crit Accept Null Hypothesis No Difference
0.05	0.17	2.26	Increased	t stat < t crit Accept Null Hypothesis No Difference
0.025	4.78	2.12	Decreased	t stat > t crit Reject Null Hypothesis Difference

These devices showed an increase in J_{SC}, but the increase is not statistically significant compared to the control. This is confirmed by the lack of increase in the JV curves, EQE spectra, and UV-Vis spectra compared to the control cell.

60 nm Ag Nanoparticles

The JV curves and EQE results for the fabricated cells containing 60 nm Ag nanoparticles are shown in figure 3-20.

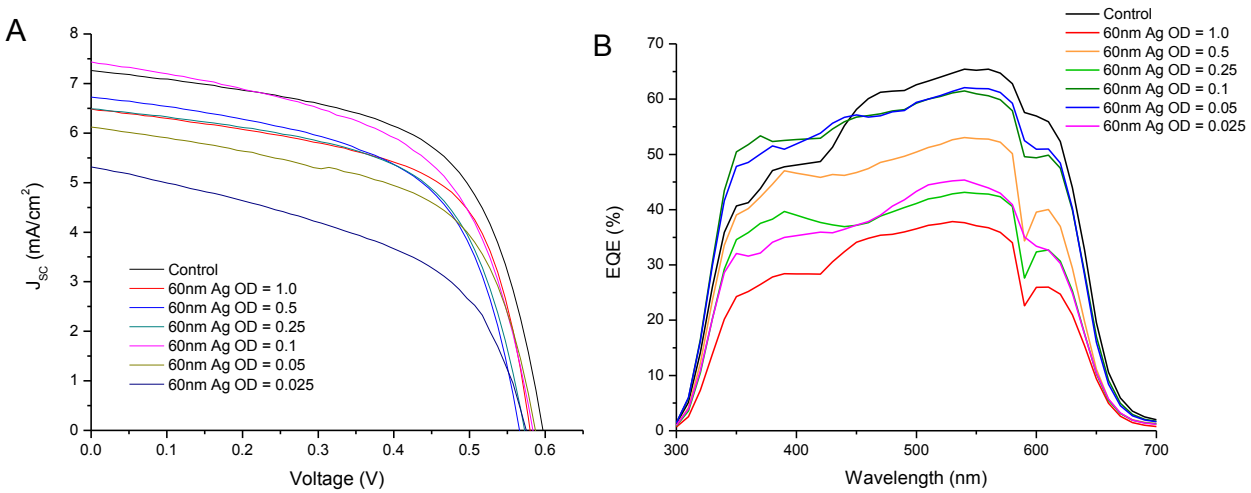

Figure 3-20 – (a) JV curves and (b) EQE spectra for BHJ cells with 60 nm Ag nanoparticles

The data presented in figure 3-20 are of cells that are representative of the average data. All of the JV curves for the cells with 60 nm Ag nanoparticles shown in figure 3-20(a) show lower current densities than the control curve. This is an indication that the 60 nm Ag nanoparticles do not cause an increase in cell efficiency. The EQE results shown in figure 3-20(b) are similar to that of the 10 nm Ag nanoparticles. The overall EQE of all the cells is lower than the EQE of the control except the cells that contain an optical density of 0.1 and 0.05. To better compare the differences in the EQE, the results are normalized as shown in figure 3-21. The cells with optical density between 0.5 and 0.05 show an increase in EQE between 330-440 nm in the normalized spectra. This indicates that these concentrations of particles may positively affect the absorbance of the active layers.

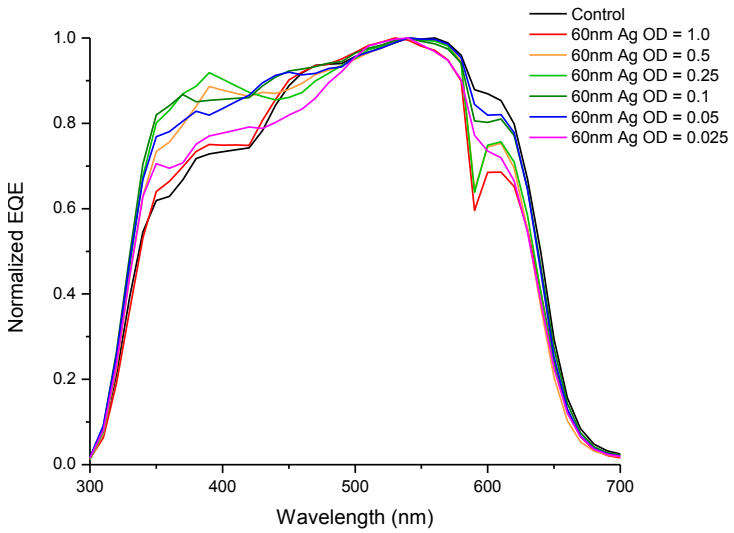

Figure 3-21 - Normalized EQE spectra for BHJ cells with 60 nm Ag nanoparticles

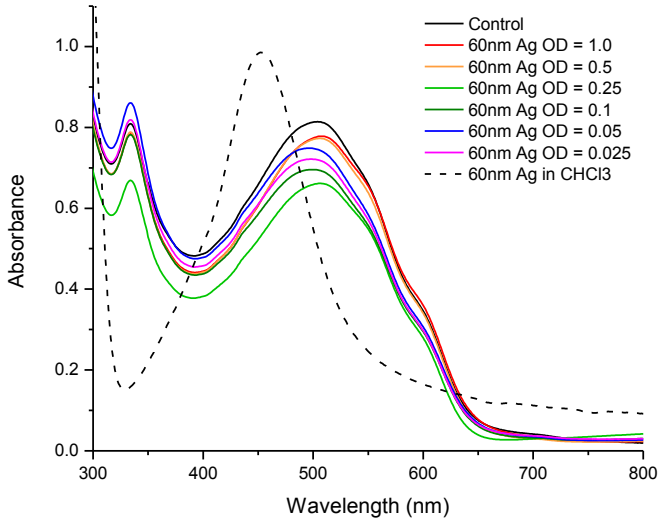

Figure 3-22 - UV-Vis of active layers of BHJ cells containing 60 nm Ag nanoparticles

Figure 3-22 shows the UV-Vis spectra of the active layers containing 60 nm Ag nanoparticles compared to the control and the PEG-ylated 60 nm Ag nanoparticles in $CHCl_3$. It can be seen that there is no increase in the absorbance of the active layer upon addition of the 60 nm Ag nanoparticles. All of the active layers that contain particles have lower absorbance than

the control. There is also no change in the shape of the spectra of the active layers that contain the particles. This is another indication that the particles are not contributing to changing the absorbance of the active layers.

The cell performance data for BHJ cells containing 60 nm Ag nanoparticles is tabulated in table 3-9. The values are given as averages of a number of measurements; the numbers in brackets are the values from the best performing cell.

Table 3-9 - Cell performance parameters for BHJ cells with 60 nm Ag nanoparticles

Au Optical Density	V_{OC} (V)	J_{SC} (mA/cm^2)	Fill Factor	Efficiency (%)
Control	0.59 ± 0.01 (0.59)	7.8 ± 1.1 (9.0)	56 ± 6 (63)	2.6 ± 0.4 (3.4)
1.00	0.58 ± 0.00 (0.58)	6.6 ± 0.4 (6.7)	60 ± 1 (62)	2.3 ± 0.1 (2.4)
0.50	0.58 ± 0.01 (0.57)	7.3 ± 0.5 (7.4)	49 ± 11 (63)	2.1 ± 0.4 (2.7)
0.25	0.57 ± 0.01 (0.58)	6.4 ± 0.9 (7.8)	60 ± 4 (64)	2.2 ± 0.5 (2.9)
0.10	0.59 ± 0.01 (0.60)	7.6 ± 1.0 (8.9)	50 ± 12 (65)	2.3 ± 0.7 (3.5)
0.05	0.58 ± 0.01 (0.59)	7.1 ± 1.0 (7.8)	51 ± 11 (57)	2.1 ± 0.4 (2.6)
0.025	0.58 ± 0.01 (0.59)	6.9 ± 0.2 (6.7)	36 ± 18 (57)	1.4 ± 0.7 (2.3)

The V_{OC} values for these cells, like the cells that contain Ag nanoparticles are unremarkable and within error of each other. The data illustrates that there is no increase in overall cell efficiency after the addition of these particles. The data also shows that the J_{SC} values for the cells containing 60 nm Ag nanoparticles are all lower than the J_{SC} of the control cell.

The incorporation of 60 nm Ag nanoparticles showed a decrease in efficiency, and like the 10 nm Ag nanoparticles only half (Ag optical densities of 1.0, 0.5, and 0.05) of these decreases are statistically significant compared to the control device. The t-test results comparing

the efficiency of the control cell to the cells containing the 60 nm Ag nanoparticles are shown in table 3-10.

Table 3-10 – 60 nm Ag nanoparticles t-test for efficiency values

Ag Optical Density	t Statistic	t Critical	Average Value Compared to Control	Conclusions
1.00	4.01	2.02	Decreased	t stat > t crit Reject Null Hypothesis Difference
0.50	3.10	2.26	Decreased	t stat > t crit Reject Null Hypothesis Difference
0.25	1.94	2.36	Decreased	t stat < t crit Accept Null Hypothesis No Difference
0.10	1.17	2.31	Decreased	t stat < t crit Accept Null Hypothesis No Difference
0.05	3.68	2.23	Decreased	t stat > t crit Reject Null Hypothesis Difference
0.025	2.77	4.30	Decreased	t stat < t crit Accept Null Hypothesis No Difference

Table 3-11 - 60 nm Ag nanoparticles t-test for J_{SC} values

Ag Optical Density	t Statistic	t Critical	Average Value Compared to Control	Conclusions
1.00	6.37	2.02	Decreased	t stat > t crit Reject Null Hypothesis Difference
0.50	1.86	2.07	Decreased	t stat < t crit Accept Null Hypothesis No Difference
0.25	3.45	2.26	Decreased	t stat > t crit Reject Null Hypothesis Difference
0.10	0.59	2.20	Decreased	t stat < t crit Accept Null Hypothesis No Difference
0.05	1.70	2.23	Decreased	t stat < t crit Accept Null Hypothesis No Difference
0.025	4.28	2.14	Decreased	t stat > t crit Reject Null Hypothesis Difference

The t-test results comparing the J_{SC} values of the control cell to the cells containing 60 nm Ag nanoparticles are shown in table 3-11.

The same conclusion as for the efficiency values is true for the J_{SC} values, all are decreased compared to the control, and only half (Ag optical densities of 1.0, 0.25, and 0.025) are statistically different from the control device. The same conclusions are shown in the JV curves, EQE spectra, and UV-Vis spectra.

10 nm Au Nanoparticles

The JV curves and EQE results for the fabricated cells containing 10 nm Au nanoparticles are shown in figure 3-23.

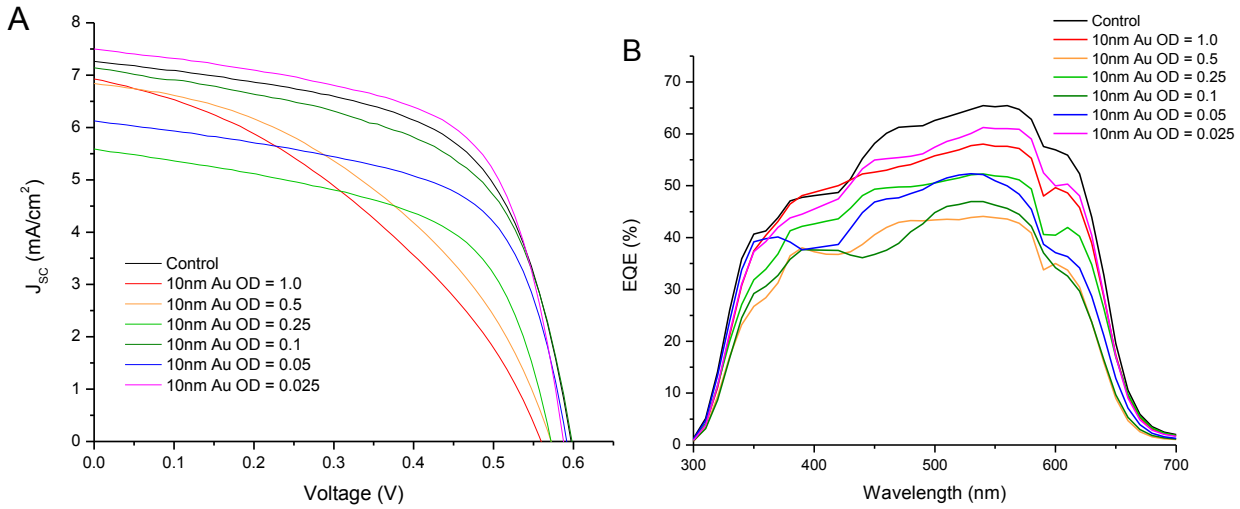

Figure 3-23 – (a) JV curves and (b) EQE spectra for BHJ cells with 10 nm Au nanoparticles

The data presented in figure 3-23 are of cells that are representative of the average data. All of the JV curves for the cells with 10 nm Au nanoparticles shown in figure 3-23(a) show lower current densities than the control curve, except for the cell containing the lowest concentration of 10 nm Au nanoparticles. The JV curves for the cells containing 10 nm Au with optical densities of 1.0 and 0.5 are poorly shaped. While an S shaped JV curve can be an indication of a poor PEDOT:PSS layer[3], these curves are not true S shaped, they just have low fill factor. This is an indication that the 10 nm Au nanoparticles may be negatively affecting the active layer. The EQE results shown in figure 3-23(b) show that all of the cells that contain the 10 nm Au nanoparticles exhibit an EQE lower than that of the control cell. The cells with the optical densities of 1.0, 0.5, and 0.25, have a slight change in spectra shape compared to the control in the 360-440 nm region. This may be due to the 10 nm Au nanoparticles in the active

layer. Figure 3-24 shows the UV-Vis spectra of the active layers containing 10 nm Au nanoparticles compared to the control and the PEG-ylated 10 nm Au nanoparticles in $CHCl_3$.

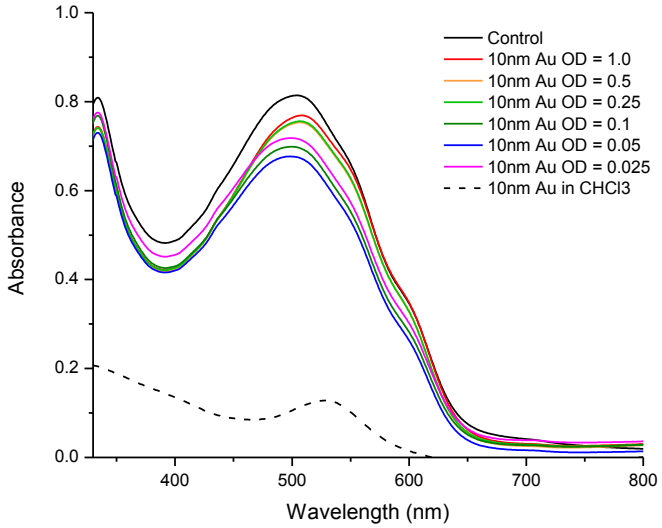

Figure 3-24 - UV-Vis spectra of active layers of BHJ cells with 10 nm Au nanoparticles

The UV-Vis spectra of the active layers show no increase or change in the absorption spectrum shape of the active layers that contain 10 nm Au particles compared to the control. If the particles positively affected the active layer absorbance an increase in absorbance of the active layer would be expected in the same region that the PEG-ylated Au nanoparticles absorb.

The cell performance data for BHJ cells containing 10 nm Au nanoparticles is tabulated in table 3-12. The values are given as averages of a number of measurements; the numbers in brackets are the values from the best performing cell.

Table 3-12- Cell performance parameters for BHJ cells with 10 nm Au nanoparticles

Au Optical Density	V_{OC} (V)	J_{SC} (mA/cm^2)	Fill Factor	Efficiency (%)
Control	0.59 ± 0.01 (0.59)	7.8 ± 1.1 (9.0)	56 ± 56 (63)	2.6 ± 0.4 (3.4)
1.00	0.56 ± 0.01 (0.57)	6.7 ± 0.5 (6.2)	39 ± 9 (52)	1.5 ± 0.3 (1.9)
0.50	0.56 ± 0.01 (0.57)	6.5 ± 0.5 (7.0)	40 ± 10 (58)	1.5 ± 0.3 (1.9)
0.25	0.56 ± 0.01 (0.57)	6.4 ± 0.5 (6.4)	53 ± 6 (60)	1.9 ± 0.2 (2.2)
0.10	0.59 ± 0.02 (0.60)	6.5 ± 0.9 (6.8)	43 ± 21 (61)	1.7 ± 1.0 (2.5)
0.05	0.59 ± 0.00 (0.59)	6.5 ± 0.7 (7.6)	57 ± 3 (57)	2.2 ± 0.3 (2.6)
0.025	0.59 ± 0.00 (0.59)	8.1 ± 0.9 (8.3)	56 ± 4 (58)	2.7 ± 0.2 (2.9)

The V_{OC} values for these cells, like the cells that contain Ag nanoparticles are unremarkable. They are very similar and do not show much variation. There appears to be a slight increase in cell efficiency for the cell containing 10 nm Au nanoparticles with an optical density of 0.025, but when the error with the averages are taken into consideration, the increase is not significant. The same sort of apparent trend occurs in the J_{SC} values of the cells, there appears to be an increase in J_{SC} for the cell with the Au optical density of 0.025, but this increase is trivial when compared to the error associated with the averages.

The incorporation of the 10 nm Au particles looks to be a somewhat positive result, for the cell containing an Au optical density of 0.025. It is the only cell that shows an increase in efficiency. Unfortunately the t-test shows that it is not a significant increase compared to the control cell. This cell is also the only cell containing 10 nm Au nanoparticles that shows an increase in J_{SC}, but like the efficiency, the increase is not significant. These t-test results are shown in table 3-13.

Table 3-13 - T-test values for BHJ cells with 10 nm Au of optical density of 0.025

	t Stat	t Crit	Conclusions
Compare Efficiency	0.85	2.26	t stat < t crit Accept Null Hypothesis No Difference
Compare JSC	0.72	2.36	t stat < t crit Accept Null Hypothesis No Difference

60 nm Au Nanoparticles

The JV curves and EQE spectra for the fabricated cells containing 60 nm Ag nanoparticles are shown in figure 3-25.

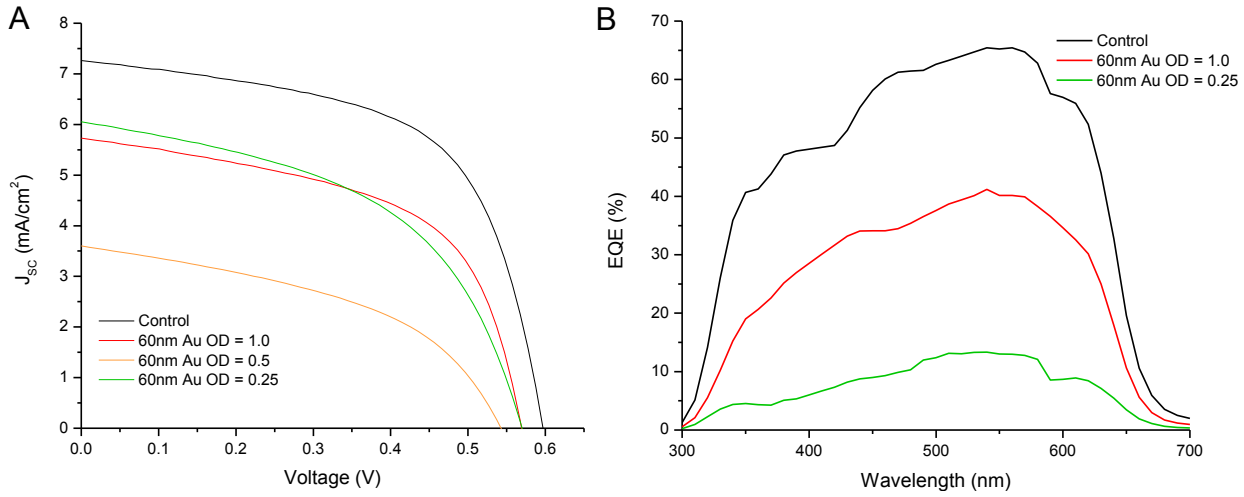

Figure 3-25 – (a) JV curves and (b) EQE spectra of BHJ cells with 60 nm Au nanoparticles

The data presented in figure 3-25 are of cells that are representative of the average data. All of the JV curves for the cells with 60 nm Au nanoparticles shown in figure 3-25(a) are considerably lower than the control curve. This is an indication that the incorporation of the 60 nm Au particles disrupts cell function instead of enhancing it. The EQE data is shown in figure

3-25(b), it should be noted that the EQE data for the cell containing 60 nm Au nanoparticles with an optical density of 0.5 was not measurable, and therefore omitted. This may have been due to instrument failure and/or cell degradation. The EQE data echoes the JV curve data. The incorporation of the 60 nm Au nanoparticles interrupts cell function and for the cells containing Au particles with an optical density of 0.25, there is a significant EQE drop in the 340-480 nm region.

Figure 3-26 shows the UV-Vis spectra of the active layers containing 60 nm Au nanoparticles compared to the control and the PEG-ylated 60 nm Ag nanoparticles in $CHCl_3$.

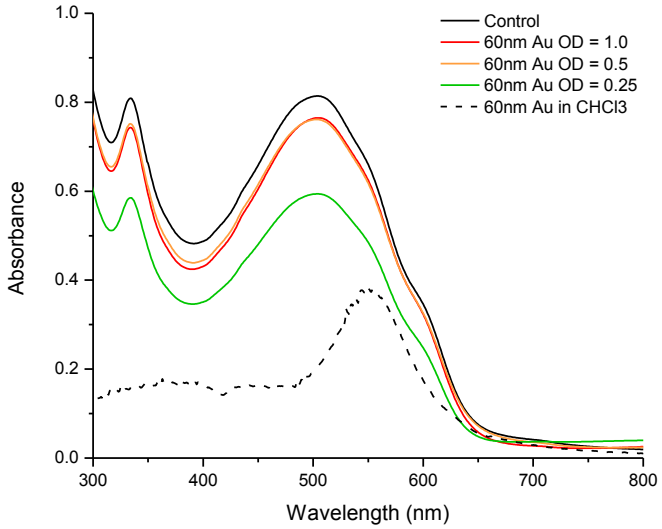

Figure 3-26 - UV-Vis spectra of active layers of BHJ cells with 60 nm Au nanoparticles

The UV-Vis spectra of the active layers containing 60 nm Au nanoparticles are lower than the absorption of the control cell. This is consistent with both the JV curve and EQE data, suggesting that the Au nanoparticles do not enhance the active layer's light absorption. The absorption of the PEG-ylated particles is compared to the spectra of the active layers and illustrates how there is no increase of absorption in the same region.

Table 3-14 shows the cell performance data for BHJ cells containing 10 nm Au nanoparticles. The values are given as averages with standard deviation, and the numbers in brackets are the values from the best performing cell.

Table 3-14 - Cell performance parameters for BHJ cells with 60 nm Au nanoparticles

Au Optical Density	V_{OC} (V)	J_{SC} (mA/cm^2)	Fill Factor	Efficiency (%)
Control	0.59 ± 0.01 (0.59)	7.8 ± 1.1 (9.0)	56 ± 6 (63)	2.6 ± 0.4 (3.4)
1.00	0.57 ± 0.01 (0.57)	6.0 ± 1.2 (7.6)	54 ± 4 (58)	1.8 ± 0.5 (2.5)
0.50	0.55 ± 0.01 (0.54)	3.7 ± 0.5 (4.5)	45 ± 1 (43)	0.9 ± 0.1 (1.1)
0.25	0.55 ± 0.02 (0.57)	6.4 ± 0.4 (6.1)	47 ± 5 (53)	1.6 ± 0.12 (1.9)

The V_{OC} values for these cells, like the other cells examined are unremarkable. They are similar within all of the variations and do not need to be compared cell to cell.

Both the overall cell efficiency and the J_{SC} values confirm the previous data concerning the BHJ cell containing 60 nm Au nanoparticles. Upon the addition of the particles, there is a drop in cell efficiency, which is also evident in the J_{SC} data. This result is similar to the addition of the Ag nanoprisms. The decrease in efficiency is large enough to be significantly different from the control cell for all of the optical densities. The same is true for the J_{SC} values. These results are echoed in the large decreases seen in the JV curve, EQE spectra, and UV-Vis spectra compared to the control.

APTES Functionalized Nanoparticles

The next type of cell studied has a slightly different architecture. These cells have the nanoparticles incorporated beneath the hole transport layer of the cell. In these cells a layer of APTES adheres the Ag nanoprisms to the surface of the substrate and the hole transport layer is

MoO_3. The particles used in this study come from both the first and second nanoprisms syntheses. Figure 3-27 shows the different positions of the plasmon bands of the different types of particles from the two syntheses that are incorporated under the hole transport layer of the APTES MoO_3 BHJ cells. The particles used from the first synthesis have a plasmon band peak at 655 nm. The particles from the second synthesis were made with different amount of seed solution and have plasmon band peaks at 590 and 490 nm.

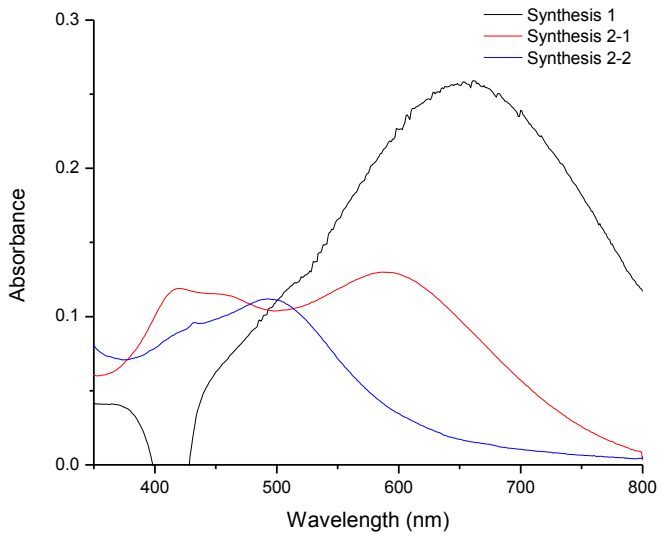

Figure 3-27 - UV-Vis spectra of nanoprisms before incorporation under the active layer

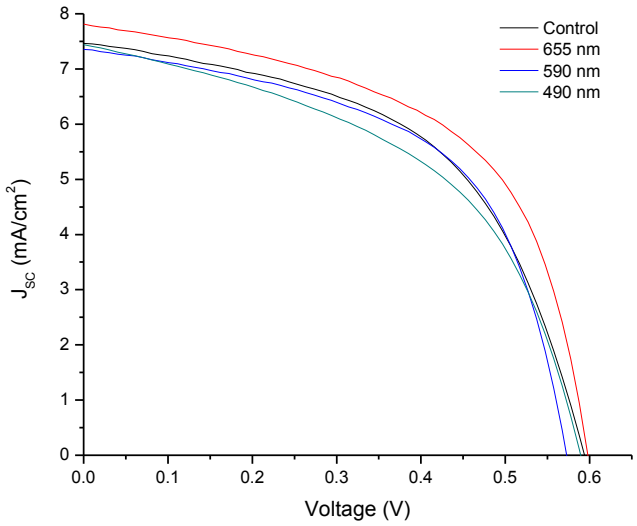

Figure 3-28 - JV curves for BHJ cells with nanoparticles under the active layer

Figure 3-28 shows data from cells representative of the average performing cell. The JV curves for cells containing particles with plasmon peaks at 655, 590 and 490 nm are compared to a control cell.

The cell performance data for BHJ cells containing the APTES functionalized nanoparticles is tabulated in table 3-15. The values are given as averages of a number of measurements; the numbers in brackets are the values from the best performing cell.

Table 3-15 - Cell performance parameters for BHJ cells with nanoparticles under the active layer

Ag Plasmon Band Position	V_{OC} (V)	J_{SC} (mA/cm^2)	Fill Factor	Efficiency (%)
Control	0.63 ± 0.03 (0.59)	5.4 ± 2.4 (7.5)	51 ± 2 (52)	1.7 ± 0.6 (2.3)
655 nm	0.59 ± 0.02 (0.61)	6.9 ± 1.0 (6.4)	48 ± 6 (49)	2.0 ± 0.4 (1.9)
590 nm	0.57 ± 0.01 (0.57)	6.1 ± 0.8 (7.4)	53 ± 5 (55)	1.8 ± 0.4 (2.3)
490 nm	0.59 ± 0.01 (0.59)	7.2 ± 0.3 (7.5)	49 ± 6 (49)	2.0 ± 0.2 (2.2)

The V_{OC} values for these cells, like the cells with the nanoparticles inside the active layer are unremarkable. They are similar within all of the variations and do not need to be compared cell to cell.

It can be seen that even though there appears to be an increase in efficiency upon the addition of the nanoparticles, the increases are all within the error of the control cells. These results are confirmed using a t-test and shown in table 3-16.

Table 3-16 – BHJ cells with nanoparticles under the active layer t-test results for efficiency values

Ag Plasmon Band Position	t Statistic	t Critical	Average Value Compared to Control	Conclusions
655 nm	0.73	2.57	Increased	t stat < t crit Accept Null Hypothesis No Difference
590 nm	0.51	2.78	Increased	t stat < t crit Accept Null Hypothesis No Difference
490 nm	1.11	2.78	Increased	t stat < t crit Accept Null Hypothesis No Difference

Table 3-17 - BHJ cells with nanoparticles under the active layer t-test results for J_{SC} values

Ag Plasmon Band Position	t Statistic	t Critical	Average Value Compared to Control	Conclusion
655 nm	1.14	2.78	Increased	t stat < t crit Accept Null Hypothesis No Difference
590 nm	0.56	3.18	Increased	t stat < t crit Accept Null Hypothesis No Difference
490 nm	1.50	3.18	Increased	t stat < t crit Accept Null Hypothesis No Difference

Similar to the efficiency results, even though there appears to be an increase in the J_{SC} values upon the addition of the nanoparticles, all the increases are within the error of the control cells. This result is again confirmed with a t-test and the results are shown in table 3-17.

Due to the cell failure rate and difficulty spin coating even active layer films, no further measurements such as EQE such as were taken. Also no further experiments incorporating other shapes, sizes or materials of nanoparticles under the active layer were pursued.

Conclusions

In summary, the incorporation of nanoparticles into BHJ cells does not increase the cell efficiency. In order to confirm this, t-tests of the efficiency and J_{SC} data were done comparing each different cell to the control cell. This confirmed that the addition of metallic nanoparticles does not increase the efficiency of a BHJ cell, and in some cases may cause a decrease in efficiency.

Examples from literature show that metal nanoparticles have already been incorporated into OPVs with some success. Li et al. were able to incorporate both spherical Ag nanoparticles and Ag nanoprisms into a P3HT:PCBM BHJ cell, and saw an efficiency enhancement from 3.60% to 4.30% with both spherical nanoparticles and nanoprisms in the cell.[9] However, there is no discussion as to how well the Ag nanoparticles are incorporated into the solvent. The experimental states that the nanoparticles were dried and dispersed into organic solvent, not solubilised. This brings about the question, how evenly distributed are the particles within the active layer? Are the particles spread throughout the active layer, do they settle to the bottom of the active layer, or do they aggregate into much larger particles?

Another example from the literature is work done by Wang et al. In this study Au octahedral nanoparticles were incorporated into a P3HT:PCBM cell, and an increase in efficiency from 3.49% to 4.36% was reported.[7] As with the previous study, the Au nanoparticles were only dispersed within the organic solvent, not solubilised. The experimental section reports ultrasonically agitating the particle/active layer solution to encourage dispersion of the particles throughout the solution. This procedure does not take into account any settling of the particles that may occur after spin coating the solution on to the substrate. Settling may occur during the drying process that would lead to an uneven distribution of the particles throughout the active layer, or an aggregation of the nanoparticles into much larger particles.

In our work, by functionalizing the nanoparticles, we ensure that they are soluble in the organic solvent used to deposit the active layer, allowing for an even distribution throughout the active layer.

One cause of these observed decreases may be from the metallic nanoparticles acting like electron traps. It has been found that metallic nanoparticles can accumulate long-lived negative

charges when they are in contact with a BHJ blend composed of P3HT:PCBM that has been photoexcited.[12] In order to avoid this phenomenon, it is suggested that the particle be coated to protect it from this build-up of electrons. The particles used in this experiment are coated with PEG-SH, which may protect them from electron accumulation, but perhaps this layer of PEG is not thick enough. A longer chain PEG-SH may protect the particles better, and may also, as discussed previously, protect from any shape change of the particle that may occur.

There are examples from the literature of OPVs that have metal nanoparticles under the hole transport layer as well. Work done by Heo et al. reports an efficiency increase from 2.90% to 3.35% upon incorporation of Au-Cu nanoparticle alloys between the hole transport layer and the anode.[13] This study incorporated the metal nanoparticles by using templates and depositing them directly on to the surface of the substrate, allowing for a more even distribution of particles. By not having to functionalize the substrate, this study was able to spin coat the PEDOT:PSS directly onto the nanoparticles. In contrast to our work, this method may result in more uniform layers leading to a lower device failure rate.

In our study, the cells that have the nanoparticles under the hole transport layer also were not effective at increasing the efficiency of the BHJ cells. Particle oxidation during transfer from aqueous solution into the glove box, or oxidation during the thermal evaporation of the MoO_3 may be the cause of these results. By simply soaking the substrates in a solution of nanoparticles, there is no guarantee that there is an even layer of metal nanoparticles on the substrate. This would lead to an uneven coating of hole transport layer, as well as active layer. This may be the reason behind the large number of devices that did not work.

It should be noted that none of the literature studies reported doing any statistical analysis of their enhancement results. If a t-test was done, results may indicate that within the errors of the measurements there was little to no significant device enhancement.

Overall the incorporation of metal nanoparticles was unsuccessful, but great strides in cell development have been made. Procedures for making and testing control cells are consistent, and the incorporation of the nanoparticles into the active layer, and under the hole transport layer are successful. With success being reported in the literature for these types of devices, and a large amount of the cell fabrication parameters optimized, work still needs to be done on improving the efficiency of the cells containing the metal nanoparticles. Perhaps changing the capping agent or chain length of the solubilising polymer will improve the cells with the nanoparticles in the active layer. Finding a way to avoid oxidation of the particles that are functionalized to the substrate surface may improve the cell failure rate, or finding a way to have functionalized particles be more uniform in surface roughness to avoid device shorts.

References

(1) Zhang, Q.; Li, N.; Goebl, J.; Lu, Z.; Yin, Y. Journal of the American Chemical Society 2011, 133, 18931.

(2) Aherne, D.; Ledwith, D. M.; Gara, M.; Kelly, J. M. Advanced Functional Materials 2008, 18, 2005.

(3) Kingsley, J. W.; Green, A.; Lidzey, D. G. In Organic Photovoltaics X; SPIE: 2009; Vol. 7416, p 74160T.

(4) Li, X.; Choy, W. C. H.; Huo, L.; Xie, F.; Sha, W. E. I.; Ding, B.; Guo, X.; Li, Y.; Hou, J.; You, J.; Yang, Y. Advanced Materials 2012, 24, 3046.

(5) Chen, H.-C.; Chou, S.-W.; Tseng, W.-H.; Chen, I. W. P.; Liu, C.-C.; Liu, C.; Liu, C.-L.; Chen, C.-h.; Wu, C.-I.; Chou, P.-T. Advanced Functional Materials 2012, 22, 3975.

(6) Wang, D. H.; Park, K. H.; Seo, J. H.; Seifter, J.; Jeon, J. H.; Kim, J. K.; Park, J. H.; Park, O. O.; Heeger, A. J. Advanced Energy Materials 2011, 1, 766.

(7) Wang, D. H.; Kim, D. Y.; Choi, K. W.; Seo, J. H.; Im, S. H.; Park, J. H.; Park, O. O.; Heeger, A. J. Angewandte Chemie International Edition 2011, 50, 5519.

(8) Wang, W.; Vaughn, M. W. Scanning 2008, 30, 65.

(9) Li, X.; Choy, W. C. H.; Lu, H.; Sha, W. E. I.; Ho, A. H. P. Advanced Functional Materials 2013, 23, 2728.

(10) Shrotriya, V.; Li, G.; Yao, Y.; Chu, C.-W.; Yang, Y. Applied Physics Letters 2006, 88, 073508.

(11) Wu, J.-L.; Chen, F.-C.; Hsiao, Y.-S.; Chien, F.-C.; Chen, P.; Kuo, C.-H.; Huang, M. H.; Hsu, C.-S. ACS Nano 2011, 5, 959.

(12) Salvador, M.; MacLeod, B. A.; Hess, A.; Kulkarni, A. P.; Munechika, K.; Chen, J. I. L.; Ginger, D. S. ACS Nano 2012, 6, 10024.

(13) Heo, M.; Cho, H.; Jung, J.-W.; Jeong, J.-R.; Park, S.; Kim, J. Y. Advanced Materials 2011, 23, 5689.

Chapter 4 - Conclusions

Discussion and Conclusions

This thesis describes how nanoparticles of different shapes and materials can be functionalized to increase their solubility in organic solvents, and their subsequent application in BHJ solar cells. Chapter 2 describes how nanoparticles can be functionalized to be phase transferred into different solvents, as well as the mechanism by which the nanoprisms are converted into nanoplates. BHJ solar cells require organic solvents for dissolution of the active layer. By functionalizing the nanoparticles so that they are soluble in organic solvents, the nanoparticles can then be introduced into the same solvent as the BHJ active layer. Chapter 3 contains currently unpublished data and is a discussion of how the functionalized nanoparticles were incorporated into the active layer of BHJ solar cell, and how this affected cell performance.

The development of methods to increase the stability of Ag nanoprisms and to preserve their sharp tips is essential to maximize near-field effects in various plasmonic applications including solar cells. The mechanism proposed in chapter 2 for the shape transformation of Ag nanoprisms, takes factors such as PEG-SH molecular weight and concentration, as well as the O_2 in the ambient environment into consideration. Excess PEG-SH in the reaction solution will react with silver ions at the high surface energy tips of the nanoprism, which will result in the formation of silver thiolate complexes and the rounding of the nanoprism tips. O_2 accelerates the tip-rounding process by continuously oxidizing the silver surface, and an important part of the tip rounding process. The Ag thiolate complex will then undergo a spontaneous redox reaction, resulting in the formation of small Ag clusters and PEG disulfide. These results demonstrate that low concentrations of high molecular weight PEG-SH are critical for the stability of the nanoprisms. The stability of these prisms is important if they are to be incorporated into BHJ

solar cells. If the shape degradation of the particles can be avoided as they are incorporated into the cell, the properties of the particles that may enhance the efficiency of the cell can be maintained.

In chapter 3, nanoparticles of different shapes, sizes, and materials were incorporated into the active layer, and beneath the hole transport layer of BHJ cells. The particles that were incorporated include, 10 nm and 60 nm Ag nanoparticles, 10 nm and 60 nm Au nanoparticles into the active layer, and 25 nm silver nanoprisms in the active layer and under the hole transport layer. These cells were tested and compared to a number of control cells. The study found that the incorporation of nanoparticles into the active layer of BHJ cells does not increase the efficiency of the cell. Statistical t-tests of the efficiency and J_{SC} values were done comparing each different cell to the control cells. This confirmed that the addition of metallic nanoparticles does not increase the efficiency of a BHJ cell, and in some cases may cause a decrease in efficiency.

Literature examples show that metal nanoparticles have already been incorporated into OPVs with some success. Li et al. were able to incorporate both Ag nanoprisms and Ag nanoprisms into a P3HT:PCBM BHJ cell, and saw an efficiency enhancement from 3.60% to 4.30% with both nanoparticles and nanoprisms in the cell.[1] Also, Wang et al. incorporated Au octahedral nanoparticles into a P3HT:PCBM cell, and reported an increase in efficiency from 3.49% to 4.36% was reported.[2] However, in both studies there is no discussion as to how well the nanoparticles are solubilized. Both studies describe that the nanoparticles were dispersed into organic solvent, not functionalized with any ligands that may improve their solubility. This brings about the question, how evenly distributed are the particles within the active layer? Are

the particles spread throughout the active layer, do they settle to the bottom of the active layer, or do the aggregate into much larger particles?

In our work, by functionalizing the nanoparticles, we ensure that they are soluble in the organic solvent used to deposit the active layer, allowing for an even distribution throughout the active layer. If particle aggregation is what is needed to enhance cell efficiency, perhaps this is why other work is seeing an increase in cell efficiency and our study is not.

Another cause of these observed decreases may be from the metallic nanoparticles acting like electron traps. It has been found that when in contact with photoexcited material, metallic nanoparticles can accumulate long-lived negative charges.[3] In order to avoid this phenomenon, as well as protect them from shape change, our particles were coated with PEG-SH, but perhaps this layer is not thick enough to protect them from the electron accumulation. Perhaps an even longer chain PEG-SH may be needed to prevent the particles from becoming electron traps, which complements the conclusions that a longer PEG-SH will protect the particles from shape change.

In the literature there are examples of BHJ cells that have metal nanoparticles under the hole transport layer, similar to what was done in this study. An efficiency increase from 2.90% to 3.35% was reported Heo et al. upon incorporation of Au-Cu nanoparticle alloys between the hole transport layer and the anode.[4] This study avoided having to functionalize the surface of the substrate, by using templates to deposit the nanoparticle directly onto the substrate, and consequently they were able to spin coat the PEDOT:PSS directly onto the nanoparticles. Unlike our study, this method may result in more uniform layers within the cell, leading to a lower device failure rate.

The BHJ cells in our study that have the nanoparticles incorporated beneath the hole transport layer did not exhibit a statistically significant increase in efficiency. This may be due to particle oxidation during deposition, or during the thermal evaporation of the hole transport layer. Also, by soaking the substrates in a solution of nanoparticles, there is no guarantee that there will be an even layer of metal nanoparticles on the substrate. This may lead to an uneven coating of the subsequent cell layers, which may be the reason why a large number of devices did not work or demonstrated an extremely low efficiency.

Overall the incorporation of metal nanoparticles was unsuccessful, but great strides in cell development have been made. Nanoparticle stability has been investigated and procedures to avoid shape degradation have been developed, procedures for making and testing control cells are consistent, and the incorporation of the nanoparticles into the active layer, and under the hole transport layer are successful.

Future Direction

Work still needs to be done on improving the efficiency of the cells containing metal nanoparticles. Changing the capping agent or chain length of the solubilising polymer may improve the cells with nanoparticles in the active layer by preventing the particles from becoming electron sinks, and protecting them from any morphology change. Avoiding oxidation of the particles that have been functionalized to the substrate surface may improve the cell failure rate in cells where nanoparticles are beneath the hole transport layer. Also, finding a way to have functionalized particles be more uniform in surface roughness may help to avoid device shorts.

References

(1) Li, X.; Choy, W. C. H.; Lu, H.; Sha, W. E. I.; Ho, A. H. P. Advanced Functional Materials 2013, 23, 2728.

(2) Wang, D. H.; Kim, D. Y.; Choi, K. W.; Seo, J. H.; Im, S. H.; Park, J. H.; Park, O. O.; Heeger, A. J. Angewandte Chemie International Edition 2011, 50, 5519.

(3) Salvador, M.; MacLeod, B. A.; Hess, A.; Kulkarni, A. P.; Munechika, K.; Chen, J. I. L.; Ginger, D. S. ACS Nano 2012, 6, 10024.

(4) Heo, M.; Cho, H.; Jung, J.-W.; Jeong, J.-R.; Park, S.; Kim, J. Y. Advanced Materials 2011, 23, 5689.